January 2011

Methyl Halide Cluster Anion Photoelectron Spectra and Angular Distributions as a Probe of Electron-Molecule Interactions

Matthew Van Duzor
Washington University in St. Louis

WASHINGTON UNIVERSITY IN ST. LOUIS

Department of Chemistry

Thesis Examination Committee:
Richard Mabbs, Chair
Dan Giammar
Sophia Hayes
Rich Loomis
Jay Ponder
Jacob Schaefer

METHYL HALIDE CLUSTER ANION PHOTOELECTRON SPECTRA AND ANGULAR DISTRIBUTIONS AS A PROBE OF ELECTRON-MOLECULE INTERACTIONS

by

Matthew William Van Duzor

A dissertation presented to the Department of Chemistry
of Washington University in partial fulfillment of the
requirements for the degree of

DOCTOR OF PHILOSOPHY

August 2011
Saint Louis, Missouri

ABSTRACT OF THE DISSERATATION

Methyl Halide Cluster Anion Photoelectron Spectra and Angular Distributions as a Probe of Electron-Molecule Interactions

by

Matthew William Van Duzor

Doctor of Philosophy in Chemistry

Washington University in St. Louis, 2011

Research Advisor: Professor Richard Mabbs

This dissertation describes the development of a method for studying electron-molecule interactions using cluster anion photodetachment. Photodetachment from an atomic centered cluster anion produces a free electron and a residual neutral species at a geometry near that of the unperturbed neutral ground state. Evidence of the free electron-molecule interactions, manifested in the photoelectron spectra and angular distributions, are elucidated through comparison to photodetachment data from the unsolvated atomic anion in question. Results are presented from number of monosolvated anion studies, including $I^-\cdot CH_3I$, $I^-\cdot CH_3Br$, $I^-\cdot CH_3Cl$ and $Cl^-\cdot CH_3I$, as well as a study of the disolvated anion $I^-\cdot(CH_3I)_2$. The findings demonstrate the usefulness of this method as a probe of anion-molecule solvation structure, long range electron-molecule interactions, solvent electronic structure, and the influence of the cluster environment upon photodetachment dynamics. A detailed description of the experimental methods, including the construction and operation of the instrumentation,

is presented. Applications of the method towards further study of electron-neutral resonances and electron initiated chemical reactions are discussed.

Acknowledgments

This thesis could not have been completed without the support, expertise and guidance of many individuals. I wish to sincerely thank all who have assisted me, professionally and personally, in this effort.

My gracious thanks to my advisor, Professor Richard Mabbs, for his commitment to teaching in both the laboratory and the classroom, and his patient mentoring. The opportunity to join his laboratory in its earliest days and aid in its construction and operation provided invaluable experience in my development as an experimentalist.

My thanks to Professor Rich Loomis for his encouragement, advice and assistance throughout my time in St. Louis.

I am also grateful for the opportunity to perform calculations using the USC Center for Computational Studies of Electronic Structure and Spectroscopy of Open-Shell and Electronically Excited Species iopenshell environment. This work could not have taken place without the financial support of the NSF and the ACS PRF; my thanks to both. Additionally, I thank the Graduate School of Arts and Sciences for awarding me the Dean's Dissertation Fellowship.

I would also like to acknowledge my dissertation committee, Professors Richard Mabbs, Jacob Schaefer, Rich Loomis, Sophia Hayes, Jay Ponder and Dan Giammar. My thanks for your time, insight and input.

I thank my present and former group members, Diep Dao, Nick Holtgrewe, Josh Lasisnski, Foster Mbaiwa and Dr. Jie Wei. I have appreciated your opinions and camaraderie over the years.

Finally, I offer my heartfelt gratitude to my friends and family, in particular my parents, William and Dolores and my wife, Andrea, for their constant encouragement and support.

Matthew William Van Duzor

Washington University in Saint Louis
August 2011

Contents

List of Tables

List of Figures

Chapter 1

Introduction

The focus of this dissertation is the development of a novel approach to elucidate details of electron-molecule interactions using cluster anion photodetachment. Cluster anions are a very interesting class of chemical species, displaying complex intermolecular interactions and solvation structure associated with condensed phases, while affording the considerable improvement in spectral resolution available in the gas phase.[1, 2] Laser excitation of cluster anions may delocalize the extra electron within the cluster framework, or remove it entirely. The work presented here seeks to explore, through use of cluster anion photoelectron spectra and angular distributions, details of free electron-molecule interactions.

At the most fundamental level, chemistry is dictated by electronic structure. Alteration of molecular orbital occupancies by addition or removal of electrons can produce marked changes in molecular geometry and reactivity. A simple, yet dramatic example is that of dissociative electron attachment (DEA), wherein an extra electron is captured into an antibonding molecular orbital of a neutral molecule, bringing about bond cleavage and production of an anionic fragment. Such processes have historically been studied through electron scattering experiments, providing insight

into the electronic structure and long range interactions of electrons with molecules at their equilibrium geometry.

The reverse process, the removal of an excess electron from an anion, is the basis of negative ion photoelectron spectroscopy. Beginning with a stable anionic species, interaction with a sufficiently energetic photon may detach the extra electron, producing a free electron and a neutral molecule. In the limit of the Born-Oppenheimer approximation (the assumption that the molecular geometry is essentially "fixed" on the very brief timescale of the photodetachment event), the residual neutral species is produced at the equilibrium geometry of the anion. The resulting spectral features contain information about non-equilibrium regions of the neutral potential energy surface, as well as the relative energy of the anion parent orbital. Further information is encoded within the angular distribution of the photoelectrons, which is highly dependent upon the parent orbital angular momentum and the kinetic energy of the free electron. Additionally, interactions between the departing electron and the neutral residue may bring about changes in the angular distribution akin to those observed in electron-molecule scattering. Unlike a scattering experiment, however, the free electron is not interacting with the equilibrium geometry of the neutral, but rather with an excited, distorted geometry of the neutral. The long range electron-neutral interactions can be expected to be quite different.

Photodetachment from cluster anions presents an integrated approach to the study of the electron-molecule interactions described above. Information of fundamental chemical importance, including electron binding energies and motifs, "solute-solvent" interactions and cluster geometries can be obtained from photodetachment studies. Additionally, electron-solvent molecule interactions subsequent to detachment of the excess electron can provide insight to long range interactions that govern

cluster chemistry. In this sense, cluster anion photodetachment may be considered both a probe of anion-neutral solvation interactions, as well as a molecular-scale electron scattering experiment.

Cluster anions studied in this work contain one or more methyl halide molecules centered around an atomic halide anion. These species are ideal candidates to demonstrate the potential of the cluster anion approach. The clusters themselves occupy local minima along the ion S_N2 reaction coordianate[3–5], and the solvating methyl halide species are known to be quite sensitive to low energy electron scattering and attachment.[6–10] The extra electron in such halide centered cluster anions is likely to be highly localized within an atomic p-orbital of the halide moiety. Additionally, the nearby methyl halide molecules are likely to experience only a minimal geometric distortion. Upon photodetachment, the nascent electron samples the potential of the neutral cluster, which is predominantly that of the methyl halide molecule near its equilibrium geometry.

The velocity-map imaging technique,[11, 12] coupled with a tunable laser source, allows for the simultaneous collection of photoelectron spectra and angular distributions over a range of energies. The experimental strategy applied allows comparison of the spectra and angular distributions arising from free halide anion photodetachment to those produced by halide anions bound in clusters. This dissertation will show that striking differences are observed, as a result of intracluster and electron-molecule interactions. Cluster anions of specific composition may be produced and mass selected using ion generation and time-of-flight methods, allowing the experimenter to "tailor" the cluster environment. This is particularly useful for purposes of comparison. As will be seen throughout the work presented here, variation of the

cluster constituents and size of the clusters will have a pronounced effect upon the observed spectra and angular distributions.

The following chapter presents general background information on photoelectron spectroscopic techniques and theory essential to understanding of the remainder of the dissertation. This includes an overview of the photodetachment process and a discussion of the total and differential photoelectron cross sections. Special consideration is given to discussion of photoelectron angular distributions. Results presented in later chapters will show how sensitive the angular distribution is as a probe of electron-molecule interactions.

Chapter 3 outlines the design of the photoelectron imaging spectrometer constructed to perform this work. This includes discussion of ion production and selection techniques and apparatus, discussion of salient aspects of the laser system and detailed description of the velocity-map imaging spectrometer.

Chapter 4 demonstrates how electron-molecule interactions manifest in the photoelectron spectra and angular distributions using experimental results from photodetachment of the $I^-\cdot CH_3I$ cluster anion. The resulting spectra and angular distributions are compared with I^- photodetachment data over a similar energy range. Pronounced evidence of electron-molecule scattering is found in the $I^-\cdot CH_3I$ data, particularly the angular distributions.

Chapter 5 presents the results of a comparative study of cluster anion photodetachment from $I^-\cdot CH_3I$, $I^-\cdot CH_3Br$ and $I^-\cdot CH_3Cl$. Examination of the evolution of both the spectral features and angular distributions with photodetachment energy elucidates the influence of the long range potentials and electronic structure of the solvent molecule in photodetacment. While in many ways physically similar, these

clusters display markedly different photodetachment behavior at low energy, illustrating the sensitivity of cluster anion photodetachment to change in the nature of the solvent. Despite these differences at lower energies, each of these clusters displays evidence of a narrow autodetachment resonance near the excited state threshold of the halogen atom core. The implications of this behavior are explored here and in subsequent chapters.

Chapter 6 discusses the possibility of using cluster anions to probe different coupling mechanisms encountered in photodetachment by modifying the cluster anion core. Photodetachment from $Cl^-\cdot CH_3I$ is studied in the context of data previously presented on the $I^-\cdot CH_3I$ cluster anion. The spectra display interesting structure unique to the $Cl^-\cdot CH_3I$ cluster anion.

Chapter 7 demonstrates extension of this approach to multiply-solvated anions. The results of photodetachment from the $I^-\cdot(CH_3I)_2$ cluster anion illustrate the concerted influence of multiple solvent molecules upon the long range electron solvent interaction. The data presented offer information regarding the cluster geometry and solvent electronic structure, as well as the dissociative electron attachment dynamics.

The key findings of this work, as well new directions for experimental inquiry of cluster anion systems, are discussed in chapter 8.

Chapter 2

Photoelectron Spectroscopy

The interaction of a photon with a neutral atom may drive oscillations of the electrons within the atom. If the energy of the photon, $h\nu$, is such that $h\nu = E_f - E_i$, where E_f is an excited atomic state of allowed symmetry and E_i is the ground state of the atom, absorption may occur producing an excited atomic state. For photon energies greater than the atomic ionization potential (IP, typically 10 or more eV), ejection of the electron may follow photoexcitation according to the equation $h\nu$ - IP = eKE, where eKE is the resulting kinetic energy of the free electron. This statement of conservation of energy is familiar from the photoelectric effect, with the metal work function (Φ) replaced by the atomic ionization potential.

Negative ions, by contrast, very rarely possess stable excited states.[13]Considering negative ion structure from the perspective of an excess electron bound to a screened atomic core, the dominant binding potential is the polarization interaction, $\propto \alpha/r^4$, where α is here the atomic polarizability.[14] Upon absorption of a photon, the interaction of the neutral atom and the free electron is mediated by the centrifugal potential, $\propto \ell(\ell+1)/r^2$, where ℓ is the angular momentum of the free electron. Unlike the coulomb potential, which is $\propto$ 1/r and represents the dominant interaction

upon photoionization of neutrals, the polarization and centrifugal potentials are usually insufficient to support excited states. As a result, negative ion binding energies (electron binding energies, eBE) typically lie between 1-4 eV, far less than neutral IPs and readily accessible to commercially available tunable radiation sources.

Although the above-mentioned $1/r^n$ ($n \geq 2$) rarely support stable excited states in negative ions, the effect of these potentials upon the departing photoelectron can be dramatic. It is this class of potentials that governs electron-atom and electron-molecule scattering interactions, including negative ion resonances and electron attachment. The investigation of such scattering interactions through photodetachment spectroscopy is a focal point of this work, utilizing atomic halide moieties within clusters of dipolar molecules as electron sources.

The iodide anion plays a central role in the work presented throughout this dissertation. With the single exception of the $Cl^-{\cdot}CH_3I$ cluster anion discussed in chapter 6, the cluster anions studied herein consist of a molecule or molecules physically bound to an iodide anion. Figure 2.1 displays an example of photodetachment from I^- at 300 nm (4.13 eV) photodetachment wavelength. Absorption of a 4.13 eV photon by I^- produces a free electron as well as a residual neutral iodine atom in either the $^2P_{3/2}$ or $^2P_{1/2}$ neutral state. At the simplest level of approximation the electron binding energy (eBE $= h\nu -$ eKE) is assumed to be equivalent to the electron affinity. This can be seen in Figure 2.1, where the lowest neutral detachment channel, $^2P_{3/2}$ state of I, displays an eBE of 3.06 eV, equivalent to the electron affinity.

In the case, however, of photodetachment from molecular anions or cluster anions, differences in the geometry of the anion with respect to the neutral are likely. This is due to either orbital occupation in molecular anions or distortion of bonds

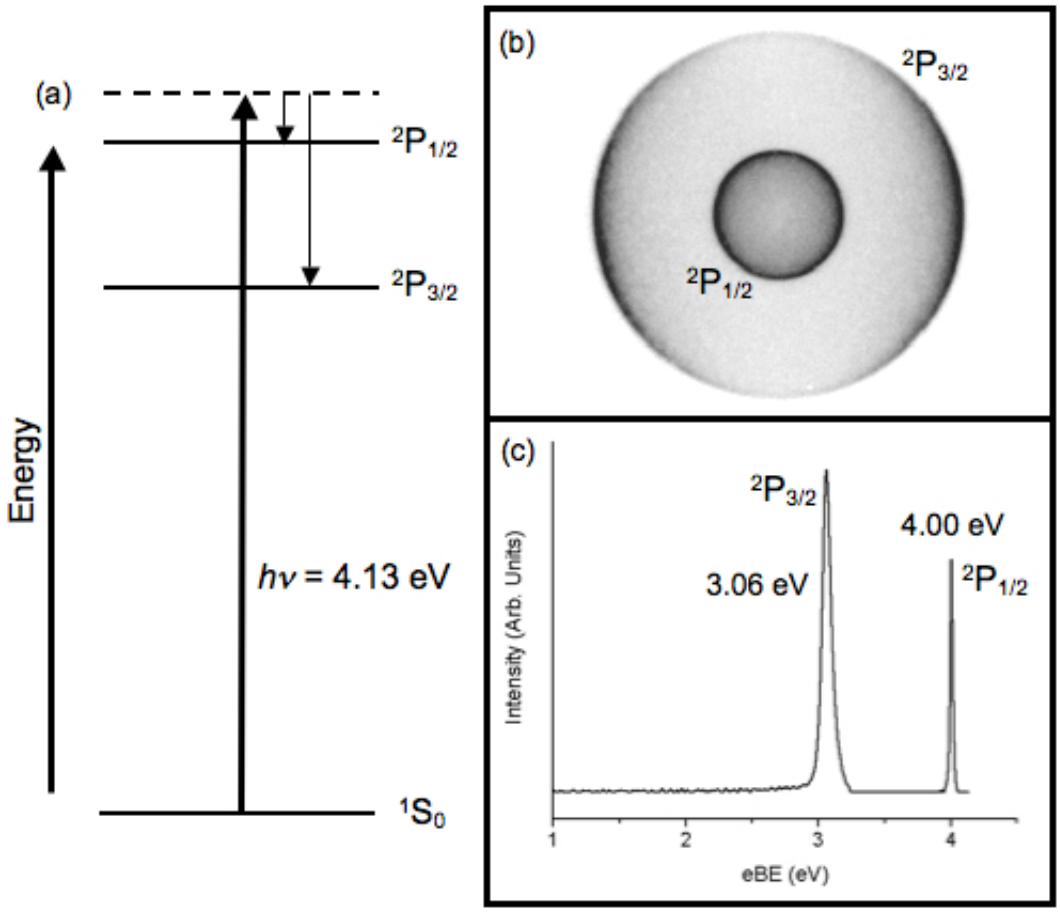

Figure 2.1: Sample photodetachment from I^- at 300 nm. (a) Schematic description of photodetachment from I^- displaying the $^1S_0$ anion and $^2P_{3/2}$ and $^2P_{1/2}$ neutral states. (b) The resulting photoelectron image with transitions to the $^2P_{3/2}$ and $^2P_{1/2}$ states labeled. (c) The photoelectron spectrum in electron binding energy (eBE) domain.

within cluster constituents due to ion-molecule interactions. As a result the vertical detachment energy (VDE), in the Born-Oppenheimer limit, will be greater than the adiabatic electron affinity (AEA). This is illustrated in Figure 2.2 (VDE $\geq$ AEA).

Photoelectron spectroscopies also benefit from diminished restriction of allowed atomic and molecular final states. In the electric dipole limit, the selection rules $\Delta\ell = \pm 1$, $\Delta m = 0$ still hold for the case of linearly polarized radiation. However, final states accessed upon photodetachment comprise a neutral species plus a free electron.

To a very good first approximation, the photon angular momentum is coupled entirely to the continuum electron state. At energies away from threshold, all allowed values of ℓ are accessible. Optically "dark" states of the neutral residue, those that would not be allowed *via* photon absorption from the neutral ground state, are thus observable. This is particularly useful to the study of neutral halides and halide-centered clusters, where the energetic splitting in the $^2P_{3/2}$ and $^2P_{1/2}$ states of the halogen core, a spin-forbidden transition, is readily observable in a single measurement (see Figure 2.1 for example).

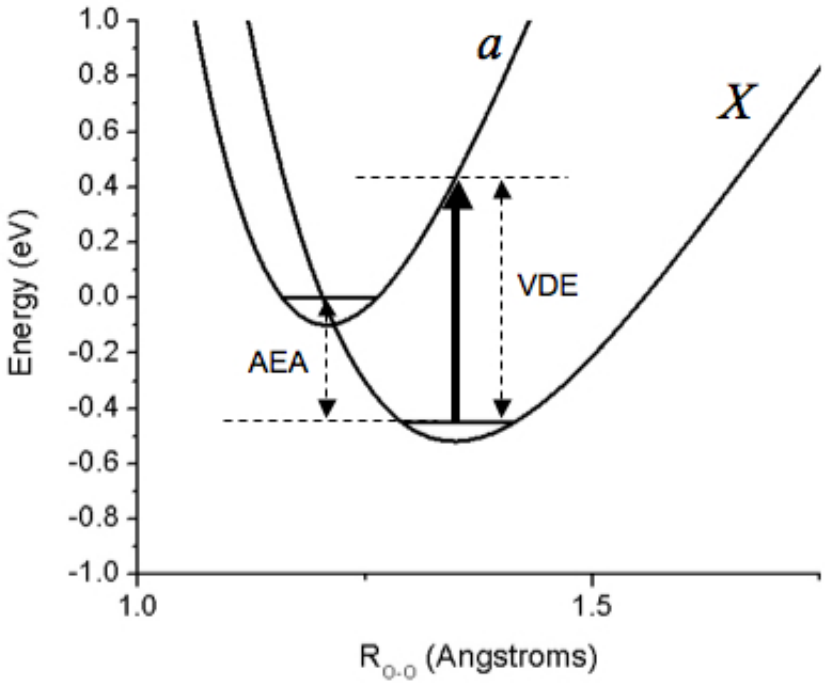

Figure 2.2: Illustration of the transition $O_2\, X^3\Sigma_g^- + e^- \leftarrow O_2^-\, {}^2\Pi_g + h\nu$. The difference between the adiabatic electron affinity (AEA) and the vertical detachment energy (VDE) is shown.

2.1 The Photodetachment Cross Section

What follows is a semi-classical development of the photodetachment cross section. The species presented in this work are all either free atomic anions or atomic centered cluster anions; this being the case the discussion will be restricted to the case of atomic anion photodetachment in which the angular momentum quantum number ℓ is a "good" number. The subject of single-photon absorption in atoms has been treated at length by a number of authors.[15, 16] Only those aspects of the development that are most relevant to understanding the work presented here will be described in detail.

The classical description of the oscillating electric field of a beam of light is a plane wave

$$\mathbf{E} = \mathbf{E}_0 e^{i(\mathbf{k}\cdot\mathbf{r}-\omega t)} \tag{2.1}$$

Here $\mathbf{E}_0$ is the electric field vector of the laser, $\mathbf{k}$ is the wave vector $(2\pi/\lambda)$ and ω is the frequency of the oscillating field. Assuming $\lambda \approx 2 - 8 \times 10^{-7}$ m and the atomic anion diameter D$\approx 1 \times 10^{-10}$ m, $\mathbf{k}\cdot\mathbf{r}/D \gg 1$. Therefore, if it is assumed that the electric field gradient is constant in the vicinity of the target atom (situated at $\mathbf{r} = 0$), and Equation 2.1 can be rewritten as

$$\mathbf{E} = \mathbf{E}_0 \cos(\omega t) \tag{2.2}$$

In the dipole approximation, the interaction of the electric field of the light with the electrons in the atom then is described as

$$H'(t) = \mu \cdot \mathbf{E} = \mu \cos(\omega t) \tag{2.3}$$

where μ is the dipole operator $\mu = -e\sum_i \mathrm{r}_i$. Equation 2.3 is reduced, in the case of polarization in the z direction, to

$$H'(t) = \mu_z E_{0z}\cos(\omega t) \tag{2.4}$$

This term is then inserted into the time dependent Schrödinger equation:

$$ih\frac{\partial \Psi}{\partial t} = [H_0 + H'(t)]\,\Psi \tag{2.5}$$

In the presence of the perturbing electric field (which is "turned on" for times $t > 0$), the wave function Ψ is written as a linear combination of the initial and final states

$$\Psi = C_0 \mid \psi_0\rangle e^{-i\omega_0 t} + C_k \mid \psi_f\rangle e^{-i\omega_f t} \tag{2.6}$$

where the definition of the wave functions $\mid \psi_0\rangle$ and $\mid \psi_f\rangle$ is as follows:

$$\mid \psi_0\rangle = \mid \psi_{n\ell' m'}(\mathbf{r})\rangle = R_{n\ell'}(\mathbf{r})Y_{\ell',m'}(\theta',\phi') \tag{2.7a}$$

$$\mid \psi_f\rangle = \mid \psi_f(\mathbf{r})\rangle = 4\pi\sum_{\ell=1}^{\infty}\left[i^{\ell}e^{-i\delta_\ell}R_{k,\ell}(\mathbf{r})\sum_{m=-\ell}^{\ell}Y^*_{\ell,m}(\theta,\phi)Y_{\ell,m}(\theta',\phi')\right] \tag{2.7b}$$

The initial state is a well defined angular momentum state described by hydrogenic wave functions. The final state, by contrast, describes a free electron with a wave vector of magnitude k and lacks a well defined angular momentum; rather, it is a sum of all available angular momentum states defined by the quantum numbers ℓ and m. The δ_ℓ term describes the behavior of the phase shift of the outgoing electron.

Using the above defined terms, it is straightforward to demonstrate [15] that the probability of finding the system at a time t in a particular final state $\psi_k = \psi_f$ is

given by the equation

$$\begin{aligned} \mid C_f \mid^2 &= \frac{e^2 \mid M_{fi} \mid^2 E_{0z}^2}{\hbar^2} \frac{\sin^2((\omega - \omega_{f0})t/2)}{(\omega - \omega_{f0})^2} \\ &= \frac{e^2 \mid M_{fi} \mid^2 E_{0z}^2}{\hbar^2} \pi t \delta(\omega_{f0} - \omega) \end{aligned} \tag{2.8}$$

Here, M_{fi} is the dipole matrix element for the transition $\psi_f \leftarrow \psi_0$, defined here as

$$M_{fi} = \langle \psi_f \mid z_i \mid \psi_0 \rangle \tag{2.9}$$

Differentiating Equation 2.8 with respect to time produces the absorption rate for the transition $\psi_f \leftarrow \psi_0$, denoted here as

$$P_{f \leftarrow 0} = \frac{\pi \mid M_{fi} \mid^2 E_{0z}^2}{\hbar^2} \delta(\omega_{f0} - \omega) \tag{2.10}$$

The cross section is defined as the absorption rate to the continuum divided by the intensity of the incident radiation at the resonance energy $\hbar\omega_{f0}$. Dividing the quantity $\hbar\omega_{f0} \times P_{f \leftarrow 0}$ by $I(\omega)\bar{2}\epsilon_0 c\omega_{f0}^2 E_{0z}^2$ produces

$$\sigma(\omega_{f0}) = \frac{P_{f \leftarrow 0}\hbar\omega_{f0}}{I(\omega_{f0})} = \frac{2\pi^2\alpha}{\omega_{fo}} \mid M_{fi} \mid^2 \delta(\omega_{f0} - \omega) \tag{2.11}$$

where the fine structure constant $\alpha = [e^2/(4\pi\epsilon_0 c\hbar)]$ has been inserted.

Equation 2.11 must now be integrated over all possible directions and energies k. Using the integration element $d\mathbf{k} = k^2 dk d\Omega$, the relation eKE $= \hbar^2 k^2/2m_e = \hbar\omega -$ eBE and averaging over all orientations and polarization axes produces the result[17]

$$\sigma_{tot} = \frac{8\pi^2 m_e \alpha \omega k}{3\hbar} \int \mid M_{fi} \mid^2 d\Omega \tag{2.12}$$

Which is the expression for the total cross section for photodetachment. Given an initial state $(\ell' m')$, for transitions other than $\ell = \ell' \pm 1$ and $m = m'$, the dipole matrix element $M_{fi} = 0$. Therefore, the square modulus of the dipole matrix element can be written in the simplified form

$$\mid M_{fi} \mid^2 = \sum_m \mid M_{\ell'+1} \mid^2 + \mid M_{\ell'-1} \mid^2 + 2\left(M_{\ell'+1} M_{\ell'-1}\right) \tag{2.13}$$

Recalling Equation 2.7b, the third term on the right of Equation 2.13 will contain a factor $Y_{\ell'+1,m}(\theta,\phi) Y_{\ell'-1,m}(\theta,\phi)$, which vanishes upon integration over all angles. Inserting the first two terms on the right-hand side of 2.13 into 2.12, it is evident that the total cross section σ_{tot} is in fact a sum of the cross sections σ_ℓ for each partial wave.

$$\sigma_{tot} = \frac{8\pi^2 m_e \alpha \omega k}{3\hbar^2} \int \left(\mid M_{\ell'+1} \mid^2 + \mid M_{\ell'-1} \mid^2 \right) d\Omega = \sum_\ell \sigma_\ell \tag{2.14}$$

Differentiation of Equation 2.12 with respect to Ω (which, given that the photoelectron distribution is cylindrically symmetric with respect to the polarization axis, reduces to differentiation over θ) produces the differential cross section[17]

$$\frac{d\sigma}{d\Omega} = \frac{4\pi^2 m_e \alpha \omega k}{\hbar} \mid M_{fi} \mid^2 \tag{2.15}$$

Referring to Equation 2.15, it should be noted that in addition to the square moduli of the partial wave dipole matrix elements, this form of the cross section retains the amplitudes and phase shifts of the cross term on the far-right of Equation 2.13. This important detail will be discussed further in section 2.2.

2.1.1 The Wigner Threshold Law

Within Equation 2.12 the σ_ℓ have been shown to vary as a function of ω, k and the square moduli of the dipole matrix elements. This is generally true in the absence of resonances and at energies away from a threshold. Near the photodetachment threshold, the centrifugal interaction, Equation 2.16, between the nascent photoelectron and the neutral residue presents a barrier to electron escape.

$$V_c = \frac{\hbar\ell(\ell+1)}{2\mu r^2} \tag{2.16}$$

Here r is the radial distance at which the electron can be found with respect to the center of mass and μ is the reduced mass, which is $\sim m_e$. The effect of this interaction upon the cross section is stated in the Wigner threshold law.

Assuming an electron moving in a central potential, the dominant term of which is the centrifugal interaction, the cross section near threshold takes the form, to first approximation:

$$\sigma_\ell \approx k^{2\ell+1} \tag{2.17}$$

Here, k is the magnitude of the photoelectron wave vector. For very low eKE, higher angular momentum partial waves are suppressed relative to those of lower angular momentum. For example, in the case of p-orbital detachent, only the s-wave channel is open at threshold. This effect is apparent in Figure 2.1b, displaying a photoelectron image resulting from detachment from I^- at 300 nm. Note that the innermost ring, produced through photodetachment *via* the $^2P_{1/2}$ channel of neutral iodine, is far more isotropic when compared to the outer ring, the $^2P_{3/2}$ phtotodetachment channel. This is a consequence of the large s-wave component σ_s relative to σ_d at low eKE.

In general, this law has important implications for interpretation of differential cross section (photoelectron angular distribution) data.

2.2 Angular Distributions of Photoelectrons

A wealth of information complimentary to the photoelectron spectrum can be extracted from the photoelectron angular distributions, or PADs. In general, PADs are strongly dependent upon the anion parent orbital and the eKE. In fact, the PAD is often referred to as a "signature" of the parent orbital. It is reasonable to suspect, however, that any anisotropic photoelectron-neutral residue interactions following photodetachment should also affect the final PAD.

This discussion will be limited to PADs produced in atomic photodetachment. It should be noted, however, that in several simple cases where the LUMO is very atomic-like in symmetry, the atomic model can be an adequate descriptor of the molecular PAD.[18–21]

When an unpolarized laser beam of wavelength sufficient to detach an excess electron ($h\nu \geq$ VDE) interacts with an anion, an electron is ejected at an angle γ from the propagation axis of the photons as in Figure 2.3. The cross section for photodetachment, σ_{tot} (equation 2.13), into the solid angle Ω subtending the interaction volume (the overlapping region of the laser beam and anion packet) is defined as the differential cross section, and is described in terms of γ as

$$\frac{d\sigma}{d\Omega} = I(\gamma) = \frac{\sigma}{4\pi}\left[1 - \frac{\beta}{4}(3\cos^2\gamma - 1)\right] \tag{2.18}$$

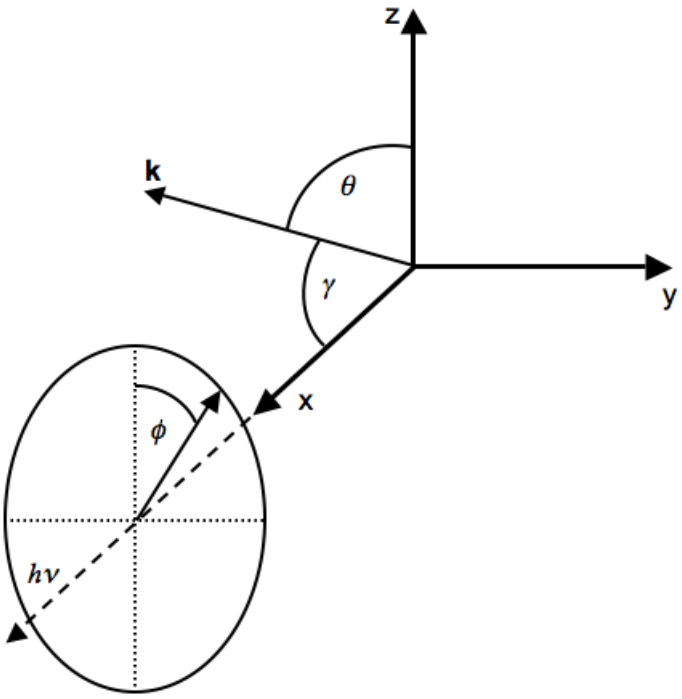

Figure 2.3: Coordinate space describing the angular dependence of photodetachment with unpolarized light. The target atom is placed at the origin, the x axis represents the direction of laser propagation and **k** is a vector describing the trajectory of the ejected electron (see text for further details).

Equation 2.18 is the result of integration over all polarization axes, denoted as the angle ϕ in Figure 2.3. Using a laser beam that is plane polarized parallel to the detector surface (in this case, parallel to the plane shared by the ion and laser beams. This experimental geometry is discussed in further detail in Chapter 3.), one may employ the relation

$$\cos\theta = \sin\gamma\cos\phi \tag{2.19}$$

where θ is the photoelectron ejection angle with respect to the z axis in the plane of the detector. If the polarization angle ϕ is fixed to coincide with z, the $\cos\phi$ term falls out of Equation 2.19. Substituting this result into Equation 2.18 produces the

well known equation

$$\frac{d\sigma}{d\Omega} = I(\theta) = \frac{\sigma}{4\pi}\left[1 + \frac{\beta}{2}(3\cos^2\theta - 1)\right] \tag{2.20}$$

or more concisely

$$\frac{d\sigma}{d\Omega} = I(\theta) = \frac{\sigma}{4\pi}\left[1 + \beta P_2(\cos\theta)\right] \tag{2.21}$$

where the quantity $1/2(3\cos^2\theta - 1)$ is recognized as the second Legendre polynomial $P_2(\cos\theta)$. The β term in Equation 2.21 is the anisotropy parameter, a coefficient which characterizes the overall distribution of the PAD. Allowed values of β vary from $+2$ (a $\cos^2\theta$ PAD or ejection parallel to the polarization axis) to -1 (a $\sin^2\theta$ PAD, ejection perpendicular to the polarization axis). It is clear upon inspection of Equation 2.21 that $\beta = 0$ removes all angular dependence, describing a purely isotropic photodetachment event. Section 2.2.1 below is devoted to a simplified derivation of the anisotropy parameter β and its physical significance, with special focus given to photodetachment from atomic anions.

2.2.1 The Anisotropy Parameter β

The $\cos^2\theta$ dependence of the PAD described by Equation 2.21 can be recognized through analysis of the electric dipole transition matrix element M_{fi}. Referring to Figure 2.4, **E** describes the orientation of the photon electric field vector in the lab frame and **k** refers to the direction of photoelectron ejection, defined relative to **E** by the angle θ. This notation is consistent with section 2.1. The expression for M_{fi}, Equation 2.9, can thus be written

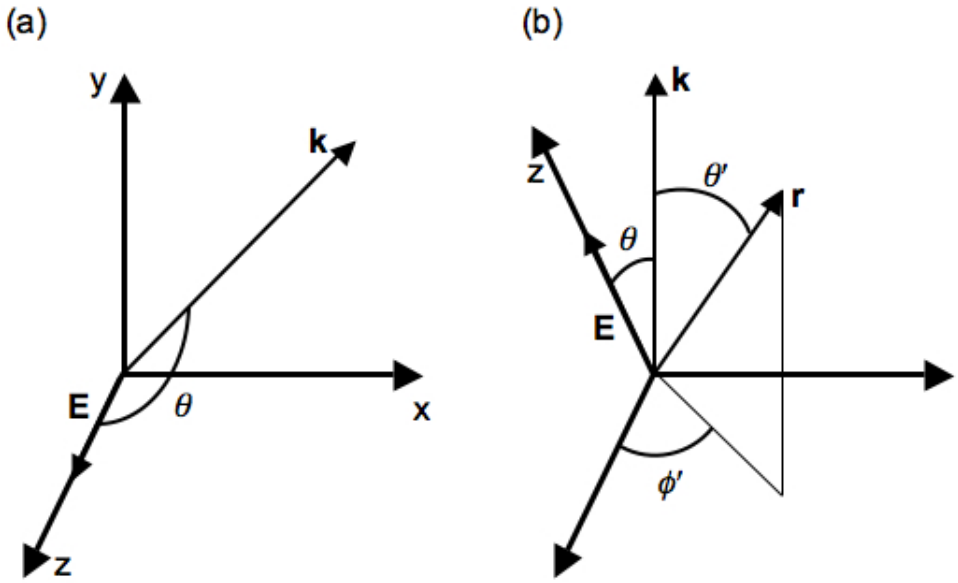

Figure 2.4: The coordinate space in which the photodetachment event is described. (a)**k** describes the trajectory of the free electron, **E** is the photon electric field vector and θ is the angle between **k** and **E**. (b) The coordinate space recast in spherical coordinates (**r**,θ',ϕ').

$$\mathrm{M}_{fi} \propto \int \psi_f^*(\mathbf{r}) z \psi_{n\ell m}(\mathbf{r}) d\tau \tag{2.22}$$

According to the coordinate space defined in Figure 2.4b, the projection $z = \mathbf{E}\cdot\mathbf{r}$ can be expressed as

$$z = \mathbf{E}\cdot\mathbf{r} = r(\cos\theta\cos\theta' + \sin\theta\sin\theta'\cos\phi) \tag{2.23}$$

Inserting 2.23 into 2.22, squaring and summing over all values of m, the resulting expression for M_{fi}, and thus the differential cross section, assumes the familiar form[22]

$$\frac{d\sigma}{d\Omega} \propto \text{A } \sin^2\theta + \text{B}'\cos^2\theta = \text{A+B } \cos^2\theta \tag{2.24}$$

where B′= A + B.

Comparing Equation 2.24 with Equation 2.21 and solving for β in terms of A and B, one arrives at the expression

$$\beta = \frac{2\text{B}}{3\text{A+B}} \tag{2.25}$$

Using a similar approach[23], Bethe derived an explicit definition for β for the case of photoionization of a hydrogen-like atom in terms of Equation 2.25.[24] J. Cooper and R.N. Zare later demonstrated a similar derivation for the case of LS coupling in multi-electron atomic anion photodetachment.[25] It is worthy of note that although the relatively simple model of the angular anisotropy parameter presented here assumes a one-electron (hydrogenic) atomic case, the multi-electron model produces an identical result.[25]

As shown in Equation 2.15, the differential cross section is expressed in terms of the transition matrix element averaged over all orientations. The wave functions $\psi_f(\mathbf{r})$ and $\psi_{nlm}(\mathbf{r})$ are defined in section 2.1, Equation 2.7a and 2.7b. The initial state wave function is describes a well-defined angular momentum state, while the final state wavefunction is a sum over a series of angular momenta.

Use of the correct expression for the outgoing wave function is particularly critical to producing the desired outcome. The form employed here is a combination of an outgoing plane wave and an incoming spherical wave.[26] The important outcome

of this approach is that the interference between these terms produces an overall outgoing radial flux. It should further be noted that the functional form of 2.7b is typical of an outgoing scattered wave, and by analogy anion photodetachment may be referred to as a scattering "half-reaction", in that photoexcitation of the anion optically populates the "closest approach" state of the electron-atom scattering problem for an allowed final angular momentum state. The PAD, in this sense, reflects the influence of the long-range interactions upon the partial wave cross sections and phase shifts as the electron retreats from the neutral.

Returning to Equation (2.7b), it is rewritten for convenience as

$$\mid \psi_f(\mathbf{r})\rangle = \sum_{\ell,m} a_{\ell,m} R_{k,\ell}(\mathrm{r}) Y_{\ell,m}(\theta,\phi) \tag{2.26}$$

where

$$a_{\ell,m} = 4\pi i^{\ell} e^{-i\delta_\ell} Y^*_{\ell,m}(\theta,\phi) \tag{2.27}$$

Using the relation

$$z_i = r_i \cos\theta = r_i \sqrt{\frac{4\pi}{3}} Y_{10}(\theta,\phi) \tag{2.28}$$

where $r_i\cos\theta$ represents the position vector in the z direction of the ith electron in the dipole operator. Defining the radial integral as

$$\Re_\ell = \int r R^*_{n,\ell'}(\mathrm{r}) R_{k,\ell}(\mathrm{r}) dr \tag{2.29}$$

the transition matrix element $|\mathrm{M}_{fi}\,|^2$ can thus be evaluated as

$$\langle \psi_f(\mathbf{r}) \mid Y_{10} \mid \psi_i(\mathbf{r})\rangle = \sum_{\ell',m'} a_{\ell',m'} \Re_{\ell'} \sqrt{\frac{4\pi}{3}} \int Y^*_{\ell',m'}(\theta,\phi) Y_{10}(\theta,\phi) Y_{\ell,m}(\theta,\phi) d\Omega \tag{2.30a}$$

$$= \sum_{\ell',m'} a_{\ell',m'} \Re_{\ell'} (-1)^{m'} \left[\frac{2\ell+1}{2\ell'+1} \right]^{1/2} \langle \ell 100 \mid \ell' 0 \rangle \langle \ell 1 m 0 \mid \ell' m' \rangle \tag{2.30b}$$

The expression on the right side of Equation 2.30a is further simplified by use of the the Clebsch-Gordan coefficients, $\langle \ell 100 \mid \ell' 0 \rangle \langle \ell 1 m 0 \mid \ell' m' \rangle$ in 2.30b. These coefficients are non-zero only for the allowed $\Delta\ell = \ell \pm 1$ and $\Delta m = 0$ transitions. Limiting the sum over final angular momentum states ℓ to $\ell' \pm 1$ and setting $m' = m$, the following identities arise[27]:

$$\langle \ell 100 \mid (\ell+1) 0 \rangle \langle \ell 1 m 0 \mid (\ell+1) m \rangle = \frac{\sqrt{(\ell - m + 1)(\ell + m + 1)}}{(2\ell + 1)} \tag{2.31a}$$

$$\langle \ell 100 \mid (\ell+1) 0 \rangle \langle \ell 1 m 0 \mid (\ell-1) m \rangle = \frac{\sqrt{(\ell - m)(\ell + m)}}{(2\ell + 1)} \tag{2.31b}$$

These identities may be inserted into 2.30b. In order to arrive at an expression for the differential cross section, the integral Equation 2.30b must be squared and summed over all possible final states m. The result is averaged over $2\ell + 1$ initial states m, under the assumption that the states are equally populated. This yields

$$\begin{aligned} \frac{d\sigma}{d\Omega} =& \frac{16\pi^2}{2\ell+1} \sum_m \Bigg\{ \mid \Re_{\ell+1} \mid^2 \left[\frac{(\ell+1)^2 - m}{(2\ell+1)(2\ell+3)} \right] \mid Y_{\ell+1,m}(\theta,\phi) \mid^2 \\ &+ \mid \Re_{\ell-1} \mid^2 \left[\frac{\ell^2 - m}{(2\ell+1)(2\ell-1)} \right] \mid Y_{\ell-1,m}(\theta,\phi) \mid^2 \\ &+ \left[Y^*_{\ell+1,m}(\theta,\phi) Y_{\ell-1,m}(\theta,\phi) e^{-i(\delta_{\ell+1} - \delta_{\ell-1})} \right. \\ &\left. + Y^*_{\ell-1,m}(\theta,\phi) Y_{\ell+1,m}(\theta,\phi) e^{i(\delta_{\ell+1} - \delta_{\ell-1})} \right] \\ &\times \Re_{\ell+1} \Re_{\ell-1} \left[\frac{(\ell+1)^2 - m}{(2\ell+1)(2\ell+3)} \right]^{1/2} \left[\frac{\ell^2 - m}{(2\ell+1)(2\ell-1)} \right]^{1/2} \Bigg\} \end{aligned} \tag{2.32}$$

Recalling the recurrence relation for spherical harmonics,

$$\cos\theta Y_{\ell,m} = \frac{(\ell - m + 1)}{\sqrt{(2\ell+1)(2\ell+3)}} Y_{\ell+1,m} + \frac{(\ell + m)}{\sqrt{(2\ell+1)(2\ell-1)}} Y_{\ell-1,m} \tag{2.33}$$

and the property of spherical harmonics $Y^*_{\ell,m} = -Y_{\ell,-m}$, Equation 2.33 can be rewritten to yield:

$$\begin{aligned}\cos\theta Y_{\ell,m} &= \left[\frac{(\ell-m+1)(\ell+m+1)}{(2\ell+1)(2\ell+3)}\right]^{1/2} Y_{\ell+1,m} + \left[\frac{(\ell+m)(\ell-m)}{(2\ell+1)(2\ell-1)}\right]^{1/2} Y_{\ell-1,m} \\ &= \left[\frac{(\ell+1)^2-m^2}{(2\ell+1)(2\ell+3)}\right]^{1/2} Y_{\ell+1,m} + \left[\frac{\ell^{\,2}-m^2}{(2\ell+1)(2\ell-1)}\right]^{1/2} Y_{\ell-1,m}\end{aligned} \tag{2.34}$$

Squaring the final form of Equation 2.34 produces the result

$$\begin{aligned}\sum_m \cos^2\theta \mid Y_{\ell,m} \mid^2 = \sum_m \Bigg\{ &\left[\frac{(\ell+1)^2-m^2}{(2\ell+1)(2\ell+3)}\right] \mid Y_{\ell+1,m} \mid^2 + \left[\frac{\ell^{\,2}-m^2}{(2\ell+1)(2\ell-1)}\right] \mid Y_{\ell-1,m} \mid^2 \\ &+ 2\left[\frac{(\ell+1)^2-m^2}{(2\ell+1)(2\ell+3)}\right]^{1/2} \left[\frac{\ell^{\,2}-m^2}{(2\ell+1)(2\ell-1)}\right]^{1/2} Y^*_{\ell+1,m} Y_{\ell-1,m} \Bigg\}\end{aligned} \tag{2.35}$$

Here the cross terms $Y^*_{\ell+1,m}Y_{\ell-1,m}$ and $Y_{\ell+1,m}Y^*_{\ell-1,m}$ are equivalent. Comparing the terms in 2.34 to those in 2.31 and using the identities

$$\sum_m \mid Y_{\ell,m} \mid^2 = \frac{2\ell+1}{4\pi} \tag{2.36a}$$

$$\sum_m m^2 \mid Y_{\ell,m} \mid^2 = \frac{\ell(\ell+1)(2\ell+1)\sin^2\theta}{8\pi} \tag{2.36b}$$

$$\sum_m m^4 \mid Y_{\ell,m} \mid^2 = \frac{(2\ell+1)}{8\pi}\left[\ell(\ell+1)\sin^2\theta + \frac{3}{4}\ell(\ell-1)(\ell+1)(\ell+2)\sin^4\theta\right] \tag{2.36c}$$

the following results are obtained, which have been rewritten in terms of $\cos^2\theta$ (by the identity $\sin^2\theta$ = 1-$\cos^2\theta$):

$$\sum_m \left[\frac{(\ell+1)^2-m}{(2\ell+1)(2\ell+3)}\right] \mid Y_{\ell+1,m} \mid^2 = \frac{\ell(\ell+1)+(\ell+1)(\ell+2)\cos^2\theta}{8\pi(2\ell+1)} \tag{2.37a}$$

$$\sum_m \left[\frac{\ell^2 - m^2}{(2\ell+1)(2\ell-1)}\right] \mid Y_{\ell-1,m} \mid^2 = \frac{\ell(\ell+1) + \ell(\ell-1)\cos^2\theta}{8\pi(2\ell+1)} \tag{2.37b}$$

$$2\sum_m \frac{1}{2\ell+1}\left[\frac{((\ell+1)^2 - m^2)(\ell^2 - m^2)}{(2\ell+3)(2\ell-1)}\right]^{1/2} Y^*_{\ell+1,m} Y_{\ell-1,m} = \frac{\ell(\ell+1) - 3\ell(\ell+1)\cos^2\theta}{8\pi(2\ell+1)} \tag{2.37c}$$

These relations 2.37a-c may then be substituted back into Equation 2.32. Gathering up those terms that contain $\cos^2\theta$ allows the resulting equation to be rewritten as

$$\frac{d\sigma}{d\Omega} = \frac{2\pi}{2\ell+1}\left\{\ell(\ell+1)\left[\Re^2_{\ell+1} + \Re^2_{\ell-1} + 2\Re_{\ell+1}\Re_{\ell-1}\cos(\delta_{\ell+1} - \delta_{\ell-1})\right]\right.$$
$$\left. + \left[(\ell+1)(\ell+2)\Re^2_{\ell+1} + \ell(\ell-1)\Re^2_{\ell-1} - 6\ell(\ell+1)\Re_{\ell+1}\Re_{\ell-1}\cos(\delta_{\ell+1} - \delta_{\ell-1})\right]\cos^2\theta\right\} \tag{2.38}$$

Here, the first line of Equation 2.38 corresponds to term A and the second line term B of Equation 2.24. Rearranging these quantities in the form of Equation 2.25 and canceling like terms gives a final form:

$$\beta = \frac{\ell(\ell-1)\Re^2_{\ell-1} + (\ell+1)(\ell+2)\Re^2_{\ell+1} - 6\ell(\ell+1)\Re_{\ell+1}\Re_{\ell-1}\cos\delta_\ell}{(2\ell+1)[\ell\,\Re^2_{\ell-1} + (\ell+1)\Re^2_{\ell+1}]} \tag{2.39}$$

It is straightforward to demonstrate that ℓ=0 produces a PAD independent of θ, which is an isotropic distribution. It is also notable that this expression of the angular anisotropy parameter correctly describes the perpendicular ($-\beta$) PAD arising from photodetachment from p-shell orbitals, such as those observed by Hall and Siegel for O^- and C^-, an effect due to interference between the two energetically equivalent detachment channels $\ell+1$ and $\ell-1$.[28]

Inspecting the form of Equation 2.39, it is clear that in addition to dependence upon the angular momentum of the parent orbital, β is also proportional the partial wave cross sections (through the amplitudes of the radial matrix elements) as well as

the overall phase shift between the two outgoing waves. In the absence of any external influences, the dominant long-range potential is the centrifugal interaction. The explicit form of the radial function $R_{k,\ell}$ in Equation 2.7b contains a term $\exp(i\pi/2\ell)$, a natural phase shift of π between the outgoing waves $\ell+1$ and $\ell-1$ imposed by the centrifugal interaction. The term $\delta_\ell = \delta_{\ell+1} - \delta_{\ell-1}$, is defined as the coulomb phase shift in the photoionization derivation of Bethe. In the absence of a coulomb potential, δ_ℓ represents a generic, additional phase shift between the two outgoing waves, sensitive to whatever potentials the electron might sample as it departs. In typical cases of atomic photodetachment, this $\cos\delta_\ell$ term is near unity. In cases where additional interaction with the outgoing electron takes place, change in this overall phase shift is reflected in the PAD. The addition of dipolar solvent molecules, in particular molecules that are effective scatterers of low energy electrons, can bring about changes in both the partial wave photodetachment amplitudes and phase shifts. Therefore, to the extent that scattering interactions between the photodetached electron and solvent molecules within a cluster anion occur, the evolution of the PAD as a function of eKE should manifest these interactions.

2.2.2 Approximation to β

Although the Cooper-Zare formulation of the β parameter can provide very useful insight of the angular anisotropy of the PAD, generation of theoretical β values by this method requires calculation of the dipole approximated radial matrix elements of both detachment channels. A valuable approximation to this method was devised by Hanstorp, Bengtsson and Larson.[29] These authors assume the validity of Wigner threshold behavior at energies further from threshold. In the limit that the centrifugal potential presents the sole electron-neutral interaction, the term $\cos\delta_\ell = 1$. Relating

the cross section as defined in the Wigner threshold law to the radial matrix elements yields:

$$\Re_{\ell\pm1} \propto k^{\ell\pm1} \tag{2.40}$$

A ratio of the dipole allowed radial matrix elements produces a relation that varies as a function of eKE

$$\frac{\Re_{\ell+1}}{\Re_{\ell-1}} \propto k^2 = A \cdot \mathrm{eKE} \tag{2.41}$$

Where A is a proportionality coefficient that scales with the "size" of the parent orbital. This relation holds quite well at relatively low energies.[19, 20, 29] Substitution of relation 2.41 into the Cooper-Zare equation (2.39) produces

$$\beta = \frac{\ell(\ell-1) + (\ell+1)(\ell+2)A^2 \cdot \mathrm{eKE}^2 - 6\ell(\ell+1)A \cdot \mathrm{eKE}\cos(\delta_{\ell+1} - \delta_{\ell-1})}{(2\ell+1)[\ell + (\ell+1)A^2 \cdot \mathrm{eKE}^2]} \tag{2.42}$$

The A and $\cos(\delta_{\ell+1} - \delta_{\ell-1})$ terms may be adjusted to fit experimental data. While the Wigner threshold law is strictly a valid descriptor of cross sections only at very low energies, when expressed as a ratio the higher order terms in k cancel. Anisotropy parameter values produced by this method are typically in good agreement with experiment at the low to intermediate energies studied here. An example of the application of this method is illustrated in Figure 2.5.

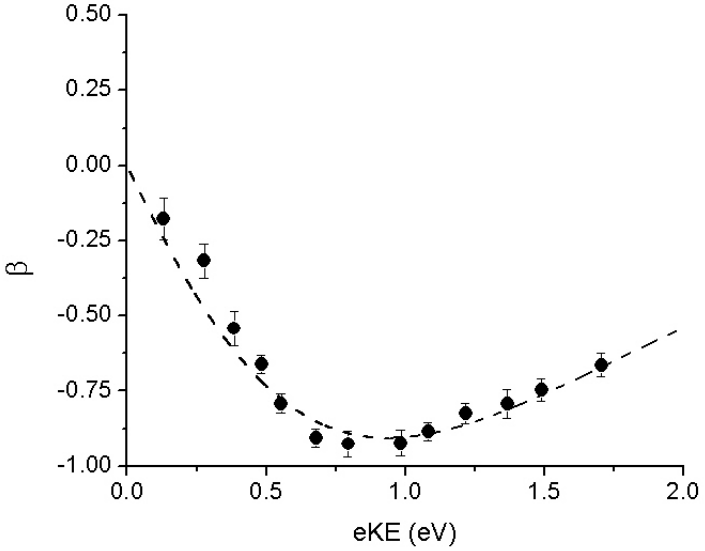

Figure 2.5: A fit of the Hanstorp-Bengtsson β parameter method to experimentally extracted values for I^- photodetachment (370-280 nm). The A and $\cos\delta_2 - \delta_0$ values are 0.52 and 0.93, respectively.

As mentioned in section 2.1.1, partial wave cross sections for $\ell > 0$ are suppressed near zero eKE. This is evident in figure 2.5, where the dominant s-wave character of the free electron wavefunction at low energies is reflected in the anisotropy parameter, which approaches zero at threshold. At higher eKEs, a d-wave component grows in, and the partial wave interference produces ever more negative β values until approximately eKE = 1 eV, at which point the progression begins to climb back toward positive 1. This behavior is typical of photodetachment from an atomic p-orbital. Deviations from this expected behavior may be indicative of interactions of the outgoing electron with its surroundings.

2.3 Electron Neutral Resonance Phenomena

Electron-neutral resonances may be broadly defined as transient negative ion species embedded in the scattering continuum of the neutral. Resonances are the product of electron-neutral collision processes, wherein the electron is captured for a finite period before decaying through a number of pathways. The most common is autodetachment, 2.43a, producing a neutral molecule and electron with final eKE equal to the incident eKE. Resonant vibrational excitation, illustrated in 2.43b, arises when the molecular framework is allowed to evolve on the timescale of the resonance decay, resulting in a non-equilibrium molecular geometry upon detachment ($\Delta v > 0$). Depending upon the lifetime of the resonance and the geometry of the potentials involved, such evolution may proceed into a region where the molecule is unstable with respect to production of a fragment anion. This results in dissociative electron attachment, shown schematically in 2.43c below. Resonance decay in molecular clusters may proceed through similar channels, as discussed in section 3.2.

$$MX(v) + e^-(E_i) \rightarrow MX^* \rightarrow MX(\Delta v = 0) + e^-(E_i) \tag{2.43a}$$

$$\rightarrow MX^* \rightarrow MX(\Delta v > 0) + e^-(E_i - E_{vib}) \tag{2.43b}$$

$$\rightarrow MX^* \rightarrow M + X^- \tag{2.43c}$$

In this manner, resonances act as important mediators of basic dynamical and chemical processes in molecules and molecular clusters.

In terms of a physical picture, resonance interactions are often classified as either single-particle or core-excited resonances[30, 31]. Single-particle or shape resonances are so called because they refer to the temporary capture of a single electron

by the potential arising from interaction with the ground state of the target atom or molecule. Generally this refers to an electron trapped within an orbital by a centrifugal barrier, thus the common appellation "shape" resonance, referring to the shape of the interaction potential. Shape resonances usually arise at energies greater than the ground state of the parent neutral. Given that the centrifugal potential varies $\propto \ell(\ell+1)/r^2$, shape resonances are not expected to occur for $\ell < 1$.

Core-excited resonances refer to the attachment of an electron to an the excited state of a neutral. The most common core excited resonances are Feshbach resonances. Electronic Feschbach resonances, described as an electron attached to an electronically excited state of a neutral atom or molecule, are usually found just below the energy of the associated parent state. Compared to shape resonances, electronic Feshbach resonances are generally longer lived, as they must decay to form an electronically less excited state than the parent state, requiring a change in electronic configuration.[30] Vibrational Feshbach resonances,[10, 32] also referred to as nuclear excited Feshbach resonances,[33, 34] can be described, by extension of the above definition, as an electron attached to a vibrationally excited state of a neutral polar molecule. Interaction of a low energy electron with the long-range dipole and polarization potentials of a polar molecule may give rise to a virtual anion state just below the threshold for a particular vibrational level. In the case that such a resonance occurs in the vicinity of a valence anion state, non-adiabatic coupling of the states may occur, bringing about an anion or anion fragment. Evidence of such a resonance associated with the ν_3=1 level in CH_3I, excited upon photodetachment from the $I^-{\cdot}CH_3I$ cluster anion, will be presented in chapter 4.

In electron scattering data, resonances are typically detected as narrow, intense enhancements in the scattering cross section. In the vicinity of the resonance, the

cross section is described by the Fano line shape function[35]

$$\sigma = \sigma_a \left[\frac{(q+\epsilon)^2}{1+\epsilon^2} \right] + \sigma_b \tag{2.44}$$

Here σ_a is proportional to the on-resonance cross section, σ_b is the backround scattering cross section, $q = -\cot \eta_\ell$, where η_ℓ is the background scattering phase shift for a given partial wave and $\epsilon = 2(E - E_r)/\Gamma$, where E_r is the resonance energy and Γ is the resonance width, defined in terms of the resonance phase shift as

$$\Gamma = \frac{2 \tan \zeta_\ell}{(E - E_r)} \tag{2.45}$$

where ζ_ℓ in this case refers to the resonance phase shift.[36] A resonance is said to occur when the resonance phase shift moves rapidly through π over a narrow energy range, with the cross section peaking at $\zeta_\ell = \pi/2$.[37] Examples, for various values of Q= $(q+\epsilon)^2/(1+\epsilon^2)$, can be found in figure 2.6. The shape of the cross section reflects the interference between the resonance and background scattering channels.

This same line shape function can also be used to describe the behavior of photoionization cross sections in the presence of autoionization resonances.[35, 38] In such cases, the q parameter describes the interference between direct ionization and resonant excitation (in the case of an autoionizing state, this is excitation to a rydberg state with an electronically excited core), as described in Figure 2.7. The q parameter can thus be described[39] as $C_1^2/(C_2 C_{12})$, where C_1 is the resonance excitation amplitude, C_2 is the direct photoionization amplitude, and C_{12} the coupling between the two channels (this is illustrated in Figure 2.7). Analogous structure has been observed in negative ion photodetachment.[40–43] It has further been illustrated that the anisotropy parameter β displays rapid variation in the presence of autoionozation

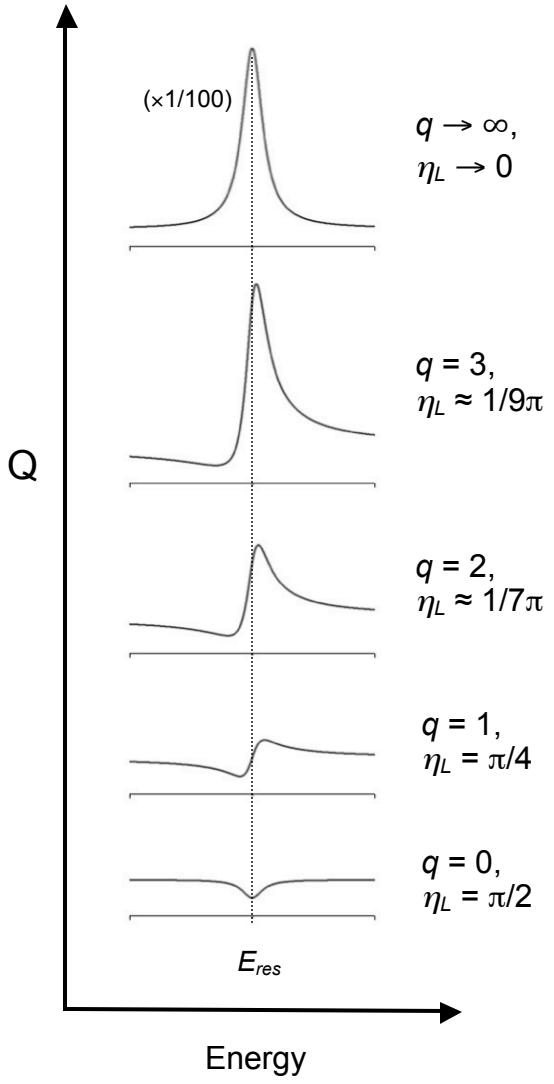

Figure 2.6: Variation in the Fano line shape Q parameter with q (see text for details). For $q \to \infty$ ($\eta_\ell = 0$, weak C_{12} coupling), an intense Lorentzian line shape is observed. For $q = 0$ ($\eta_\ell = \pi/2$, strong C_{12} coupling), a so-called "window resonance" is evident. Intermediate q produces an asymmetric profile.

resonances.[39, 44] Such resonances in the PAD scale with those observed in the cross section, although they are generally broader and may display small shifts in the peak energy.[45]

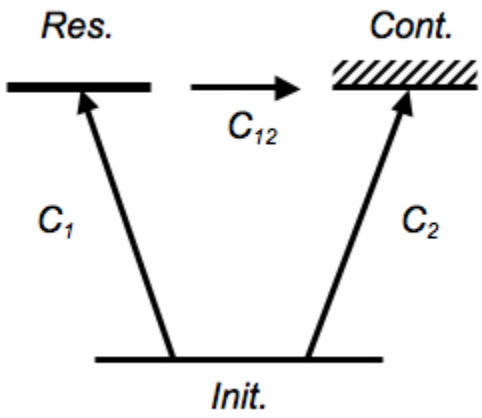

Figure 2.7: Schematic representation of multi-channel process underlying the asymmetric line shapes observed in photodetachment. C_2 represents direct the photodetachment channel, C_1 represents excitation to a discrete resonance state. C_{12} represents coupling of the resonance (*via* autodetachment) to the continuum.

Very limited studies of resonances in PADs associated with the electronic structure of solvent molecules within cluster anions have been undertaken to date.[21, 46] A major focus of this work involves the study of excitation of electron molecule resonances *via* electron transfer within cluster anions, recasting the C_1 transition referred to above as excitation to a resonant state in a neutral cluster constituent. The decay of such a resonance should be evinced in the PAD as interference between the decay channel and direct photodetachment.

2.4 Photoelectron Detection Methods

This section offers a brief summary of three types of widely implemented photoelectron spectrometers, two of them more traditional methods. The basic operating principles of the hemispherical sector analyzer, magnetic bottle spectrometer and charged particle and velocity-mapped imaging (VMI) detection will be outlined, as well as the relative advantages and disadvantages to these methods. In particular, the VMI method will be given considerable attention as this is the detection technique employed in this work.

2.4.1 Hemispherical Sector Spectrometer

The essence of the hemispherical sector spectrometer can be most simply described as a pair of hemispherical electrodes (or segments of two such hemispheres), the smaller nested inside the larger of the two. A cross sectional cut of such an arrangement is represented in Figure 2.8. Electrons enter the analyzer at P_i, while the detector position is P_f. The inner and outer electrodes are labelled E_{in} and E_{out}, respectively. In order for an electron to traverse the curved path (a circular orbit) of radius r with respect to a given point between P_i and P_f, the centripetal and radial forces must balance each other,

$$\frac{m_e v_0^2}{r_0} = eE_0 \tag{2.46}$$

Here E_0 is the applied field between E_{in} and E_{out} allowing an electron with velocity v_0 to traverse r_0, e is the charge of the electron and m_e the electron mass. For known

values of R_1 and R_2, the radial distances of the two electrodes, E_0 is described as [23]

$$E_0 = V_2 - V_1 = \frac{\text{eKE}}{e}(\text{R}_2/\text{R}_1 - \text{R}_1/\text{R}_2) \tag{2.47}$$

A point focus is achieved at 180°. A photoelectron spectrum over all energies can be obtained by scanning the potential difference $V_2 - V_1$ and measuring the resultant electron current while maintaining a constant anion and photon flux through the interaction volume.

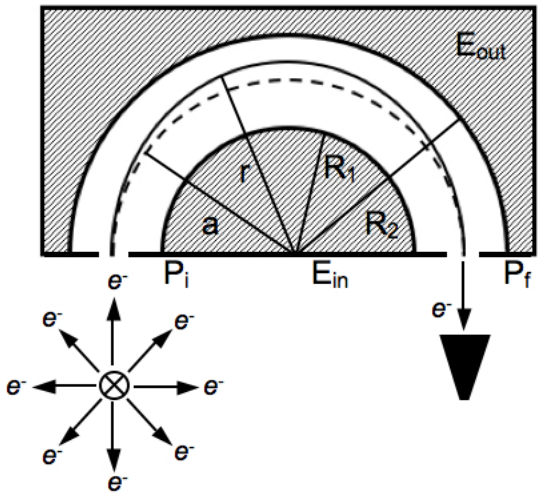

Figure 2.8: Schematic drawing of a cross sectional perspective of a hemispherical sector detector. Photoelectrons originate at the interaction volume (vector directed into the page represents the laser beam). A small solid angle of the photoelectron expansion enters at P_i. Those photoelectrons with a specified energy will traverse 180°, exiting at P_f. R_1 and R_2 represent the radii of the inner and outer hemispherical electrodes, respectively, **a** denotes the radial position of the optic axis and **r** illustrates the radius of the photoelectron trajectory at a given point within the sector.

The resolving power of this analyzer can be expressed (to first order assuming no relativistic effects) as[22]

$$\frac{\Delta E}{E} = \left|\frac{s}{2\text{a}}\right| + \left|C_1\alpha_r^2\right| + \left|C_2\alpha_z^2\right| \tag{2.48}$$

where s is the effective "width" of the electron source, a is the radius of the optic circle, α_r and α_z are the radial and azimuthal angles with respect to a ray extending from the the optic axis at the opening of the sector and C_1 and C_2 are aberration coefficients specific to the geometries of the sector in question.[22] $\Delta E/E$ of 0.0002 are achievable by this method. Resolving power scales with the distance traversed by the photoelectron (described by a in Equation 2.48). For this reason, multiple hemispherical sector analyzers may be used in series. The method is particularly useful for high eKE applications, where magnetic bottle and VMI based spectrometers tend to lose resolution.

While the excellent energy resolution capability of the hemispherical sector analyzer have made it a workhorse detection apparatus for decades, the most glaring shortcoming of the method is its modest detection efficiency. Energies of interest must be measured individually by carefully scanning a range of deflection potentials $V_2 - V_1$, and only a small fraction of the overall 3-dimensional distribution of electrons of a given energy will be accepted into the small solid angle of detection. In fact, in order to gather a photoelectron spectrum, the ion current, photon flux and overlap volume of the two beams must be carefully monitored throughout the experiment while maintaining the laser polarization vector at an angle of 54.7° with respect to the spectrometer entrance P_i. At this angle, the so-called "magic angle", the second Legendre polynomial $P_2(\cos\theta)$ is equal to zero, therefore the recorded intensity is directly proportional to the photodetachment cross section (Equation 2.21). The PAD evolves with eKE, so failure to carefully maintain this angle may introduce inconsistencies in the photoelectron spectrum.

These difficulties are amplified when measuring PADs. In this case, the potential $V_2 - V_1$ and photon energy must be held constant, while the angle of the laser

polarization is rotated, and the resultant variation in photoelectron current with polarization angle is measured. Care must again be taken to ensure that ion current, photon flux and overlap volume do not vary over the course of the measurements, the last being made more difficult through the necessary manipulation of the laser beam.

2.4.2 Magnetic Bottle Spectrometer

The magnetic bottle detector is essentially a time-of-flight detector, employing an inhomogeneous magnetic field to capture 2π steradians of the photoelectron distribution. This has a much greater collection efficiency than the hemispherical sector analyzer. For this reason, the magnetic bottle detector is well suited to detection of relatively weak, lower energy photoelectron signals. The high collection efficiency of the magnetic bottle was first realized by Kruit and Read[47], who situated the laser-target interaction volume between the pole pieces of a 1 T electromagnet, as illustrated in Figure 2.9. The Lorentz force, $e\mathbf{v}\times\mathbf{B}$, causes the nascent free electrons to spiral upward with frequency $\omega_i = e\mathbf{B_i}_i/m_e$ into a region of lower, homogeneous magnetic field maintained at $\sim 1\times10^{-3}$ T by a Helmholtz coil. This time-of-flight tube is shielded by μ-metal in order to diminish the influence of stray magnetic fields. Variation in z is assumed to be adiabatic, which is to say that the magnetic field changes negligibly in z within a single rotational period. This being the case, the equations

$$\frac{\sin\theta_f}{\sin\theta_i} = \frac{B_f}{B_i} \tag{2.49}$$

$$v_{zf} = v\left[1-(B_f/B_i)\sin^2\theta_i\right]^{1/2} \tag{2.50}$$

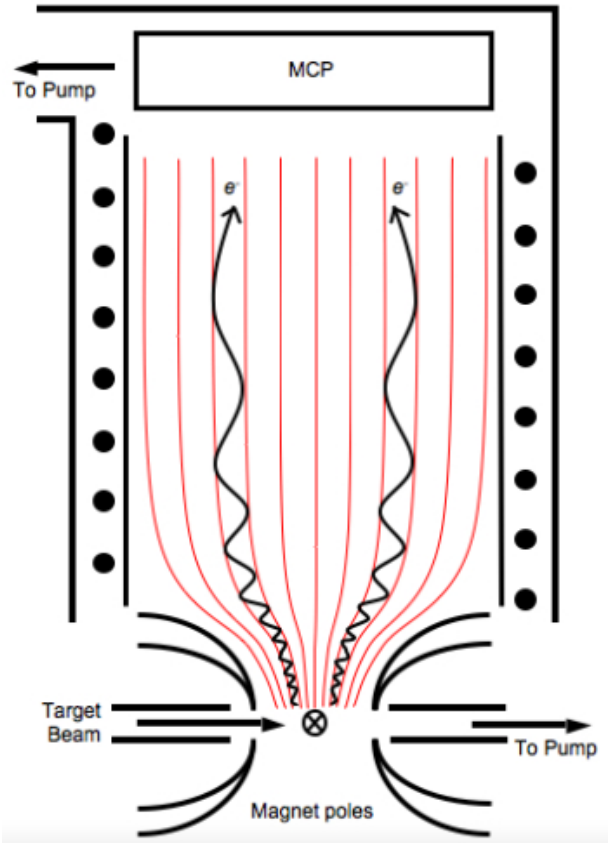

Figure 2.9: Schematic drawing of Magnetic bottle photoelectron spectrometer. The curved red lines describe the magnetic field. The vector pointing into the page represents the laser beam position. The photoelectrons are produced between the poles of an electromagnet and directed into a region of lower magnetic field maintained by a Helmholtz coil. The photoelectrons are detected at an MCP. Energy resolution is achieved by TOF.

describe the final velocity in the direction z aligned to the flight tube. For θ defined with respect to z, θ_f is very close to zero for most photoelectrons, a phenomenon referred to a parallelization.[47] Electrons with $\theta_i = \theta_f$ will, however, reach the detector slightly faster than those of for which $\theta_i > \theta_f$, giving the photoelectron distribution a temporal width ΔT. Resolution is limited by this factor ΔT by the relation

$$\frac{\Delta E}{E} = \frac{2\Delta T}{T} \tag{2.51}$$

In practice, the TOF (time-of-flight) tube is much longer than that displayed in figure 2.9 since T can be expected to increase more rapidly than ΔT with length. Typical flight tube lengths are in the range of 500 to 1000 mm. Design schemes implementing permanent magnets have also been successful, the key factor is establishing an overall gradient in the magnetic field of ~ 1 to 1×10^{-3} T. Spectrometers have also been developed for use with mass-selected fast ion beams [48, 49], where switched electric fields are applied in order to decelerate and focus the fast ions in the magnetic field prior to photodetachment. Energy resolution has also been improved since the initial design of Kruit and Read. The electrical impulse deceleration method [50] of Giniger et al. has produced $\Delta E/E \approx 0.02$ by using a pulsed electric field to preferentially reduce the velocities of electrons with $\theta_i = \theta_f$.

Determination of PADs with the magnetic bottle spectrometer is less straightforward. While measurement of angular distributions is not a strength of the magnetic bottle spectrometer, it is possible. Kruit and Read[47] demonstrated that the angular distribution can be measured by limiting the solid angle of electron acceptance through application of static electric fields and manipulation of the laser polarization. This approach is not unlike that taken in the study of PADs using the hemispherical sector analyzer. However, this diminishes the principal advantage of the magnetic bottle spectrometer, which is its broad acceptance angle, and given the requirement of additional electric fields to diminish the solid angle of acceptance, this approach is arguably more difficult. A new approach to collecting PADs with a magnetic bottle spectrometer while using a fixed laser polarization was recently proposed by Pedersen and coworkers [51], utilizing the inherent Doppler shift imparted upon electrons detached from fast ion beam. The anisotropy parameter for O^- photodetachment was

extracted from the state resolved photoelectron intensity profiles as a function of the TOF, producing β values similar to those reported using other detection techniques.

2.4.3 Velocity-Mapped Imaging

As discussed throughout this chapter, PADs contain a great deal of information pertaining to the character of the parent anion orbital, as well the long-range interactions of the neutral and free electron upon photodetachment. Until relatively recently, the collection of a PAD was a painstaking procedure, as detailed in the preceding sections. The introduction of velocity mapped imaging by Eppink and Parker [11, 12] marked a tremendous leap forward for charged ion imaging, and eventually photoelectron spectroscopy, in that it allowed for the simultaneous collection of spectra and angular distributions.

Velocity mapping built upon the 2-dimensional charged-particle imaging method of Chandler and Houston.[52] Charged-particle imaging, initially applied to imaging of ions, provides a very intuitive, direct measurement of the product fragment energy distribution, as well as angular information.

The original design of Chandler and Houston's charged-particle detector consisted, essentially, of a repeller plate positioned opposite a field-free TOF tube isolated from the repeller field by a fine, metal mesh. In a photodetachment experiment, the interaction of an anion with a plane polarized excitation laser centered within the linear repeller field produces electrons with velocity components v_x, v_y and v_z. The resulting momentum-space distribution of electrons is cylindrically symmetric around the polarization axis of the laser (z). The electrons are accelerated by the uniform electric field into the TOF region, where they drift at a velocity much greater than

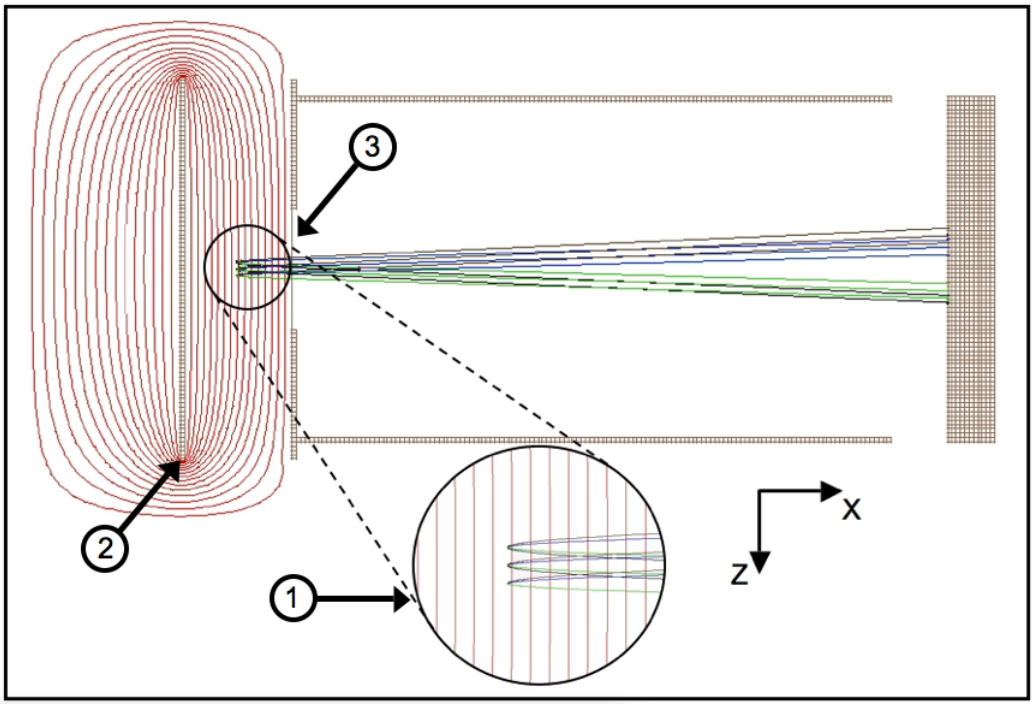

Figure 2.10: A simulation of a charged-particle imaging spectrometer of the design of Chandler and Houston. The interaction volume (1) contains 3 origin points, spaced over a 3 mm range (typical experimental laser beam diameter), each containing a collection of 4 different, color coded velocity components (brown, black, blue and green). The repeller (2) is held at -1000 V. A wire mesh (3) is referenced to ground, as is the TOF tube. The electric field is linear in the vicinity of the interaction volume, illustrated by the red equipotential lines. The electron trajectories, interaction volume size and TOF tube geometry are equivalent to those of Figure 2.11 to facilitate comparison.

that of their recoil velocity. This causes the Newton-sphere to flatten along the flight axis (x). As a result, only v_z and v_y are recorded; this is quite acceptable, though, due to the cylindrical symmetry of the expansion with respect to the laser polarization axis (section 2.2). The position, R, at which the particle impinges upon the detector is defined by R = $v_e \times$TOF, where v_e is the velocity component in the plane of the detector ($v_e = v_z + v_y$).[53] The repeller field is linear, so the spatial extent of the interaction volume (i.e. the range of initial positions) affects the extent of the velocity distribution at the detector. For an interaction volume of finite size, the velocity elements arising from photodetachment will be mapped onto a range of points on the

detector, producing a blurring of the image. Additionally, collisions with the grid reduce the number of electrons that reach the detector and local aberrations in the field homogeneity may be introduced by the grid, shifting the trajectories of electrons passing through.

Velocity mapping addresses these issues. A simulation of the velocity map imaging lens employed in this work is displayed in Figure 2.11, including equipotential curves (a schematic drawing of how the technique is implemented in this work can be found in Chapter 3, Figure 3.9). An additional extraction plate [(3) in Figure 2.11] of intermediate voltage is inserted between the repeller [(2) in Figure 2.11] and the ground plate [(4) in Figure 2.11] at the entrance to the electron TOF tube. Also, the 25 mm openings in the center of the extraction and ground plates are open; no mesh is used. This creates the lensing effect evident in the figure. The outcome of the lensing is to reduce spatial blurring of the image to an extent effectively equivalent to that assumed of a point interaction volume in the conventional arrangement. This is a tremendous advantage for anion photodetachment in particular, as space-charge effects limit the anion number density within the interaction region. Also, the removal of the mesh ensures 100% electron transmission to the detector. This provides for measurement of the position of all of the photoelectron impacts in a single experiment with fixed laser polarization.

The potentials applied to the plates can be found in the caption of Figure 2.11. These potentials can be adjusted in order to change the "size" of the image. Size, in this case, refers to the spatial extent of the photoelectron momentum distribution over the detector surface. Upon photodetachment, the 3-dimensional distribution of photoelectrons will expand at a rate limited by the photoelectron velocity. As in the Chandler and Houston arrangement, this momentum distribution is "flattened" along

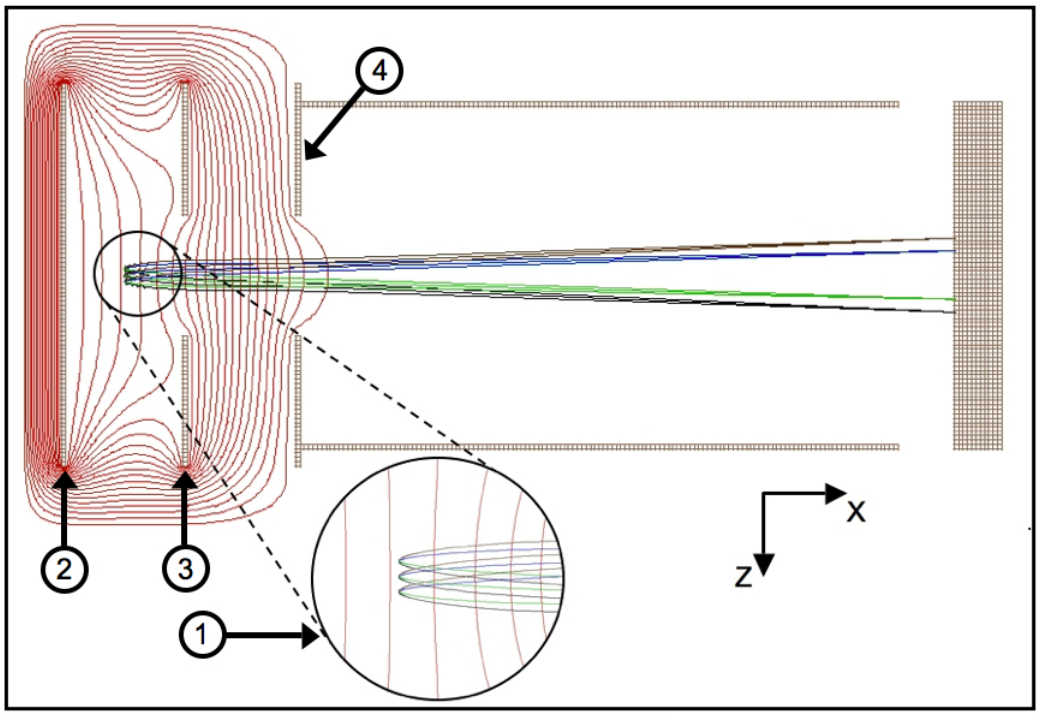

Figure 2.11: A simulation of the velocity-mapped imaging spectrometer employed in this work. The interaction volume (1) is defined in Figure 2.10 above. The repeller (2) is held at $-$V, the extraction plate (3) is held at $\sim -0.75\times$V and a third plate (4) is referenced to ground, as is the TOF tube. The resulting electrostatic lens is illustrated in red equipotential lines. At the far end of the TOF tube, each of the velocity groups is focused to a respective point upon the detector.

the TOF axis. Keeping the potentials of the electrodes fixed, the radial extent of the momentum distribution (R) scales linearly with the photoelectron velocity (V, defined above). The resolving power of the arrangement, R, scales as $\mathrm{eKE}^{(1/2)}$. Allowing the image to expand over a wide range of the detector for a fixed eKE provides greater detail in the image, while maintaining the potentials applied to the electrodes over a range of eKEs allows direct comparison of the momentum space images.

For the purposes of velocity map focusing, there is an optimum extractor to repeller voltage ratio (C) for a given electrode arrangement, aperture size and location of the interaction region.[53] Maintaining this ratio while altering the magnitudes of the potentials allows the experimenter to "scale" the size of the image.

While the energy resolution of VMI spectrometers is in general poorer than that of the hemispherical sector and magnetic bottle methods, newer methods such as that of Cavanagh, et al.[54] and the SEVI (slow electron velocity-mapped imaging) method of Neumark and coworkers[55] boast $\Delta E/E$ values as low as 0.0038. The spectrometer used in the current work is capable of a far more modest although quite acceptable value of 0.01.

The foremost advantage of the VMI spectrometer is the ease with which PADs and photoelectron spectra can be collected within a single experiment. This method allows for the eKE dependence of the PAD to be probed over a range of wavelengths without the requirement of changes in the laser polarization, variation of external fields or sacrifice of collection efficiency. Details specific to the implementation of the VMI technique in this work can be found in the following chapters.

Chapter 3

Experimental Methods

Much of the early work towards this dissertation comprised the design, construction and calibration of the photoelectron imaging spectrometer. What immediately follows is a brief description of that instrumentation. Individual aspects of the instrumental design and operation, as well as supplementary background material regarding experimental methods, are discussed in greater detail in subsequent sections.

3.1 Overview of Instrumentation

A schematic overview of the photoelectron imaging spectrometer can be found in Figure 3.1. Broadly speaking, it consists of a source chamber in which anionic species are produced, a time-of-flight mass spectrometer allowing selection of anions of interest and a detection chamber in which electrons are photodetached and detected using the velocity-mapped imaging (VMI) technique. Beginning with the source chamber, the atomic or molecular species of interest is entrained within a carrier gas (typically argon) and introduced to the chamber through a pulsed nozzle (general valve series 9, Parker-Hannifin). Reservoir pressures range from 15-80 psig, depending

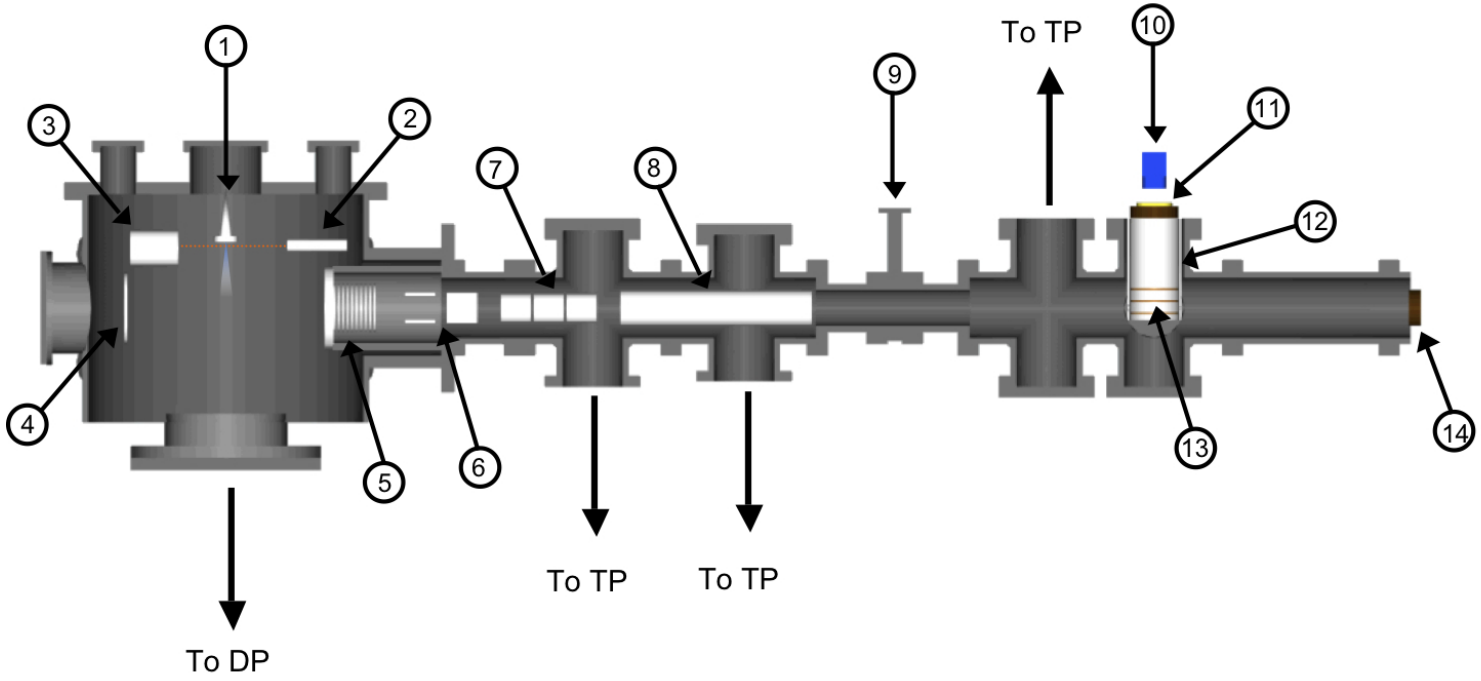

Figure 3.1: Schematic of the photoelectron imaging spectrometer. (1) Pulsed nozzle, (2) electron gun, (3) faraday cup, (4) TOF repeller plate, (5) extraction plate and acceleration stack, (6) electrostatic deflectors, (7) einzel lens, (8) potential switch, (9) 6" gate valve, (10) CCD camera, (11) imaging MCP and phosphor screen, (12) μ-metal sheilded electron flight-tube, (13) VMI lensing plates, (14) ion detection MCP.

upon the sample and the desired cluster anion, while the source chamber is held at a base pressure of 1×10^{-6} torr by a diffusion pump (Leybold DIP 8000, 8000 L s^{-1}) positioned opposite the nozzle. The diffusion pump is backed by a mechanical pump (Leybold D40, 920 L min^{-1}). The base pressure in the source region rises to $2\text{-}5\times10^{-5}$ torr during operation, allowing the sample to expand supersonically. Anions are prepared using one of two methods; electron impact ionization or pulsed discharge ionization. A complete discussion of these ion preparation techniques can be found in section 3.2. Both methods, coupled with the jet cooled source, produce a variety of stable monomer and cluster-anion species.

The anions generated are extracted from the jet by a negatively-biased high-voltage (HV) pulse and separated by mass within the Wiley-McLaren time-of-flight (TOF) mass spectrometer stage of the instrument.[56]

The arrival of the ion packet at the VMI detector is timed to be coincident with a detachment laser pulse (section 3.4), liberating the excess electrons. The residual neutral species continue to propagate out of the detection region, while the resulting photoelectrons are deflected into a 6 in. field-free flight tube by a 3-plate electrostatic lensing configuration (Figure 3.5). The flight tube, oriented perpendicular to the shared plane of the laser and ion beams, is shielded by 2 annealed layers of μ-metal surface. At the end of the flight tube is an imaging quality microchannel plate coupled to a phosphor screen detector with a charge-coupled device (CCD) camera positioned above the phosphor, allowing the position of the individual electron impacts to be detected. Details of this imaging arrangement are presented in section 3.5. Over the course of thousands of laser shots, the collected sum of these photoelectron impacts produces the final image. Using any of a number of techniques (Section 3.6), a "central

slice" can be extracted from the reconstructed photoelectron momentum distribution. From this slice, the photoelectron spectrum and PADs can be produced.

The timing scheme of a typical experiment is illustrated in Figure 3.2. Briefly, an experimental cycle is set in motion by the firing of an IOTA One pulsed nozzle driver (Parker-Hanifin), which triggers the series 9 valve. The synchronous output of the IOTA One triggers a digital delay generator (Berkeley Nucleonics, BNC 565, 8 channels) which in turn triggers (from top to bottom in Figure 3.1) the laser, imaging MCP collection pulse (See section 3.5), the CCD camera shutter, discharge ionization source (in the case that this source is being used), TOF repeller plate, potential switch and the oscilloscope (LeCroy Wavejet 314A, 100 MHz), which displays the ion signal as a function of TOF. The digital delay generator allows for the relative delay times between the items listed above to be altered as necessary. The ion time of flight is determined as the time elapsed between the pulse of the TOF repeller plate and the detection of the ion at the ion MCP detector, situated 0.5 meters beyond the laser interaction region. This being the case, the laser must be fired several μs in advance of the arrival time of the ion packet at the detector (TOF time). A useful estimate for this time, Δt in Figure 3.2, has been found to be

$$\Delta t \approx 0.821 \times \mathrm{m}^{1/2} \tag{3.1}$$

where m is the mass in atomic mass units of the target anion and 0.821 is an instrument specific constant arrived at through measurement of Δt for different masses using a 1.95 keV ion beam potential.

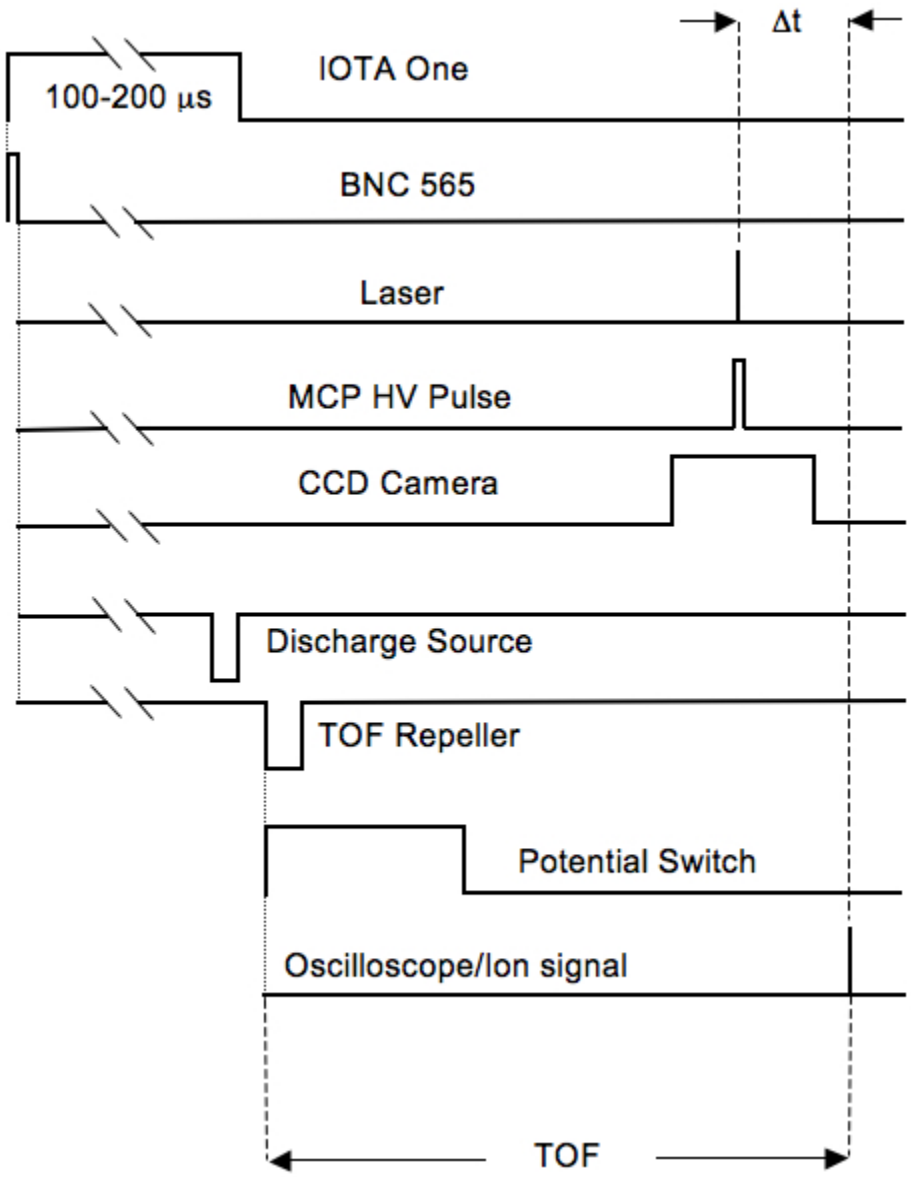

Figure 3.2: Schematic of the experimental timing sequence (see text for details)

3.2 Ion Preparation Techniques

The production of sufficient densities of negative ions in the gas phase can be challenging. Unlike positive ions, which can be generated by simple ionization of a parent neutral species, negative ions require the stable capture of an excess electron by a neutral target. Interaction of a free electron with a neutral target may produce a transient negative ion or negative ion resonance. Such species are formed in the electronic continuum of the neutral, and in the case of molecular electron attachment, at or near the equilibrium geometry of the parent molecule. Stable molecular anions generally have a ground state geometry different from that of the neutral. As such, these transient negative ion species are both electronically and geometrically unstable [57], often decaying through autodetachment on timescales ranging from femtoseconds to microseconds, depending largely upon the size (number of internal degrees of freedom of the target).[58, 59] The excess electronic energy of the transient anion must be disposed of on the timescale of the autodetachment lifetime in order to produce a stable anion. Several means of achieving this end are outlined below.

One mechanism by which a transient anion may decay to produce stable anionic species is dissociative electron attachment (DEA), represented in Equation 3.2.

$$\mathrm{MX} + e^- \rightarrow \mathrm{MX}^{*-} \rightarrow \mathrm{M} + \mathrm{X}^- \tag{3.2}$$

As the name implies, in the DEA process decay occurs through cleavage of the M-X bond. In many cases, such as the methyl halide species discussed in this work, no stable anionic states of the molecule exist (see for example Figures 4.1, 5.8 and accompanying text). DEA may also occur in cases where a stable anion state is present,

but simply inaccessible at attachment energy and geometry (for instance, attachment above the asymptotic dissociation limit of the anion state). Generation of the negative fragment necessitates a breakdown of the Born-Oppenheimer approximation. The transient species, prepared at the equilibrium geometry of the neutral, must relax by converting electronic energy into nuclear motion. If this relaxation proceeds rapidly enough that the M-X bond length exceeds the neutral anion curve-crossing point within the lifetime of the transient anion, the bond is broken and the anion fragment X^- is produced. DEA is a common means of atomic halide anion production, as cleavage of the R-X (X=F, Cl, Br or I) bond in alkyl halides is favored by the relatively low-lying σ^* antibonding orbitals as well as the high electron affinities of the halogens.

For cases of parent neutrals possessing positive electron affinities, production of anions through three-body association presents another means of electron capture[60, 61].

$$\mathrm{Ar} + \mathrm{M} + e^- \rightarrow \mathrm{Ar} \cdot \mathrm{M}^{*-} \rightarrow \mathrm{M}^- + \mathrm{Ar} \tag{3.3}$$

Here M is a target molecule (or atom) and Ar is a carrier gas atom. Interaction of M with the free electron produces a transient anion as in Equation 3.3. If the transient anion is sufficiently long lived, it may suffer a collision with the carrier gas prior to autodetachment. The internal energy of the transient anion is thus lost to the Ar atom as kinetic energy, yielding a stable anion. The introduction of low energy electrons into a supersonic expansion of target gas presents an ideal, high collision environment, as will be discussed at length below.

Particularly attractive targets for electron attachment are molecular or atomic clusters. The dynamics of this process shares aspects of both Equations 3.2 and 3.3.

Beginning with the cluster M_n,

$$M_n + e^- \rightarrow M_n^{*-} \rightarrow M_{n-x}^- + (M)_x \tag{3.4}$$

a transient cluster anion is generated. This cluster transient anion decays through loss of one or more monomer substituents, yielding the cluster anion M_{n-x}. This "evaporative" relaxation mechanism[62–64], operates similarly to the evaporative cooling of molecules within supersonic expansions. In the both cases, internal energy is lost as the kinetic energy of the evaporated monomer or monomers. Evaporative relaxation of cluster anions may be the most effective route to stable negative ions in that the "third body" is already present at the time of electron capture, therefore the autodetachment channel is suppressed. In addition to cluster anions, evaporative relaxation may also produce monomer anion species for sufficiently small ($n = x + 1$) or initially excited clusters. The rationale for this is illustrated in electron attachment to O_2 and $(O_2)_2$.[65][61] Comparing the attachment kinetics of the processes

$$O_2 + O_2 + e^- \rightarrow O_2^- + O_2 \tag{3.5}$$

$$(O_2)_2 + e^- \rightarrow O_2^- + O_2 \tag{3.6}$$

it is found that the second process (Equation 3.6) is roughly 10 times more favorable than the first (Equation 3.5), even allowing only 0.1% dimer concentration within the beam [65].

The ion production mechanisms outlined above are generally favored for lower energy free electrons and internally cold molecules. Lower energy electrons produce less highly excited transient anions which will generally have lower autodetachment

rates. Conditions favorable to electron attachment can be satisfied in general by introduction of low energy electrons to a supersonic expansion of gases.

3.2.1 The Pulsed Supersonic Expansion

Since its first implementation over 60 years ago, cooling of gas samples by supersonic expansion has since become an indispensable tool of molecular spectroscopists.[66, 67] Jet cooling of samples provides an intense source of neutrals at substantially lowered internal energy relative to the reservoir gas, as well as narrowing of group velocity. These attributes result in diminished spectral congestion and minimized doppler broadening. Additionally, and of particular interest to this work, clustering of atoms and molecules may also occur in supersonic jets.

The initial sample gas (a thermal sample of gas at temperature T_0, pressure p_0, and internal energy $U_0 = U_{trans} + U_{vib} + U_{rot}$) is held in the reservoir. This reservoir gas is allowed to flow into a second chamber through a small aperture of diameter D$<\lambda_0$, where λ_0 is the mean free path of the gas in the reservoir. The second chamber is held at a pressure p$\ll$p$_0$. Assuming the process to be adiabatic, the total energy of the sample gas is conserved as it passes from the reservoir to the vacuum. Although this neglects collisional heat transfer to the nozzle walls and enthalpies of cluster formation, this is essentially valid. An overall expression for the total energy of the gas can thus be written as

$$U_0 + \mathrm{p}_0 kT_0 + \frac{1}{2}\mathrm{m}u_0^2 = U + \mathrm{p}kT + \frac{1}{2}\mathrm{m}u^2 \tag{3.7}$$

where the left hand side represents the internal, potential and kinetic energy of the sample within the reservoir, and the right hand side represents the same for the sample upon passing through the aperture[16]. The symbols u_0 and u refer to the total mass transfer within the reservoir sample and the jet, respectively. A few simple assumptions regarding the terms in Equation 3.7 illustrate the change in the energy distribution of the sample gas upon expansion into the vacuum chamber. Overall

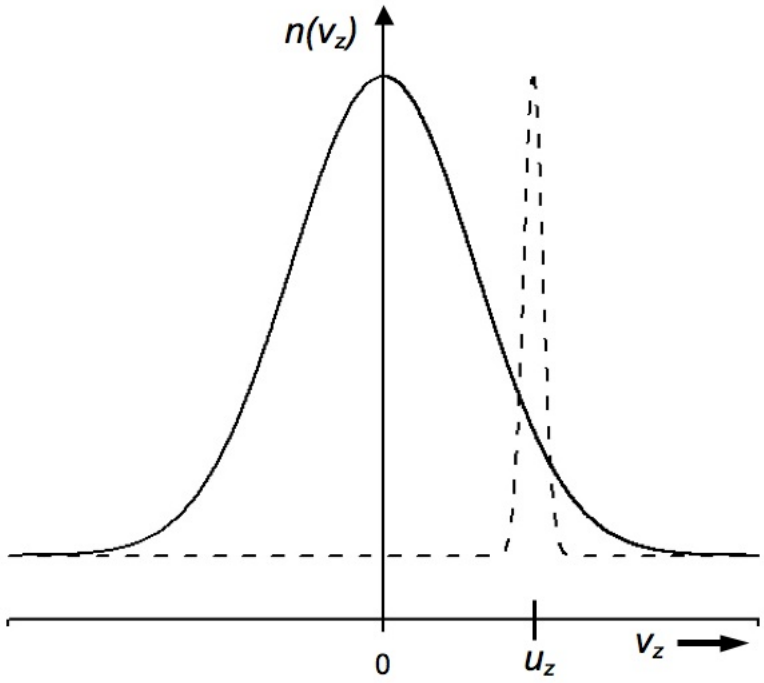

Figure 3.3: Comparison of a the reservoir gas velocity distribution in terms of v_z, the direction of flow through the nozzle orifice, at 273 K (solid line) and the resulting velocity distribution (dashed line) following supersonic expansion to Mach 10.

mass flow is randomized within the reservoir, therefore u_0=0. Within the vacuum chamber, the mass flow has strong directionality, such that at a distance r/D≥10, $u \approx u(z)$. The pressure within the vacuum chamber is sufficiently less than p_0 that it is neglected entirely. Inserting these results into Equation 3.7 yields

$$U_0 + p_0 k T_0 \approx U + \frac{1}{2} m u(z)^2 \tag{3.8}$$

The random motion of the reservoir gas is converted into strongly directional mass flow within the vacuum chamber, causing the fourth term to dominate the right hand side of Equation 3.8. It follows that U is far less than U_0, and so the molecules are internally cooled. Additionally, for r/D≥10 the velocity distribution within the jet may now be described by the modified Maxwell-Boltzmann [16] distribution

$$n(v_z) = N_0 exp\left(-\frac{m(v_z - u)^2}{2kT_{\parallel}}\right) \tag{3.9}$$

where $T_{\parallel}$ is the translational temperature, which serves as a measure of the width of the velocity distribution. This translational cooling is illustrated in Figure 3.3.

The collisions necessary to bring about such dramatic cooling occur only within jets that are supersonic (Mach number > 1) with respect to the surrounding vacuum. This condition is satisfied for a pressure differential $(p_0 - p)$ maintained at

$$(\mathrm{p_0 - p}) > \left(\frac{\gamma + 1}{2}\right)^{\gamma/(\gamma-1)} \tag{3.10}$$

throughout the lifetime of the expansion, where γ is the sample gas' ratio of heat capacities C_p/C_v.[68].

As mentioned above, at great distance from the aperture (r/D≥10), the range of velocities within the expansion is limited. Within this region of the expansion, the so-called "zone of silence", gas density is relatively low and collisions are relatively few [69]. The bulk of collisions occur much nearer to the orifice and dictate the extent of cooling and cluster formation. It is therefore important to understand the experimental parameters which bring about conditions favorable to cluster production in this limited region.

In thermodynamic terms, condensation of atomic and molecular clusters is favored when the vapor pressure of the condensing species falls below the local pressure in the jet. This pressure can be described as

$$p_s = pe^{-A/T} \tag{3.11}$$

where p_s is the condensing species' vapor pressure, p is the local pressure, A is a constant which depends upon the volume and surface tension of the condensate and T is the local temperature[16]. The keys to producing larger clusters are to decrease local temperature T while increasing residence time within the denser regions of the jet.

Assuming again that the expansion behaves isentropically, the local temperature T, pressure p and density ρ within the portion of the jet where collisions are occuring are described by the well known relation [68]

$$\frac{T}{T_0} = \left(\frac{p}{p_0}\right)^{(\gamma-1)/\gamma} = \left(\frac{\rho}{\rho_0}\right)^{(\gamma-1)} = \frac{1}{1+\frac{1}{2}(\gamma-1)\mathrm{M}^2} \tag{3.12}$$

where T_0, p_0 and ρ_0 are the source temperature, pressure and density and M is the mach number. Further, the mach number can be defined as [68]

$$\mathrm{M} = A\left(\frac{x}{\mathrm{D}}\right)^{\gamma-1} - \frac{(\gamma+1)/(\gamma-1)}{2A(x/\mathrm{D})^{\gamma-1}} \approx A\left(\frac{x}{\mathrm{D}}\right)^{\gamma-1} \tag{3.13}$$

where A is a constant, equal to 3.26 for monatomic gases. Inserting the far right-hand side of Equation 3.13 into Equation 3.12, it becomes apparent that $p \propto p_0\mathrm{D}$. It is also clear that the local temperature and density within the jet scale with $p_0\mathrm{D}$ as well. Binary collisions will increase with stagnation pressure and increasing nozzle aperature

diameter, D. In the case of 3-body collisions, the scaling is found experimentally to be $p_0 D^n$, where $0.5 < n < 1$, depending upon the species being expanded.[70–72] The strong dependence upon nozzle diameter, particularly with respect to three-body collisions, can be understood through consideration of Equation 3.13. For a fixed, terminal mach number, increasing D implies increasing x. As the flow rate varies relatively little with p_0[72], this has the effect of increasing the residence time of the gas in the denser region of the jet where collisions are likely to take place. Plots of the three-body collision rate as a function of both p_0 and D are found in Figure 3.4.[73, 74]

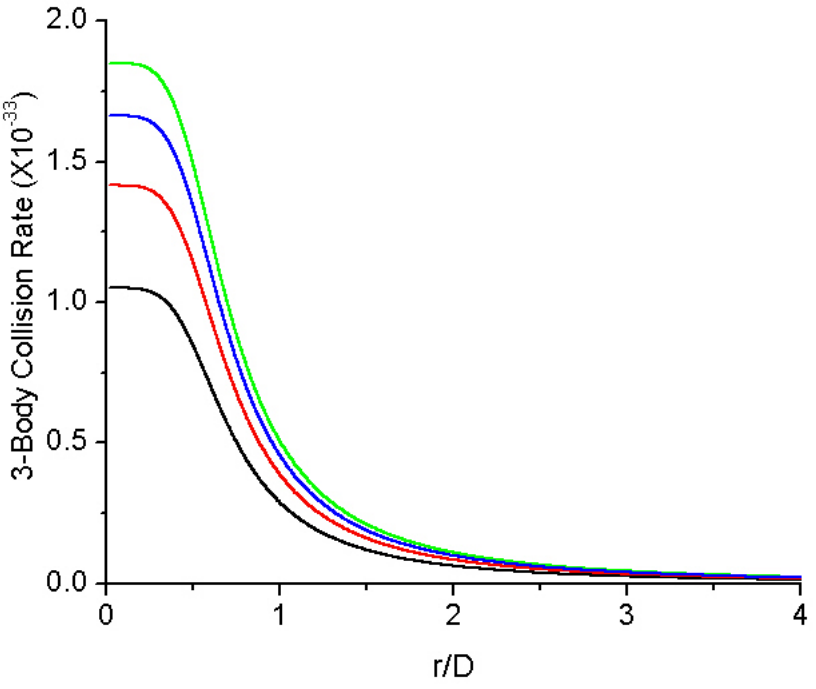

Figure 3.4: The calculated 3-body collision rate ($T^{1/2}$ cm^6 $atom^{-2}{\cdot}s^{-1}$) for argon expanding through a .75 mm diameter orifice into a vacuum as a function of distance (r/D) form the nozzle orifice. Stagnation pressures of 100 torr (black line) 700 torr (red line) 2000 torr (blue line) and 4000 torr (red line) are displayed. Increasing p_0 produces an increase in 3-body collision rate. Increasing D lengthens the range r/D in which collisions can be expected to occur.

3.2.2 Impact Ionization Method

It has been demonstrated for a wide variety of gas phase molecular species that low energy electrons (> 0.20 eV) are captured with great efficiency in comparison to higher energy electrons[75, 76]. With this in mind, a variety of methods for introducing low energy electrons into supersonic jets have been devised. Notable among these approaches are the alkali atom collisional electron transfer method of Bowen et al.[77], the laser photoelectron attachment method of Hotop and co-workers[78] and the heated-filament methods of Haberland[79] and Bowen[80]. While each of these approaches have advantages and disadvantages, the central problem faced is the inherently low flux of near-zero eKE electron sources due to space charge effects and the influence of stray fields. These problems can be largely addressed through application of the impact ionization method.

Impact ionization is a technique first applied to positive ion and cluster ion production over 30 years ago in the groups of Miller[81, 81], Zare[82] and Lineberger[83], among others. The method is applied, rather simply, by the interaction of a high energy (100-2000 eV) electron beam with the dense, immediate post-nozzle region of a supersonic gas expansion. What results is the ionization of the carrier gas by the high energy electron beam, producing a great amount of lower energy, secondary electrons. This cascading ionization process ultimately results in an electrically neutral, relatively cool plasma surrounding the jet[84]. The plasma has the advantages of providing both a low energy electron source as well as an electrostatically shielded region for ion production. The carrier gas employed throughout the work presented in chapters 4 through 7 of this work is argon.

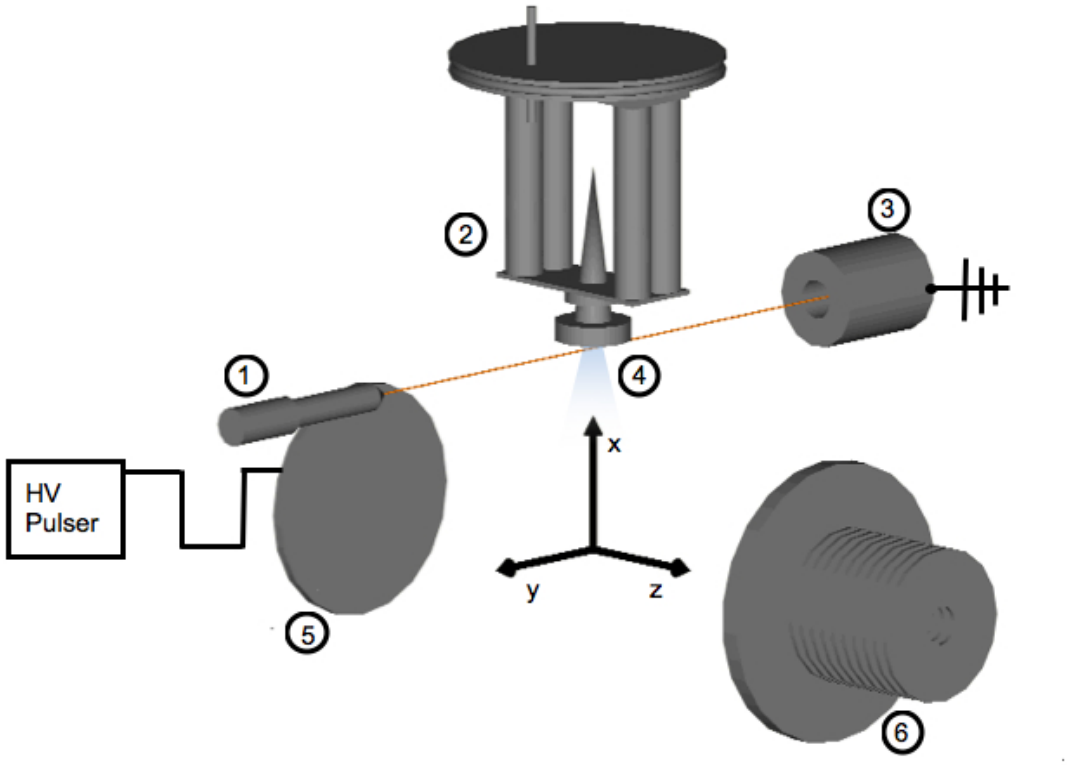

Figure 3.5: Schematic drawing of the electron impact ionization method. Items pictured include (1) the electron gun, (2) the pulsed-nozzle and mounting flange, (3) the Faraday cup, (4) the supersonic gas expansion, (5) the HV repeller plate and (6) the extraction plate and acceleration stack of the TOF mass spectrometer. The ion TOF axis is defined as z within the image.

The position of the electron beam with respect to the nozzle orifice is of importance to cluster ion production. In the case of positive ions, positioning of the electron beam within 1 nozzle diameter downstream has been found to produce the largest and greatest variety of cluster ions, while intersection of the jet further downstream produces a greater ratio of monomer cations[83, 84]. This is due to the fact that cluster cations form most effectively through nucleation around a monomer cation, thus generation of cations within a region of the expansion where collisions are still underway is critical.[84] Cluster anion production, by comparison, shows a weaker

dependence upon the intersection point of the electron beam and the jet.[84] Cluster anions, as mentioned in section 3.2, are most efficiently produced by evaporative cooling of a transient cluster anion, suggesting that a distance of r/D>5 (see Figure 3.4) should be expected to produce clusters. Experimentally, the optimal position of the electron beam with respect to the nozzle orifice has been found to be very sensitive to other experimental conditions.

When employing the impact ionization method in this work, a nozzle with a 0.76 mm diameter orifice was employed. The immediate post-orifice region of the supersonic expansion was intersected with a 1000 eV beam produced by a Kimball Physics model EFG-7 electron gun (EGPS-1017 power supply, yttria coated iridium disc cathode). This electron gun is equipped with an einzel lens, deceleration grid, and electrostatic deflectors, allowing the beam to be focused and steered. The gun is mounted such that the output end is approximately 200 mm away from the nozzle and parallel to the nozzle faceplate. Residual electrons passing through the expansion are captured by a faraday cup positioned opposite the gun.

Temperatures of ion beams produced by impact ionization were not directly measured in this work. However, internal temperatures of ions produced in this manner have been reported to be comparable to neutral species cooled by supersonic expansion [84]. With respect to translational temperatures, the shielding effect of the electrically neutral plasma is important in that it prevents extensive deflection of the nascent ions by the ionizing electron beam.

3.2.3 Pulsed Discharge Method

More recently, the source chamber of the instrument has been modified to allow for another means of ion production, the pulsed discharge method. Having long been employed in the study jet cooled radicals and cations, extension of the method to the production of anions occurred relatively recently [54, 85, 86] The configuration of the pulsed discharge source utilized in this work was modeled after that of Osborn et al.[86], with several modifications. A schematic of the source can be seen in Figure 3.6.

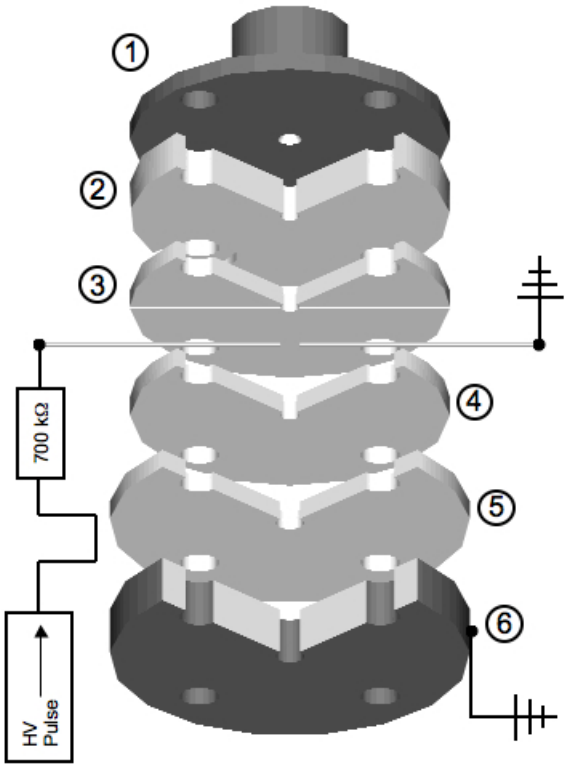

Figure 3.6: Exploded, cutaway drawing of the pulsed discharge ionization source. Components are described with thickness (T) and inner diameter (ID) in mm: (1) the pulsed nozzle faceplate, (2) teflon spacer [T=4, ID=2], (3-4) teflon spacers with .25 mm depth grooves to hold needles [T=2, ID=2], (5) teflon spacer [T=2, ID=3], (6) stainless steel end piece [T=5, ID=3].

It is composed of a series of small plates of different thickness and material, fixed to the faceplate of a series-9 pulsed nozzle (Parker-Hanifin). The insulating plates are made of teflon, while the conducting plates are made of stainless steel. In the arrangement displayed in Figure 3.6, the stainless steel ring electrode of Osborn et al.[86] has been substituted by a pair of 0.5 mm diameter needles sandwiched between two teflon plates.

Operation of the pulsed discharge source is very straightforward. As the pulse of gas is released from the nozzle, it passes between the needle electrodes, positioned 4.0-8.0 mm downstream from the orifice. Application of a HV pulse concomitant with the arrival of the gas produces a potential gradient sufficient to field ionize the carrier gas, producing a plasma between the needle points. In order to maintain the stability of the source, a ballast resistor (700 Ω) is placed on the supply side of the pulse and a very low current electron beam (≥ 1 μA) is passed over the outer aperture of the discharge source. This electron beam serves as a "seed" to the plasma, slowing recombination and preventing cations downstream from being drawn back against the current of the jet. The duration of the HV pulse is typically $\leq$10-15 μs, which is about 5% of the average nozzle pulse duration. It has been found that anion yield is maximized if the HV pulse is made to coincide with the leading edge of the of the gas pulse.

One advantage of the pulsed discharge source relative to the impact ionization source is the ease with which the plasma position can be held at a specific position within the jet. By adding or removing plates, the discharge can be placed closer to or further from the nozzle. For the purposes of cluster anion generation, a setup employing needles of 0.5 mm diameter placed 6 mm downstream from a 0.4 mm diameter nozzle proved optimal. 11 mm of additional plates were placed after the

needles. Lengthening of the "tube" appears to favor clustering[48, 85]. The needle points were held 1 mm apart and HV pulses applied ranged from 400-900 V.

This source, like the impact ionization source, is expected to produce anions that are comparable to neutrals within the jet in terms of internal temperature. Advantages of the discharge source compared to impact ionization are stability of signal and the relatively low electron beam currents required, which drastically extends the lifetime of the electron gun cathode.

3.3 TOF Mass Spectrometer

The ion optical components making up the TOF stage of the instrument are illustrated in Figure 3.1 [items (5-8)]. Newly created anions flow downward into the space between the TOF repeller plate and the extraction plate. A HV pulse, ranging from -700 to -950 V is applied (Directed Energy Inc. PVX-4140 pulse generator, Burle PF1053 power supply). The field strength that a given anion experiences depends upon its position with respect to the repeller plate. This has the effect of imparting greater acceleration upon those anions nearer the repeller, and less upon those nearer the extraction plate. This potential can be tuned to allow that the majority of the anions of a given mass reach the extraction plate at approximately the same time. The optimal value of the repeller potential varies with the mass of the species being studied, as well as the stagnation pressure of the sample.

Upon passing through an aperture in the extraction plate, the anions enter an acceleration region, wherein they are uniformly accelerated into a +1.950 kV field by a series of 10 stainless steel plates resistively coupled (10 MOhm per plate) to ground.

Referring to the well known relation $T = \frac{1}{2}mv_z^2$ where T is the kinetic energy, m the anion mass, and v_z the anion velocity in the direction of ion beam propagation, anions A_1 will travel the length of the flight tube at a velocity proportional to $m_1^{-1/2}$, while anions A_2 will travel at a velocity proportional to $m_2^{-1/2}$, and so on for other species. This of course assumes all anions possess a mass to charge ratio of 1, which is a good assumption for ions produced by the methods detailed above. The different anion species are thus separated into "packets". This region of the instrument is held at approximately 1×10^{-7} torr by a pair of turbo-molecular pumps (Leybold TMP 361, 360 L s^{-1}) backed by a rotary vane mechanical pump (Leybold D-16, 379 L min^{-1}).

In order to ensure that the anion packets are focused as tightly as possible in the detection region, a series of ion optics are employed. These include a pair (horizontal and vertical) of electrostatic deflection plates and an einzel lens. All of these components, with the exception of the central element of the einzel lens, are referenced to a potential of +1.950 kV by using an isolation transformer (DEL AD1640). Additional potentials are added to the deflectors (0 to ±140 V) using a pair of DC power supplies (Agilent E3630A, also referenced to +1.950 kV) resulting in a range of 1810-2090 V. The central element of the einzel lens can be varied from 0 to 2500 V (Stanford SRS PS325) to achieve optimal focus. The final ion optical element, the potential switch[87], re-references the 1.950 kV ion beam to the ground potential of the detection region. This allows the ion MCP and velocity-mapped imaging spectrometer to be operated at far more manageable potentials. The operation of the potential switch is very simple. The switch is composed of a long stainless steel tube (42 cm) with a 7.5 cm inner diameter and smaller 1.9 cm exit aperture. The tube is electrically isolated from the instrument by two teflon collars and connected to a HV pulser (DEI PVM-4140, Stanford SRS PS325 power supply). As illustrated

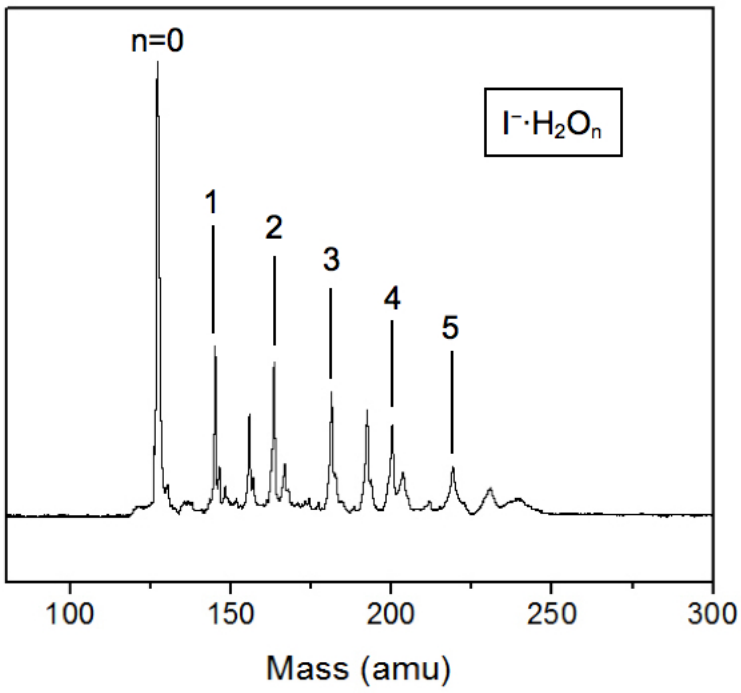

Figure 3.7: Sample mass spectrum displaying $I^-{\cdot}H_2O_n$, n=0-5. Anions were produced by passing 40 psig argon over separate samples of solid iodine and liquid water and expanding this mixture through the pulsed discharge ion source.

in Figure 3.2, the tube is pulsed to a potential of 1.950 kV, matching that of the acceleration region, at TOF=0 μs. This potential is maintained by the pulser until the anions of interest are within the tube. Within the tube, the field experienced by the anions is essentially zero. Provided the pulser is fast enough (quoted rise and fall time of the PVM-4140 is < 25 ns), the potential can be reduced to zero with the anions experiencing a negligible perturbation. The re-referenced anions then pass out the exit aperture and proceed toward the VMI lens.

Anions are detected at a MCP detector (Del-Mar Photonics, MCP-MA25/2, Burle PF1053 power supply) 0.5 m past the VMI lens. A sample mass spectrum is shown in Figure 3.7. Experimental Δm/m values of 0.39% are easily achievable, providing resolution that is more than adequate for the purpose of this work.

3.4 Laser System

The detachment laser used in this work was produced by a Spectra-Physics Sirah Cobra Stretch LG-24 dye laser. This laser was pumped by the s-polarized output of a Spectra-Physics Quanta-Ray INDI 40-10 Nd:YAG (yttrium aluminum garnet) laser, emitting at either the second or third harmonic (532, 355 nm, respectively). The pump laser produces pulses of 5-8 ns temporal width, with energies of ∼100 mJ (355 nm) to ∼200 mJ (532 nm).

The output of the dye laser is p-polarized prior to frequency doubling. The fundamental output is tunable over a range from 370-760 nm. Second harmonic generation (SHG), if desired, can be achieved through the motor-controlled rotation of a β-barium borate crystal (BBO) and beam compensator. The BBO used in this work allows SHG over a range from 380 to 250 nm. The s-polarized output of the BBO is separated from the residual fundamental beam by a series of Pellin-Broca prisms. The polarization of the second harmonic must be turned through 90° (such that it is polarized in the plane of the imaging detector) before being directed into the chamber. This is accomplished through the use of turning mirrors on the optical table.

The laser system was operated at a repetition rate of 10 Hz, producing pulses of ∼4 ns duration. The frequency doubled output is 98% p-polarized, with typical intensities in the range of 1-5$\times 10^7$ Wcm^{-2}.

3.5 Velocity-Mapped Imaging Spectrometer

A schematic drawing of the spectrometer used in this work is displayed in Figure 3.8. Three plate electrodes were used in this design, a repeller, an extraction plate and a ground plate. Each plate was 10.16 cm (4″) in diameter and 0.8 mm (1/32″) thick. The upper two plates (extraction and ground) each have a 25 mm (1″) diameter hole in the center to allow electrons to be pass through to the detector. The edges of the hole of the central plate are knife-edged in order to maximize field density in the vicinity of the openings. The plates are made of OFHC (oxygen free high conductivity) copper and were placed 25 mm (1″) apart on alumina (Al_2O_3) spacers to ensure that the plates are electrically isolated. The spacers were slid over 4 molybdenum threaded rods and held in place by molybdenum nuts. These plates were coated with a graphite aerosol in order to diminish generation of spurious photoelectrons by interaction of the copper surface (the work function of copper is Φ=4.7 eV) with scattered photons.[88] Potentials were supplied to the repeller and extractor plates by two Stanford SRS PS325 power supplies. The electron flight tube, from the top of the ground plate to the detector surface, is 12.5 cm (4.9″) long with an inner diameter of 7.2 cm (2.8″). It is lined both inside and outside with 0.35 mm thick μ-metal sheets to diminish the influence of permanent external fields, such as the earth's magnetic field, upon the electron trajectories.

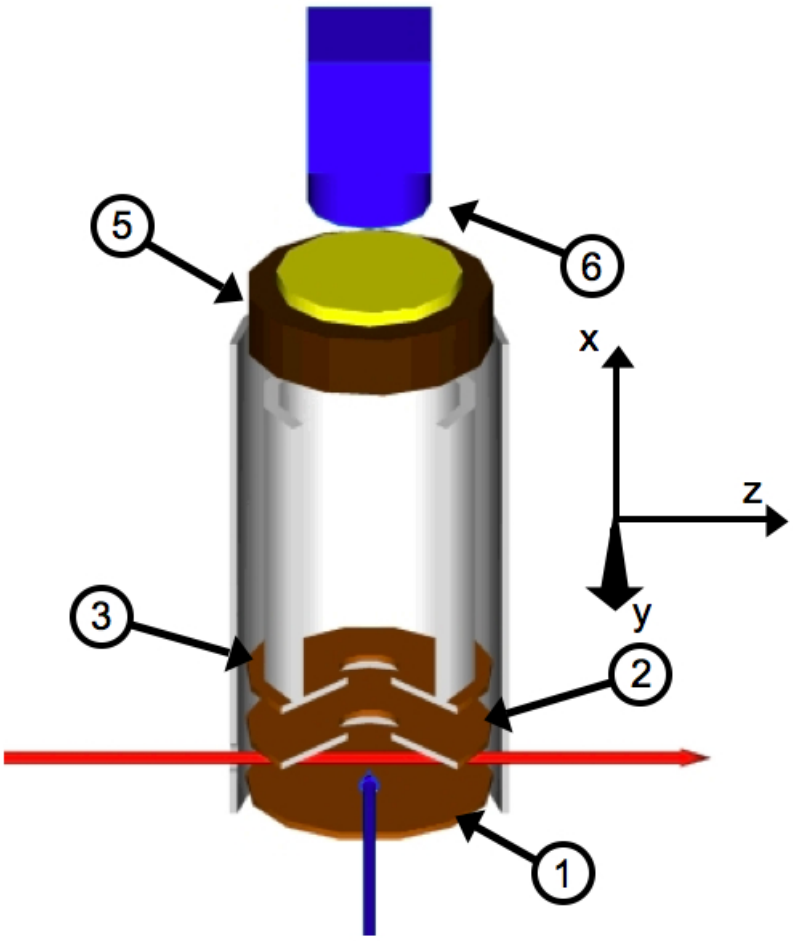

Figure 3.8: Schematic drawing of the VMI spectrometer, featuring the (1) repeller electrode (typically −300 to −1000 V), (2) extractor electrode (∼repeller×0.75 V), (3) ground electrode (5) imaging MCP/Phosphor detector, (6) CCD camera. The red ray represents the ion beam, while the blue represents the detachment laser beam, polarized in the yz plane of the detector. See text (sections 2.4.3 and 3.5) for further details.

The detector consists of a two chevron-stacked MCP plates (Burle, Inc. 40 mm Diameter, 10 micron pore pitch, MgO coating, Burle PF1054 power supply) coupled to a P20 phospor screen. The detector is electrically biased such that the vaccuum side is at 0 V (as is the TOF tube), while the back of the MCP stack is held at 1 kV. To discriminate against background electrons, an additional 0.85 kV pulse (DEI PVM-4210) is applied to the back of the MCP stack for a brief period surrounding the

arrival of the photoelectrons (∼200 ns). The gain across this MCP stack at 1.85 kV is on the order of 10^7. The phosphor screen is held between 2.5-3.5 kV (Burle PF1054). Pressure within the detection region of the instrument is maintained at 1-5$\times 10^{-9}$ torr during operation by a turbo-molecular pump (Leybold TMP 361) backed by a rotary vane mechanical pump (Leybold D-16).

Individual electron impact events, having been amplified by the MCP, are manifested as points of light on the phosphor screen. These impact events are recorded by a CCD camera (Imperx, Inc., IPX- VGA120-L, 640×480 pixels) and accumulated in 32 bit raw signal files using custom programmed collection software (VideoSavant 4.0, IO Industries). Typical signal collection cycles comprise 4000 to 8000 laser shots. An equal number of background laser shots, where the laser to ion packet timing (Δt of Equation 3.1) is detuned such that the laser does not interact with any ions (i.e. the target ions or other species present in the mass spectrum, typically a 5-10 μs shift), are also collected and stored as a 32 bit raw background file. Subtraction of this background from the signal produces the final image.

3.6 Data Extraction

The image process represents two-dimensional projection of the initially cylindrically symmetric three-dimensional momentum space distribution of photoelectrons onto the detector. In order to extract useful information from this data, a "central slice" of the original three-dimensional expansion is required. A variety of methods are available to achieve this end. These include experimental techniques such

as "slicing"[89–91], in which the central region of the newton-sphere is detected directly, and also mathematical treatments of the raw image which recreate the three-dimensional distribution from the two-dimensional projection. Slice imaging is most readily applied to ion imaging experiments, as photoelectrons require exceedingly fast-switching detectors. Therefore, this work relies on mathematical extraction of the "central slice". Examples of such mathematical techniques include the inverse Abel tranformation (displayed schematically in Figure 3.9), as well as the closely related basis set expansion (BASEX) method [92], the Onion peeling method[93], and the iterative procedure of Vrakking[94], among others. The inverse Abel transformation reconstruction method is discussed in greater detail in appendix A.

Given the central slice of the photoelectron momentum distribution, the photoelectron spectrum and angular distribution can be extracted. The energy domain distribution (spectrum) is arrived at through calculation of the eKE, which is proportional to r^2 in the momentum domain. The relation between r and v_e, the electron velocity, is linear. Through implementation of the Jacobian transformation

$$P(\text{eKE}) = P(v_e)/v_e \tag{3.14}$$

where $P(\text{eKE})$ is the intensity as a function of eKE and $P(v_e)$ is the intensity as a function of electron velocity, the energy space distribution is recovered.

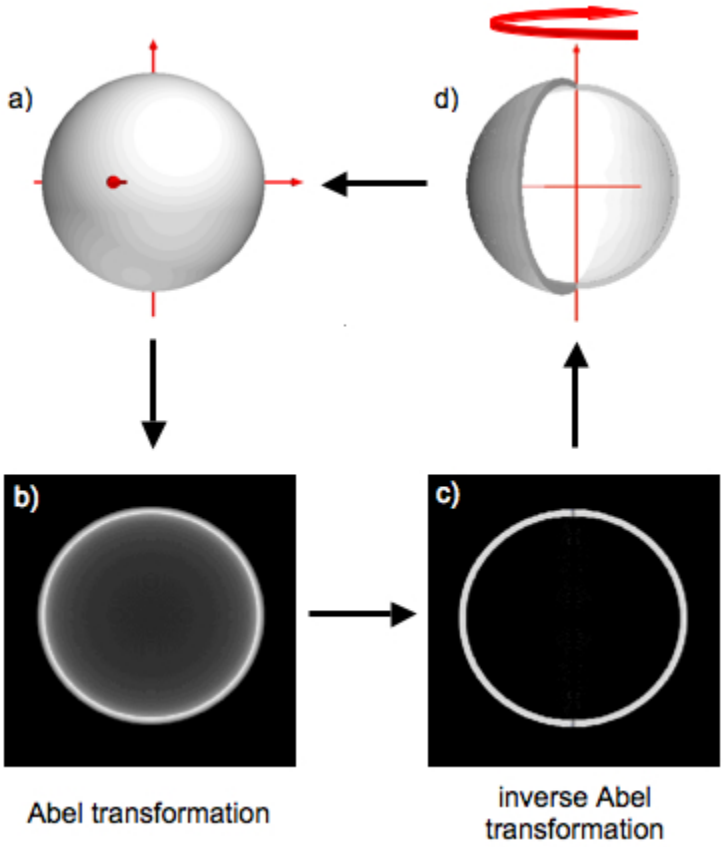

Figure 3.9: Schematic representation of image reconstruction *via* the Abel and inverse Abel transformations. The 3-dimensional distribution (a) is projected in two dimensions (b) on the detector. The inverse Abel transformation (c) extracts a central slice of this image, and rotation about the symmetry axis (d) restores the original distribution.

The PAD, for the case of single-photon detachment, is described by the function $I(\theta) = (\sigma/4\pi)[1 + \beta P_2(\cos\theta)]$ of chapter 2 (Equation 2.21). Given a particular radial range r, typically defined by the full width at half maximum (FWHM) of a spectral feature of interest, the intensity as a function of θ may be extracted from the reconstructed image. Plotting $I(\theta)$ versus $P_2(\cos\theta)$ produces a linear relationship. A linear regression of this plotted data yeilds $\beta =$ slope/intercept.

3.6.1 Instrumental Calibration: Superoxide Photodetachment

The custom-built instrument used in this work was calibrated using the widely studied superoxide anion. The image displayed in Figure 3.10 was produced through 460 nm photodetachment from O_2^-. O_2^- was prepared by impact ionization of neat O_2 at 15 psig stagnation pressure.

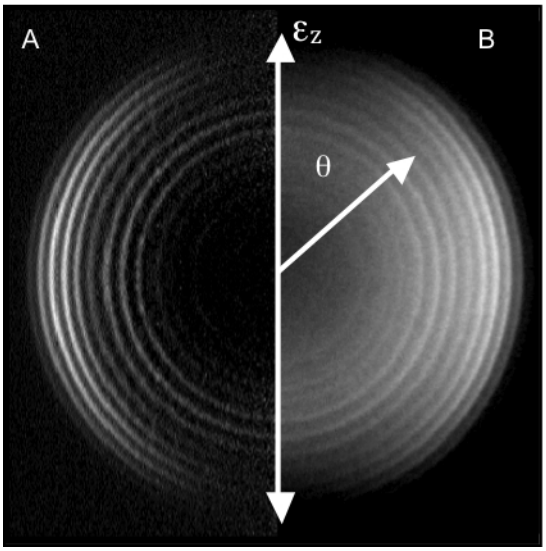

Figure 3.10: Photodetachment from O_2^- at 460 nm. The left-hand side of the image (A) shows the central slice of the momentum space photoelectron distribution extracted *via* the BASEX method. The right-hand side (B) shows the raw image. The laser polarization vector is denoted as σ_z, and the photoejection angle with respect to σ_z is θ.

The concentric rings in the image correspond to transitions to vibrational levels of the neutral molecule accessed *via* the transitions

$$O_2\,(X^3\Sigma_g^-) + e^- \leftarrow O_2^-\,(^2\Pi_g) + h\nu\,(460nm) \tag{3.15a}$$

$$O_2\,(a^1\Delta_g) + e^- \leftarrow O_2^-\,(^2\Pi_g) + h\nu\,(460nm) \tag{3.15b}$$

The outermost rings, those with the highest velocities, correspond to photodetachment *via* the ground state of the neutral, (Equation 3.15a). The innermost rings, which are clearly more isotropic with respect to θ than the outer rings, correspond to photodetachment producing the first excited electronic state of neutral oxygen (Equation 3.15b).

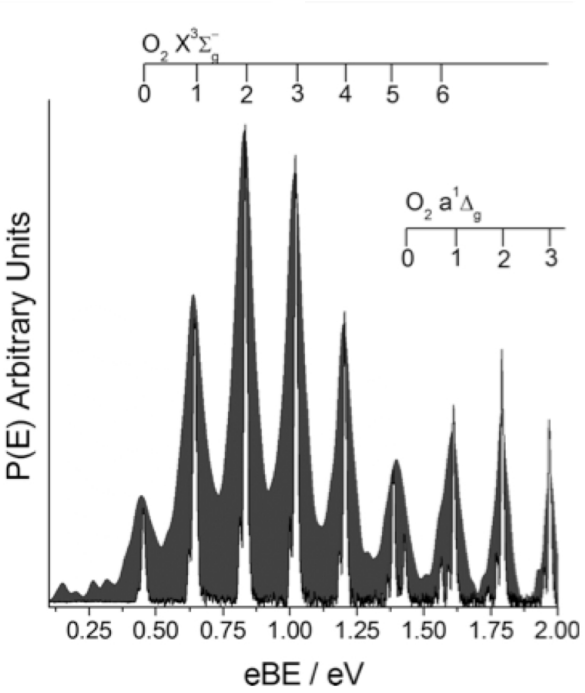

Figure 3.11: Photoelectron spectrum for 460 nm detachment from O_2^- (Grey, this laboratory) and photoelectron spectrum for 454.57 nm (white, ANU data), displayed in terms of eBE. The grey spectrum was taken from the image shown in Figure 3.9 above. Vibrational levels are labelled for the $X^3\Sigma_g^-$ (X) ground electronic state and $a^1\Delta_g$ (a) first excited electronic state of O_2. (Reproduced with permission from *The Journal of Chemical Physics*, Van Duzor *et al.*, Nov. 2010, Vol. 133 174311-174320 ©2010 *American Institute of Physics*.)

The left-hand side of the image, labeled (A), displays the central slice of the photoelectron momentum distribution, reconstructed using the BASEX program.[92] This reconstruction provides a spectrum in the radial domain of the detector, $P(r)$. Conversion of this radial spectrum to the energy domain is accomplished using the

following relationship:

$$\text{eKE} = \left(\frac{hc}{\lambda} - \text{eBE}_i\right) \times \left(\frac{r_i}{r}\right)^2 \tag{3.16}$$

Here eBE_i is the electron binding energy (eV) of a specific spectral feature serving as the point of calibration, λ is the detachment wavelength, r_i is the radial position of the calibration peak. For the case of detachment accessing the ground vibrational level of the X state of O_2, eBE_i is 0.45 eV.[95] Conversion of the radial spectrum to the energy domain allows the photoelectron velocities to be explicitly calculated as $v_e = (2eKE/m_e)^{1/2}$. Recalling that $P(r)$ is linearly proportional to $P(v_e)$ and utilizing the Jacobian transformation (Equation 3.14), the spectrum $P(\text{eKE})$ is produced.

The darker of the spectra shown in Figure 3.11 was extracted from the image displayed in Figure 3.10 and was calibrated from the major peak (v=2, X state, 0.8318 eV, eBE)[95]. This spectrum is displayed in terms of eBE ($h\nu - \text{eKE}$). The major vibronic transitions have been labeled in the figure. These correspond to vibrational levels of the ground state $X^3\Sigma_g^-$ (X) and the first electronically excited state $a^1\Delta_g$ (a) of neutral O_2. As is evident from the vibrational assignments, the onset of the a state partially overlaps with the higher lying vibrational levels of X state. The eBE values recorded for the X and a state transitions are in good agreement with reported values, including the data produced on the high resolution photoelectron imaging spectrometer at Australian National University (ANU data, white spectrum in Figure 3.10)[19, 20] as well as with previously published work.[95].

The angular anisotropy parameter may be extracted by integration over a range of radial values r for a given value θ as described in section 3.6. In order to verify the quality of our detector response for these measurements, the O_2^- data collected in this laboratory was compared to a similar set of O_2^- data collected on the high

resolution photoelectron imaging spectrometer at Australian National University. To avoid inconsistencies arising from PADs extracted from overlapping electronic bands, as well as poor signal-to-noise associated with the $0 \leftarrow 0$ vibronic channel of the X state, only the 1-4 vibrational final states of the X state were considered. The results are shown in Figure 3.12.

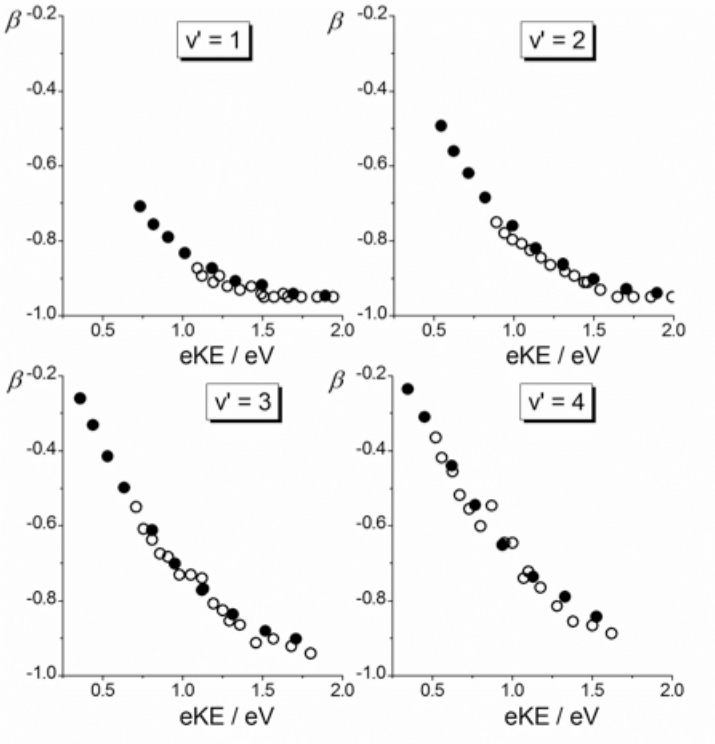

Figure 3.12: Comparison of extracted β(eKE) values from the 1-4 vibronic transitions associated with detachment *via* the (X) state as in (Equation 3.15a) over a wavelength range from 480-900 nm. Each data point represents measurement at a different wavelength. The white circles are data taken in this laboratory, while the dark circles come from data taken in the ANU laboratory. (Reproduced with permission from *The Journal of Chemical Physics*, Van Duzor *et al.*, Nov. 2010, Vol. 133 174311-174320 ©2010 *American Institute of Physics.*)

Measurements were taken at a number of detachment wavelengths over a range from 440 to 900 nm. These were compared with data from the ANU laboratory. Our

spectrometer faithfully reproduced the results recorded using the higher resolution instrument.

Chapter 4

Evidence of Intracluster Electron-Molecule Interactions: Photoelectron Angular Distributions of $I^- \cdot CH_3I$

Photoelectron angular distributions (PADs) can provide a sensitive probe of the orbital structure of atoms, molecules and clusters[96, 97]. Understanding of the relationship between the PAD, the eKE and the spectroscopic selection rules governing the detachment process can yield considerable insight into the parent electronic wave functions.[98] The electric dipole selection rules for photodetachment with plane-polarized light limit the available detachment channels to $\Delta\ell = \pm 1, \Delta m = 0$. For this reason, it is often claimed that the PAD represents "a signature of the parent orbital. Cluster anion photodetachment presents a particularly intriguing case.[99] Interactions between the departing electron and the neutral residue are similar to

Portions of this chapter have been reproduced with permission from *The Journal of Chemical Physics*, Van Duzor *et al.*, Nov. 2009, Vol. 131, 204306-204314. ©2009 *American Institute of Physics.*

those active in electron-molecule scattering. Thus, it may be reasonably expected that such interactions should be manifested in the cluster anion PADs.

In order to assess the applicability of such claims, rigorous studies of the eKE dependence of the cluster anion PAD must be performed. In this chapter, measurements of the angular distributions and photoelectron spectra associated with photodetachment from the $I^- \cdot CH_3I$ cluster anion are reported over a range of eKEs. In view of the eKE dependence of the angular distribution it is perhaps surprising that to date very few groups have coupled the power of anion detachment imaging with a readily tunable photon source to experimentally probe PAD evolution.[100, 101]

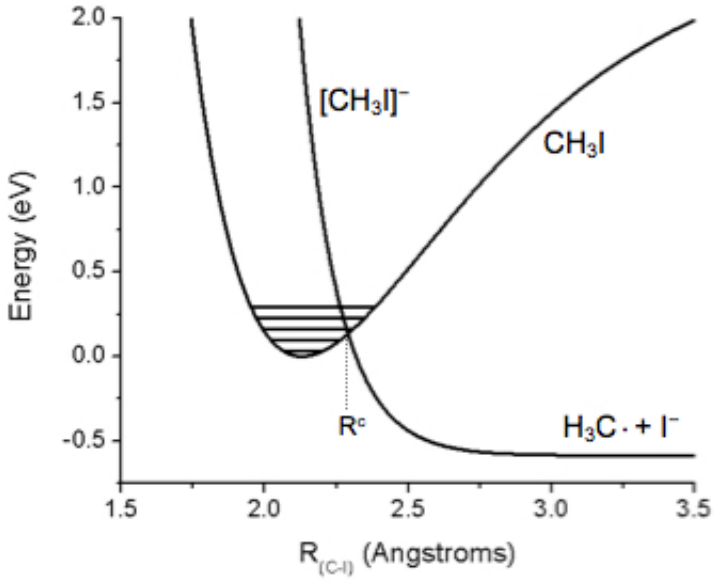

Figure 4.1: Relevant potential curves of the CH_3I molecule along the C-I coordinate. Capture of low energy electrons by CH_3I at C-I bond lengths $<$ than R^c prepares the transient anion $[CH_3I]^-$. If $[CH_3I]^-$ can evolve to a length $R > R^c$ prior to autodetachment, I^- is produced.

As illustrated in Figure 4.1, CH_3I displays a strongly dissociative anion state intersecting the neutral ground state just above the the $\nu_3 = 1$ vibrational level (predominantly the C-I stretching mode). The close proximity of these states at low energy makes CH_3I a very interesting system for the study of electron molecule scattering interactions. A number of electron scattering studies have shown evidence of electron-molecule resonances, vibrational excitation and dissociative electron attachment (DEA) in CH_3I.[8–10, 102, 103]

The $I^-{\cdot}CH_3I$ cluster anion is a fascinating species. It has been studied as a proposed S_N2 intermediate and does indeed produce I^- fragments under specific photoexcitation conditions.[3–5, 41, 104] At low eKEs, a transient anion species may arise due to capture of the electron into the σ^* orbital. Due to the close proximity of the dissociative state CH_3I^- to the ground state of neutral CH_3I at low energy, the CH_3I^- anion is more likely to evolve beyond the curve crossing point R^c on the timescale of autodetachment, as illustrated in Figure 4.1. This intracluster fragmentation process is analogous to the dissociative electron attachment (DEA) process observed in the interaction of low energy electrons with gaseous methyl iodide molecules and molecular clusters.[6, 9, 10, 32, 105, 106] These studies and a body of other existing work suggest that the structure of the cluster anion is that of an atomic anion moiety (I^-) physically bound to the CH_3I molecule, which suffers little distortion from its ground electronic state equilibrium geometry.[46, 107] In light of this structure it would be reasonable to assume that the PAD obtained through photodetachment from this cluster anion would be similar to that of free I^- detachment. This is certainly true in many other atomic iodide based cluster anions.[46, 108–111]. However, photodetachment measurements of $I^-{\cdot}CH_3I$ reveal a very significant deviation from this expectation.[46, 109]

Given the structure of the cluster anion and the surprising nature of the angular distribution [46], $I^-{\cdot}CH_3I$ represents an ideal system in which to examine the effect of the immediate environment on the detachment process. Herein, the results of $I^-{\cdot}CH_3I$ photodetachment imaging are compared with those of I^- detachment taken over a similar energy range. Within this energy range, the results presented strengthen the case for electron localization on the noncovalently bound I atom in the cluster. Also observed are fragmentation channels first reported by Johnson et al.[3] More importantly, one may gain a better understanding of the relationship between the PAD and the parent orbital, in particular the effect of the interactions of the departing electron with its surrounding environment. In doing so, some important caveats regarding the claim that the PAD represents the nature of the parent orbital can be established.

4.1 Experimental Details

Free I^- and $I^-{\cdot}CH_3I$ cluster anions are produced using the electron impact ionization method (section 3.2.2) and a pulsed supersonic expansion of Ar carrier gas seeded with the ambient vapor pressure of CH_3I. The prenozzle stagnation pressure is 80 psig and the base pressure in the vacuum chamber is $1{\times}10^{-6}$ torr, rising to $1{\times}10^{-5}$ torr during nozzle operation. The photon wavelength range in these experiments is 370-270 nm, achieved by frequency doubling (BBO crystal) the output from various dyes (coumarin 307, coumarin 153, pyrromethane 597, DCM, pyridine 1, and pyridine 2). Pulse energies range from 4-13 mJ. Under the mild focusing conditions of the experiment (1 m lens and pair of irises to collimate the beam) power densities of 4.2 - $13.5{\times}10^{10}$ W cm^{-2} result.

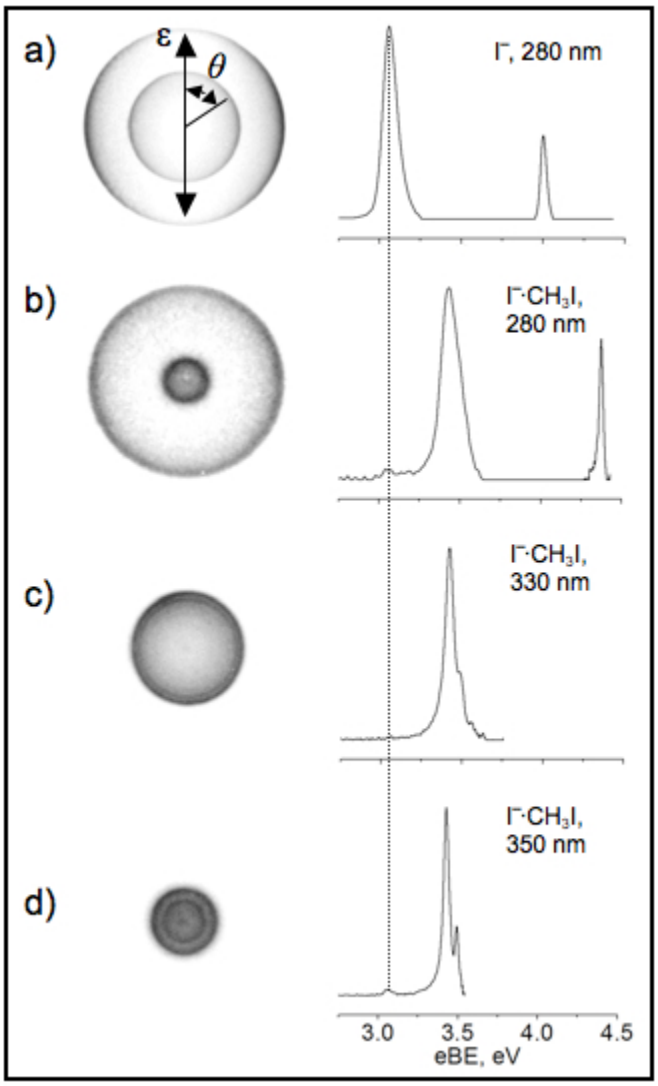

Figure 4.2: Photodetachment (images at left, spectra at right) from (a) I^- at 280 nm and [(b)-(d)] $I^-\cdot CH_3I$ at 280, 330 and 350 nm. The direction of the laser electric field polarization vector is indicated in (a). The shift in eBE due to solvation is evident in [(b)-(d)]. A minor peak at 3.06 eV eBE is seen in (b)and (d), corresponding to photodetachment of the DEA product I^-. (Reproduced with permission from *The Journal of Chemical Physics*, Van Duzor *et al.*, Nov. 2009, Vol. 131, 204306-204314. ©2009 *American Institute of Physics.*)

4.2 Data and Analysis

Photoelectron images were collected for I^- and $I^-\cdot CH_3I$ detachment over the wavelength range of 370-270 nm in 10 nm steps. A representative sample of these images is displayed in Figure 4.2. Encoded within the images are details of the eigenstates of the parent neutral species (through the photoelectron spectrum) along with the electronic eigenfunctions of the parent anion and the interactions of the departing electron with the neutral residue (through the PAD).

This work employed the algorithm of Hansen and Law[112] to perform the Abel inversion. Photoelectron spectra are calibrated against the well characterized $^2P_{3/2}$ transition of I^- detachment.[113–115].

4.2.1 Photoelectron Energy Distributions

The images shown in Figure 4.2 were recorded under identical velocity mapping conditions. Consequently, the radial size of the features in each image provides instant visual indication of the relative eKEs. The eKE is governed by energy conservation, eKE = hν - eBE. Alluded to briefly in Chapter 2, the case of photodetachment from I^- produces an open shell species in one of two relatively low lying electronic states. These are labeled $^2P_{3/2}$ and $^2P_{1/2}$ and correspond to the two spin-orbit states associated with the $5p^5$ atomic electron configuration of neutral iodine. The binding energy associated with the transition to the $^2P_{3/2}$ state is 3.06 eV. An additional 0.94 eV, the spin orbit splitting in neutral I, is required to access the $^2P_{1/2}$ state.[113] Since higher radius corresponds to higher eKE the outer feature in the 280 nm image and the single feature in the 330 and 350 nm images correspond to the $I^-(^1S_0) \rightarrow I(^2P_{3/2}) + e^-$ channel. The inner feature is only apparent at photon energies greater than the binding energy associated with the $I^-(^1S_0) \rightarrow (^2P_{1/2}) + e^-$ channel.

Comparison of the photoelectron spectra extracted from the 280 nm I^- and $I^-\cdot CH_3I$ shows striking similarities. The $I^-\cdot CH_3I$ spectrum displays the narrow features characteristic of atomic anion detachment and also shows the same separation (0.93±0.02 eV) observed in the I^- photodetachment spectrum. The most obvious difference between the spectra is the significant shift in the eKE of the peaks in the cluster anion spectrum. Since the energy is shifted to lower values there must be a

corresponding increase in eBE, or a stabilization of the anion. Our results show that the magnitude of this solvation induced shift is 0.37±0.02 eV, consistent with earlier work on this system.[3, 5, 104, 116] Due to the similarity of the spectra (notwithstanding the solvent shifts) the major bands in the $I^-{\cdot}CH_3I$ spectra will be referred to henceforth by their respective neutral iodine atom final state.

Closer inspection of the 350 nm $I^-{\cdot}CH_3I$ image [Figure 4.2(d)] reveals some closely spaced concentric features within the $^2P_{3/2}$ band. This structure (which is also discernible in the 330 nm image) is the result of vibrational excitation of the neutral residue upon photodetachment.[105, 116] In the images, these features appear as concentric rings nested within the outermost feature. The observed spacing between these features is consistent with the reported value of 1 quantum in the ν_3 mode. This value, 66 meV in free CH_3I [4, 116, 117] is measured at 69±3 meV in our spectra. Superficially, these features appear to be absent in the 280 nm $I^-{\cdot}CH_3I$ image. However, this is a facet of the energy resolution of the detector which decreases as a function of eKE. Comparison of the 280 nm photoelectron spectra reveals broadening of the $^2P_{3/2}$ transition for $I^-{\cdot}CH_3I$ relative to I^-, due to unresolved spectral features associated with the internal degrees of freedom of the cluster.

4.2.2 Fragmentation Channels

The $I^-{\cdot}CH_3I$ photodetachment images shown in Figure 4.3 all show the presence of a weak transition at an eBE of 3.06 eV. These measurements lie within a narrow energy window of one or other of the direct detachment thresholds. The 350 nm image represents a photon energy of 0.12 eV in excess of the $^2P_{3/2}$ channel onset, while 370 nm photons lie below the vertical detachment energy. Such features are not

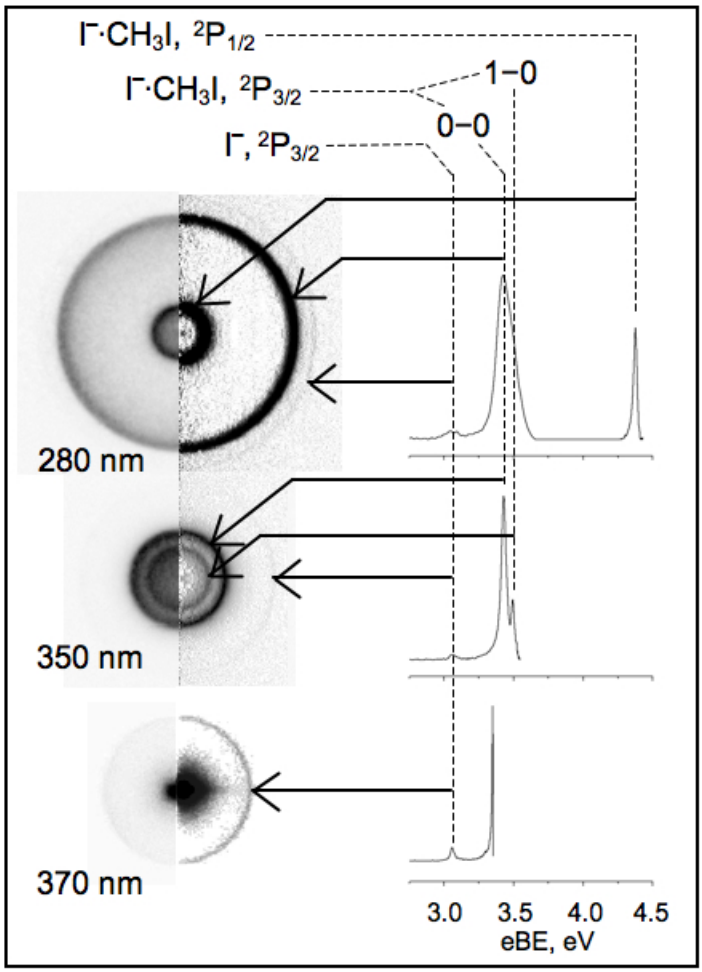

Figure 4.3: Photodetachment from I^-CH_3I at 280, 350 and 370 nm. Images are split, with the raw image at left and the Abel-inverted image at right. Spectra accompany at far-right. The Abel-inverted images are contrast-enhanced to reveal evidence of fragmentation. (Reproduced with permission from *The Journal of Chemical Physics*, Van Duzor *et al.*, Nov. 2009, Vol. 131, 204306-204314. ©2009 *American Institute of Physics.*)

observed for wavelengths shorter than 330 nm until the photon energy approaches the vicinity of the $^2P_{1/2}$ threshold. Similar behavior is, however, observed just above the $^2P_{1/2}$ direct detachment threshold in the 280 nm image in Figure 4.3. The eBE of this weak feature identifies it as being due to photodetachment from I^-.[118] The presence of this I^- detachment signature is ascribed to intracluster electron transfer followed by dissociation of the methyl iodide moiety. This will be discussed in greater detail below.

4.2.3 Photoelectron Angular Distributions

Perhaps the most striking result upon comparison of the images presented in Figure 4.1 is the differing photoelectron anisotropy in the I^- and $I^-{\cdot}CH_3I$ images. A difference in the PAD upon monosolvation of I^- with CH_3I was previously reported by Mabbs et al.[46] in a single measurement at 267 nm. However, it is well known that PADs are generally dependent on the eKE. The current measurements represent the first study of the evolution of the $I^-{\cdot}CH_3I$ PAD over a range of photodetachment energies from near-threshold to 1.2 eV, eKE. These measurements also provide a direct comparison with I^- PADs over the same eKE range.

To facilitate later discussion of the evolving PADs and to illustrate the significant differences between free I^- detachment and $I^-{\cdot}CH_3I$, the anisotropy parameter β is used. The significance of the anisotropy parameter has been discussed at length in chapter 2 and will be only briefly summarized here.

For single-photon detachment with a linearly polarized laser the PAD is described by $I(\theta) = \sigma/4\pi[1 + \beta P_2(\cos\theta)]$described in detail in section 2.2 (Equation 2.21). The anisotropy parameter, β, varies between 2 and -1 and characterizes the

Table 4.1: eKEs and anisotropy parameters (β) at selected detachment wavelengths for I^- and $I^-{\cdot}CH_3I$ via the $^2P_{3/2}$ photodetachment channel. (Reproduced with permission from *The Journal of Chemical Physics*, Van Duzor *et al.*, Nov. 2009, Vol. 131, 204306-204314. ©2009 *American Institute of Physics.*)

	I^-		$I^-{\cdot}CH_3I$	
λ, nm	eKE (eV)	β	eKE (eV)	β
350	0.49	-0.64 ± 0.06	0.12	-0.02 ± 0.06
340	0.59	-0.83 ± 0.05	0.22	0.09 ± 0.05
330	0.70	-0.92 ± 0.03	0.33	0.11 ± 0.03
320	0.82	-0.89 ± 0.04	0.45	0.13 ± 0.04
310	0.95	-0.85 ± 0.04	0.58	0.06 ± 0.04
300	1.08	-0.87 ± 0.02	0.71	-0.01 ± 0.07
290	1.22	-0.80 ± 0.05	0.85	-0.06 ± 0.05
280	1.37	-0.76 ± 0.03	1.00	-0.17 ± 0.08
270	1.45	-0.75 ± 0.03	1.17	-0.26 ± 0.11

PAD. The anisotropy parameters extracted from the $^2P_{3/2}$ channel feature in our I^- and $I^-{\cdot}CH_3I$ images are recorded in Table 4.1 and represented graphically in Figure 4.4. Attention is confined to this channel as it offers the widest range of data for comparison between the free and clustered I^- detachment experiments. The associated uncertainties of the values in Table 4.1 are standard deviations within a number of experiments and thus represent a measure of the repeatability of the measurements. Due to the fourfold symmetry of the results each image represents four individual measurements of the PAD. Using the Hansen and Law [112] algorithm a measurement of β can be made using each quadrant of the image. Additionally, at each wavelength a minimum of four images were collected. Each image comprises about 2000 laser shots. In cases of poorer signal to noise, two to four additional images were collected. The number of images recorded allows determination of the standard

deviation from the mean β value for a given wavelength.

The plot in Figure 4.4 clearly shows the contrast in the two sets of data. Near thresh-

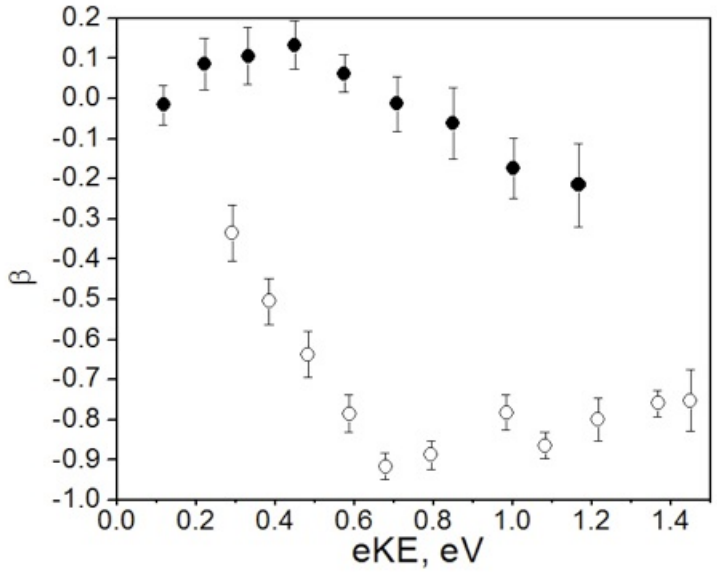

Figure 4.4: Experimentally determined anisotropy parameter (β) vs. eKE for photodetachment via the $^2P_{3/2}$ channel of I^- (open circles) and $I^-{\cdot}CH_3I$ (filled circles). (Reproduced with permission from *The Journal of Chemical Physics*, Van Duzor *et al.*, Nov. 2009, Vol. 131, 204306-204314. ©2009 *American Institute of Physics.*)

old, both I^- and $I^-{\cdot}CH_3I$ PADs are effectively isotropic, β values approach zero. While a variation in β with eKE is expected, the two trends diverge markedly. The I^- data follows the familiar pattern of direct, single photon photodetachment from an atomic p orbital, becoming steadily more negative until arriving at a minimum value around 0.7 to 0.9 eV. Thereafter, β shows a steady decrease in magnitude. This behavior is predicted by the Cooper-Zare treatment (discussed in chapter 2)[24, 25, 119, 120] and is in good agreement with previous measurements. However, for the $I^-{\cdot}CH_3I$ detachment there is an increase in β until approximately 0.45 eV and then a steady decrease.

4.3 Discussion: Intracluster Electron Interactions in $I^-\cdot CH_3I$

The differences in the $I^-\cdot CH_3I$ PAD compared to that of I^- are striking. This is even more remarkable upon comparison with the PADs observed in photodetachment of other atomic iodide anion centered clusters with strongly polar solvent molecules. Examples include $I^-\cdot H_2O$, $I^-\cdot CH_3CN$[46, 111], $I^-\cdot C_4H_5N$ ($I^-\cdot$pyrrole)[110], aniline[108], and $I^-\cdot CH_3Cl$(presented in chapter 5)[109, 121], which are very similar at eKE < 0.90 eV to that of I^- recorded in this work and by other researchers.[46, 122, 123]

To gain at least a qualitative physical insight into the reasons for these discrepancies it is helpful to consider the detachment process in two stages. First the electron is detached from the noncovalently bound, atomic iodide moiety. Subsequently the departing electron interacts with the neutral solvent molecule as it leaves the cluster. To justify this approach, an argument must first be made for electron localization on the noncovalently bound iodine atom within the cluster by setting these current results in the context of previous work. Finally, the nature of the electron-neutral interactions in the photodetachment channel is discussed.

4.3.1 Electron Localization Within $I^-\cdot CH_3I$

In cluster anions of type $X^-\cdot M_n$ where X represents a halogen atomic anion and M "solvent" molecule, the excess charge is typically found to remain strongly localized upon the halogen atom.[46, 108, 124] Direct detachment from such clusters reveals photoelectron spectra displaying narrow features strongly reminiscent of atomic anion detachment (although subject to broadening associated with excitation of the internal

degrees of freedom of the cluster). The most obvious difference is the increased eBE due to the stabilizing solvent effect of the neutral molecule. Similarly the PADs are usually affected to only a minor extent, even in the case of highly polar solvent molecules.[125]

In the case of $I^-{\cdot}CH_3I$, although the spin-orbit splitting of iodine and the narrow, atomic like detachment features are retained, vibrational structure is observed. This is due predominantly to excitation of the ν_3 mode corresponding to motion predominantly along the covalently bound CI coordinate[41, 104, 116] as evinced by the peak separations measured at low eKE. Delocalization of the excess electron orbital across the cluster would be expected to cause significant distortion of the CH_3I moiety. However, ab initio calculations and Franck-Condon treatments of the photoelectron spectrum have shown that CH_3I distortion is minor. Experiment and theory seem to confirm that there is only a slight (1.5%) elongation of the CI bond in the cluster anion.[41, 107] In the case of $I^-{\cdot}CH_3I$ detachment a major contribution to the vibrational structure, particularly near the threshold of the detachment channels is a nonadiabatic coupling of the photoelectron and the CI coordinate *via* a temporary negative ion state, a vibrationally inelastic scattering event.[41] Ab initio calculations were performed using the same basis sets and methods as Truhlar, et al.[107] which show a Mulliken charge of 0.94 a.u. on the noncovalently bound iodine atom and determine the localization of the excess electron (as shown in Figure 4.5), further justifying the discussion of the angular distributions in terms of detachment from an initial iodide moiety.

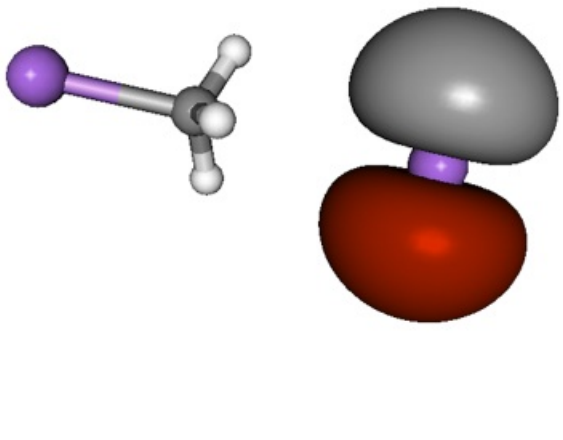

Figure 4.5: The calculated HOMO of $I^- \cdot CH_3I$ (MP2 level, basis sets and exponents ref. 23) evinces localization of the excess electron on the atomic I.

4.3.2 Intracluster Fragmentation Channels

Before turning attention to the $I^- \cdot CH_3I$ angular distributions, brief comment should be made regarding the 3.06 eV binding energy feature observed in several of the images. This weak feature appears within two narrow photodetachment wavelength windows. The first of these windows lies at 370-330 nm, while the second is accessed only in our 280 nm measurement. These correspond to photon energies in the region of the thresholds for the $^2P_{3/2}$ and $^2P_{1/2}$ channels, respectively. The detachment wavelength specificity of this feature rules out fragmentation of the cluster during its time of flight through the mass spectrometer as a source of free iodide. Instead an intracluster electron transfer process followed by fragmentation of the CH_3I molecule occurs. This process was first reported in the $I^- \cdot CH_3I$ cluster anion in Reference [20]

and explained in similar terms to the DEA observed in low energy electron collisions with CH_3I.[8, 10, 32, 106, 126, 127]

In brief, the diabatic potential curve along the C-I coordinate for the dissociative CH_3I^- state crosses the diabatic potential associated with the ground electronic state of the neutral CH_3I molecule near its equilibrium geometry(see Figure 4.1). The intracluster fragmentation process is consistent with a mechanism whereby a virtual dipole bound state or a vibrational Feshbach resonance pre-dissociates on a timescale faster than that of vibrational autodetachment. This feature is apparent in our images as the result of a sequential, two-photon absorption process. The first absorption results in the excitation of the temporarily bound anion state and the fragmentation process occurs on a timescale that is extremely rapid compared with the length of our laser pulse (25 fs cf. 4 ns).[41] In support of this assignment, it is noted that reducing the laser intensity by half results in a twofold decrease in the integrated intensity of the direct transition and an approximately fourfold decrease in the integrated intensity of the transition associated with the fragmentation product.

4.3.3 Photoelectron Angular Distributions

In view of the strong localization of the electron on the I atom, it is reasonable to view the initial detachment as atomic anion-like. PADs are frequently quoted as representing signatures of the parent anion detachment orbital.[98, 99] This appealing statement promises that photodetachment imaging studies provide a window of insight into the nature of anion detachment orbitals. For example, the I^- images display PADs that can be very satisfactorily explained in terms of detachment from an atomic p-orbital.[98] The angular distribution observed in this case is the result

of interference between the s and d partial angular momentum waves contributing to the free electron wave function. The variation in the β parameter characteristic of the PAD (Figure 4.4) is explained by the changing cross sections for these partial waves as the eKE increases, in accordance (to a reasonable approximation) with Wigner threshold law.[128]

The observed I^- behavior is in accordance with the Cooper-Zare model which predicts the anisotropy parameter based upon the partial wave radial matrix elements and relative phase shifts.[24, 25, 119, 120] A further simplification of the Cooper-Zare expression for β allows for the variation in the anisotropy parameter to be expressed in terms of the relative phase shift of the partial waves and the ratio of their radial matrix elements, which scales approximately as eKE.[29] For detachment from an atomic p-orbital the simplified expression, as explained in more complete detail in section 2.2.2, takes the form

$$\beta(\mathrm{eKE}) = \frac{2\mathrm{A}^2 \cdot \mathrm{eKE}^2 - 4\mathrm{A}^2 \cdot \mathrm{eKE}^2 \cdot \cos\delta_{d-s}}{1 + 2\mathrm{A}^2 \cdot \mathrm{eKE}^2} \tag{4.1}$$

Equation 4.1 is simply Equation 2.42 rewritten for the p-orbital case $\ell = 1$. This form of the function allows for a simple fit of the data as a function of eKE. The proportionality constant, A and the relative phase shift, δ_{d-s} are parameters of the fit. Equation 4.1 may be fit to the experimental β(eKE) data using the Levenberg-Marquardt [129] nonlinear least-squares algorithm fitting procedure. In the case of I^-, this returns values for A of 0.54 eV and $\cos\delta_{d-s}$ 0.90, which are in good agreement with previous work [46] on the I^- photodetachment angular distributions obtained using far fewer data points and very satisfactorily reproduces the experimental data. Such energy independent A factors and relative phase shifts are sufficient to describe the general trends in β(eKE) and therefore the PAD over energy ranges within a few

eV of threshold for many different atomic anion-like systems. The use of an energy independent A parameter was justified in section 2.2.2 according to the arguments of Hanstorp et al.[29]. Here the implications of the use of a fixed δ_{d-s} are briefly examined.

For atomic anions, the relative phase shift is determined primarily by the details of the detachment event. However, as the size of the atom increases it is reasonable to ask what role polarization effects will play. In particular, the different partial waves will experience different interaction with the potential of the neutral residue. To assess the likely variation in the relative phase over the energy range pertinent to these experiments the simplification that the polarization term is most significant is applied. In doing so, the effect of the quadrupole term is ignored. At the level of insight required in this discussion, it is assumed to be negligibly small due to the magnitude of the quadrupole polarizability.[130]

Concentrating solely on the contribution of the r^{-4} polarization term in the potential the s and d phase shifts can be approximated using the modified effective range theory (MERT) expressions [131–133]

$$k \cdot \cot \eta_s = \frac{1}{A_0} + \frac{\pi\alpha}{3A_0^2}k + \frac{2\alpha}{3A_0^2}k^2 \ln\left(\frac{\alpha k^2}{16}\right) \tag{4.2}$$

and

$$\tan \eta_d = \frac{\pi\alpha k^2}{(2\ell+3)(2\ell+1)(2\ell-1)} \tag{4.3}$$

ignoring higher order terms in k. Using η_ℓ to denote the energy dependent phase shift associated with the ℓ^{th} partial wave, a distinction with the energy independent δ_ℓ can be made. k is the linear momentum of the electron, α is the dipole polarizability, and A_0 is the scattering length. A dipole polarizability of 5.35×10^{-24} cm^3[134] is

used and, in the absence of a value for the scattering length of I, an approximation is made using that of Xe, -6.2 a.u.[131] The eKE dependent relative phase shift δ_{d-s} behavior is illustrated by the dashed line in Figure 4.6(a). Recalculation of β(eKE) via substitution of $\delta_{d-s} = \eta_{d-s}$(eKE) into Equation 4.2, the dotted line in Figure 4.6(a) yields close agreement with the curve obtained at fixed δ_{d-s} [solid line, Figure 4.5(a)]. It is noted that over the majority of the energy range the MERT calculations yield a $\cos\delta_{d-s}$ value of approximately 0.98. Given the truncation of the MERT expressions, the approximate nature of the scattering length and that this treatment ignores short range details of the detachment process, the 10% difference in the cosines of δ_{d-s} and η_{d-s} can be considered reasonable agreement. More pertinently, the value of η_{d-s} is relatively constant over the energy range considered. Additionally, this approach completely ignores short range effects.

The above shows why the use of a constant relative phase shift can yield reasonable agreement between experimentally determined and Cooper-Zare predicted β values for I^-, and indeed several other atomic and atom based cluster anion systems. However, a relatively minor change in η_{d-s} with eKE is not likely to be a general phenomenon, particularly where background scattering or resonances are encountered. In these cases the recorded PAD is likely to be severely affected. The $I^-{\cdot}CH_3I$ anisotropy parameters recorded in this work serve to illustrate this point.

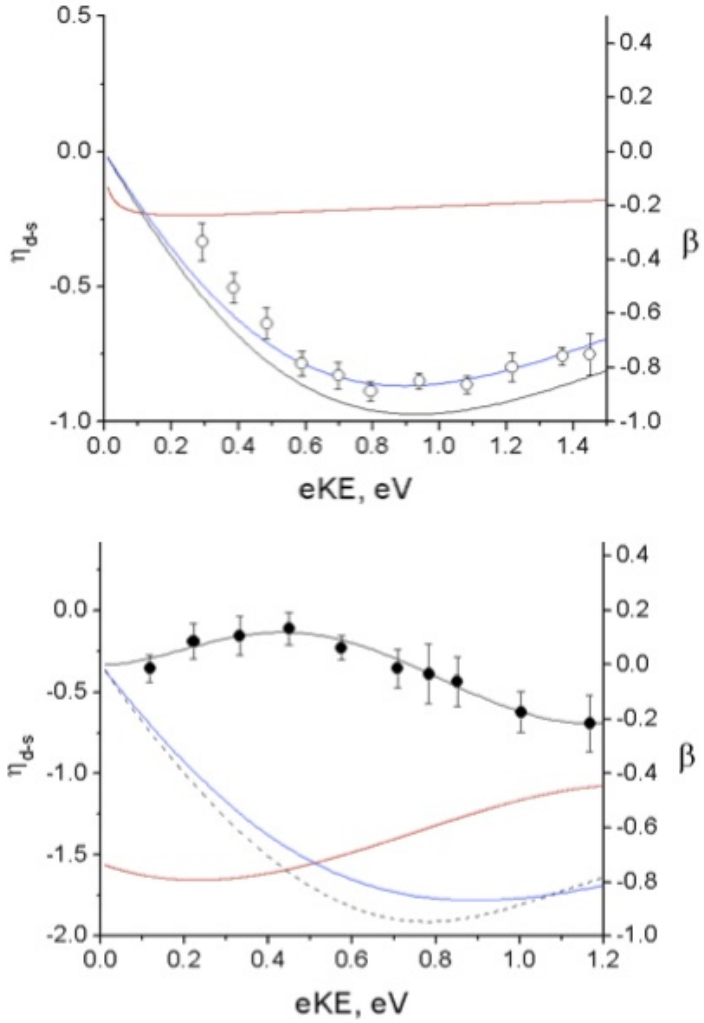

Figure 4.6: (a) The effect of η_{d-s} on the I^- PAD. Open circles are experimental I^- β values. The blue line is Equation 4.1 with $\delta_{d-s} = 0.45$ radians. The red line is the MERT η_{d-s}(eKE) and the black line is Equation 4.1 with η_{d-s}(eKE) substituted for δ_{d-s}. (b) Closed circles represent experimental $I^- \cdot CH_3I$ β values. The solid black line is a fit of Equation (2) to these using η_{d-s}(eKE) as the fitting parameter in place of δ_{d-s}. The red line shows η_{d-s}(eKE) and the dashed black line is β(eKE) from Equation 4.1 substituting η_{d-s}(eKE)+ $\pi/2$ for δ_{d-s}. The blue solid line is reproduced from part (a) above. (Reproduced with permission from *The Journal of Chemical Physics*, Van Duzor *et al.*, Nov. 2009, Vol. 131, 204306-204314. ©2009 *American Institute of Physics.*)

The differences between the angular distribution associated with $I^-\cdot CH_3I$ and those of almost every other I^- based cluster anion reported in the literature to date [46, 108] are dramatic. To explain this phenomenon a simplistic approach is taken. It must be stressed that this is not designed to give quantitatively accurate phase shifts but is significantly insightful regarding the nature of the detachment process within this cluster. The detachment process is treated as being from an I^- anion, subsequent to which the electron encounters the field of the cluster. Thus it is approximated that the relative partial wave cross sections have the same ratio as expected for I^- detachment. In this case one would expect the differences in the angular distribution to be determined by the changing relative phase shift as the electron departs the cluster. Retaining the assumption that A (Equation 4.2) is independent of eKE the variation in the relative phase shift over the energy range of the experiment using equation (2) can be extracted. This variation is shown in Figure 4.6(b) (dotted line) and was obtained by representing η_{d-s} with a second order polynomial in eKE and performing a nonlinear least-squares fit to the data. Again it must be stressed that this procedure is not designed to be quantitatively accurate (it is tacitly assumed that the central potential model gives a reasonable enough description of the long range interactions and any effects of inelastic scattering events are neglected). However, it is of considerable interest to note that addition of a constant $\pi/\ 2$ to our extracted η_{d-s} brings β(eKE) close to the curve obtained in the I^- detachment experiment, as shown by the dash-dotted line in Figure 4.6(b).

Observation of a shift of the order of $\pi/\ 2$ is significant. It has previously been suggested that a resonance phenomenon might be responsible for the anomalously isotropic PADs from $I^-\cdot CH_3I$ detachment.[46] The phase shift associated with a single ℓ wave resonance reaches a maximum of $\pi/2$ at the resonance energy. A possible

candidate is a shape resonance associated with the CH_3I σ^* orbital.[127, 135, 136] ISEELS (inner shell electron energy spectroscopy) studies have suggested that the energy of this resonance in free CH_3I molecules will have a lower limit of 0.7 eV with the actual value more likely to lie closer to 2 eV.[136] The presence of a small peak in measurements of the total scattering cross section at 1.8 eV has been presented as experimental evidence of this feature.[127] However, for a resonance of this nature to account for the constant $\pi/2$ contribution to our relative phase shift it would have to be very broad. Furthermore, a shape resonance requires temporary capture of the electron, which is facilitated by the centrifugal part of the potential. Thus, this resonance must be associated with $\ell > 0$ and therefore correspond to a d-wave resonance. The relative phase shift can be written in terms of its s and d wave components as follows:

$$\eta_{d-s} = \eta_d - \eta_s = (\eta_{d,res} + \eta_{d,bkg}) - (\eta_{s,res} + \eta_{s,bkg}) \tag{4.4}$$

where $\eta_{\ell,res}$ is the resonance contribution to the phase shift, which should be small except in the vicinity of the resonance itself, and $\eta_{\ell,bkg}$ being the background phase shift. In the case of a d-wave resonance we would expect that subtraction of $\pi/2$ from our extracted η_{d-s} would recreate the I^- angular distribution. This is somewhat contrary to the change in the relative phase shift that is observed. From these considerations one may conclude that the drastic change in the angular distributions observed may be not entirely due to the σ^* shape resonance.

Alternatively, the factor $\pi/2$ may indicate the presence of a zero energy s-wave "bound state" or more correctly a zero energy resonance. To put this into context, the total electron energy-loss cross section for CH_3I in the low energy region is known to be large (4000×10^{-20} m^2 at 0.01 eV)[8] with only a small fraction being accounted

for by the DEA channels. In accordance with Levinson's theorem, the phase shift at zero energy is given by

$$\eta_s(0) = (n_0 + N/2)\pi \tag{4.5}$$

where n_0 represents the number of s wave bound states and N=1. This means that the s wave phase shift will have a value of $\pi/2$ (modulo π) at zero energy and, provided n_0 is even, may account for the approximate shift of $\pi/2$ in the relative phase of the s and d waves.

The role of some form of electron-molecule resonance is intriguing. However, the approach above must be treated with considerable caution. If a zero energy resonance is involved it must be sufficiently broad to account for the very slow change in relative phase shift over the eKE range of our measurements. It should also be considered that vibrational autodetachment from the temporary anion state associated with the vibrational Feshbach resonance may play a significant role in the observed behavior. Again, the width of the angular distribution variation is hard to explain by invoking the Feshbach resonance as it should be relatively narrow. There is also the σ^* shape resonance discussed above, which is presumably associated with the d-wave. Although the peak of this resonance presumably lies higher in energy than the 0-1.2 eV of these experiments, the sensitivity of the asymmetry parameter may allow that its effects begin to be felt toward the higher end of this eKE region.

It should also be pointed out that strictly the Cooper-Zare approach only applies in the case of a central potential. The success of this approach in predicting the β(eKE) trends for a large number of cluster anions allows us to use it to gain insight into the nature of the intracluster electron interactions. However, while approximating the detachment process as one of detachment from an atomic anion clearly gives

good results in a large number of cases caution must be applied. Transfer of angular momentum with the CH_3I molecule or even sufficiently strong interaction with the methyl iodide leading to a breakdown of the approximation that ℓ is a good quantum number would significantly alter the partial wave contributions. Rigorous calculations are required to resolve the effects of the scattering processes on the angular distributions in $I^-{\cdot}CH_3$ I photodetachment. However, the present measurements provide a data set upon which to test the accuracy of such calculations. Furthermore, the approach outlined above provides a physical picture which forms a starting point for such calculations and offers significant clues as to the nature of the detachment process.

4.3.4 Summary

Photoelectron imaging studies of $I^-{\cdot}CH_3I$ conducted over a range of detachment wavelengths from 370 to 270 nm show a marked and sustained difference in the evolution of the PAD to that of I^- detachment experiments over the same range. While the $I^-{\cdot}CH_3I$ cluster anion has the usual atomic anion-neutral solvent molecule structure the PADs do not conform to the usual modified Cooper-Zare behavior observed in other monosolvated halide anions. Treatment of the scattering interaction using a modified Cooper-Zare approach and an energy dependent relative phase shift (between the s and d partial waves expected in the detachment of an electron from an atomic p orbital) reveals that this is close to $\pi/2$. This argues in favor of an electron-molecule scattering resonance associated with the neutral cluster residue. However, by analogy with free-electron, neutral CH_3I experiments there are several phenomena which might play a role in such a process, in addition to the likelihood of a large background scattering contribution. A rigorous theoretical approach is

required to further determine the contribution of phenomena such as vibrational Feshbach and zero energy s-wave resonances in the detachment process, however, these experiments appear to validate viewing the photodetachment from this cluster anion through the lens of an electron scattering event. The following chapter develops this theme through a comparative study of the clusters $I^-{\cdot}CH_3Cl$ and $I^-{\cdot}CH_3Br$.

Chapter 5

$I^-\cdot CH_3X$ (X=Cl,Br,I): A Comparative Study of Photodetachment and Electron-Neutral Interactions

5.1 Introduction

Scattering experiments have long been used to probe electron-molecule interactions. In particular, they allow the study of resonances and virtual electronic states,[31, 137–139] which have a profound influence on electron capture and DEA. Photoexcitation experiments have demonstrated the existence of DEA [3–5, 104, 109, 121] and non-adiabatic vibrational excitation [3–5, 46, 104, 109, 116, 121] in atomic halide-methyl halide cluster anions. Application of the velocity mapped imaging

Portions of this chapter have been reproduced with permission from *The Journal of Chemical Physics*, Van Duzor *et al.*, Nov. 2010, Vol. 133, 144303-144312. ©2010 *American Institute of Physics.*

(VMI) technique [11] to cluster anion excitation has shown, as in the previous chapter, the strong sensitivity of the $I^-\cdot CH_3I$ PAD to the resonances encountered in electron-molecule scattering experiments.[46, 109, 121] As was demonstrated in chapter 4, the VMI technique, in conjunction with a tunable photon source, facilitates determination of the electron kinetic energy (eKE) evolution of the PAD. With prior knowledge of the PAD and photoelectron spectra of the core anion, this introduces the prospect of using atomic halide based cluster anions as probes of scattering phenomena. The anionic moiety might be made to act as an electron source (via photodetachment) in close proximity to a target molecule.

The present chapter expands upon the comparative analysis of I^- and $I^-\cdot CH_3I$ photodetachment presented in chapter 4, presenting the results of photodetachment imaging over the wavelength range 350-270 nm for $I^-\cdot CH_3X$ (X = Cl, Br, I) cluster anions. These halo-methanes comprise an ideal family of compounds with which to compare free electron-free molecule interactions with the results of cluster anion excitation. We are able to draw on an extensive body of experimental data (gathered through electron swarm, electron transmission, laser photoelectron attachment and Rydberg atom electron transfer techniques)[8, 10, 32, 102, 103, 106, 127, 135, 136, 140–168] and several theoretical and computational treatments of these processes, the potentials, and the resonances involved [6, 9, 10, 76, 102, 105, 106, 135, 145, 152, 153, 164, 168–175] to compare and contrast with the cluster anion photoexcitation results. It has already been made clear that the cluster anion PAD can reveal details of the interaction of the outgoing electron with the cluster substituents. This chapter will examine, by comparison of the three $I^-\cdot CH_3X$ systems, the effect of specific cluster substituents upon the PAD. Additionally, strongly energy dependent changes in the vibrational structure of the photoelectron spectra are observed. However, although

many similarities are found between cluster anion photoexcitation and free CH_3X-electron interactions, these results also identify processes unique to the cluster anion environment.

5.2 Experimental Details

A detailed description of the instrumentation can be found in chapter 3. Only specific details pertinent to the data presented in this chapter will be discussed here. Anionic species of interest were generated using the electron impact ionization technique. The gas mixtures were prepared by seeding Ar with the methyl halide of interest at a concentration of $\sim 5\%$, and flowing that mixture over liquid CH_3I at a base pressure of 40 psig, with the exception of the $I^-{\cdot}CH_3I$ cluster, which was again prepared as described in chapter 4.

Images were accumulated over the course of 1000 to 2000 laser shots. Several images are recorded for each anion (I^-, $I^-{\cdot}CH_3X$, X = I, Br, Cl) at individual wavelengths between 350 and 270 nm. At the shorter wavelengths, laser dependent background photoelectrons become significant. These are accounted for by subtraction of background images obtained by imparting a 5 μs delay between the anion and photon arrival times, and collecting for an equivalent number of experimental cycles.

5.3 Results and Analysis

$I^-{\cdot}CH_3X$ (X = I, Br, Cl) cluster anion photodetachment images were recorded at wavelengths between 350-270 nm, along with images of bare I^- detachment over

the wavelength range 370-280 nm to serve as a reference data set. Measurements were taken at regular intervals (5-10 nm), excepting those regions in which marked variation in the PAD occurs over a small eKE range. Specifically, smaller steps were taken near the opening of the photodetachment channel associated with the $^2P_{1/2}$ excited state of the iodine core. In such cases, smaller ($\leq$ 1 nm) intervals were employed to more completely recover the rapid evolution of the PAD with eKE.

5.3.1 Cluster Anion Electronic Transitions

Figure 5.1 displays photoelectron spectra (at 280 nm, $E_{h\nu}$ = 4.43 eV) representative of those extracted from the experimental images. The spectra are plotted as a function of electron binding energy, with the kinetic energy of each transition maximum written alongside. It is apparent that the eBE of the cluster anions is shifted compared to that of the bare I^- anion (3.06 eV).

This is due to stabilization of the I^- moiety through interaction (solvation) with the methyl halide. The degree of solvation is remarkably similar within the $I^-\cdot CH_3X$ series, 0.37 $\pm$ 0.01 eV, 0.36 $\pm$ 0.01 eV, and 0.35 $\pm$ 0.01 eV for X = I, Br, Cl respectively. Presumably the increase in ion-dipole interaction from X = I to Cl is offset by the decreasing polarizability, or changing ion-quadrupole interaction.

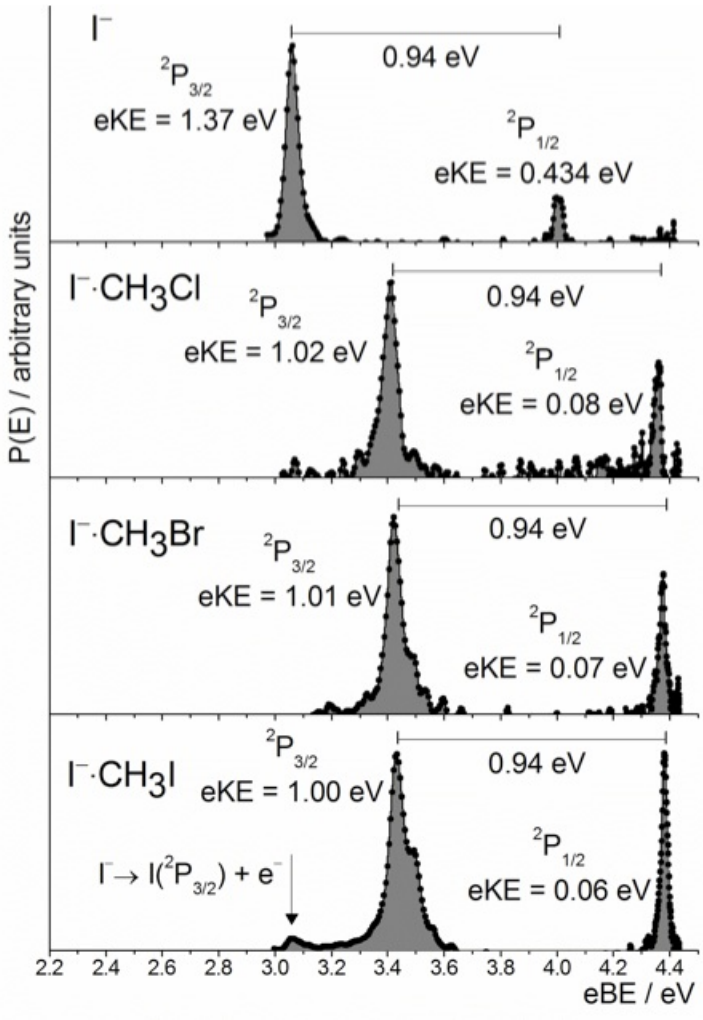

Figure 5.1: Photoelectron spectra (as a function of eBE) for I^-, $I^-{\cdot}CH_3Cl$, $I^-{\cdot}CH_3Br$, and $I^-{\cdot}CH_3I$ at a detachment wavelength of 280 nm. The downward arrow in the $I^-{\cdot}CH_3I$ spectrum indicates a contribution from I^-, produced by dissociation. (Reproduced with permission from *The Journal of Chemical Physics*, Van Duzor *et al.*, Nov. 2010, Vol. 133, 144303-144312. ©2010 *American Institute of Physics.*)

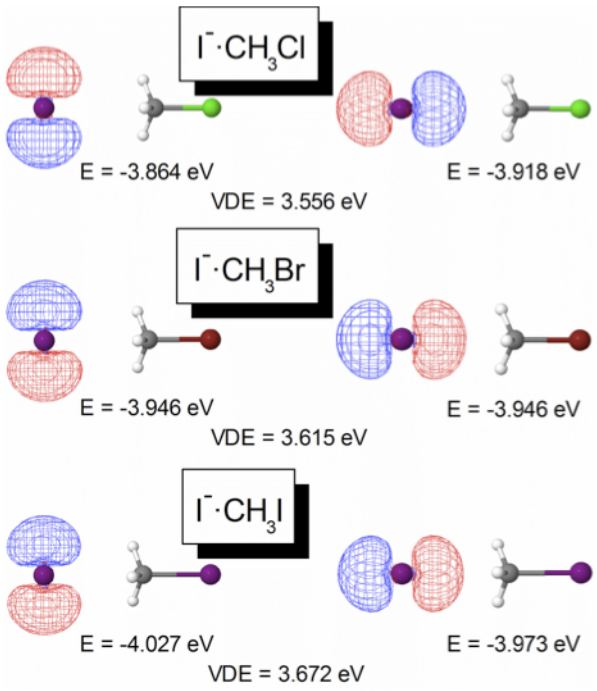

Figure 5.2: Isosurface representations of the two highest occupied orbitals (HOMO and HOMO-1) of each $I^-{\cdot}CH_3X$ cluster anion, orbital energies and vertical detachment energies. The HOMO switches from the $p_{x,y}$ ($I^-{\cdot}CH_3Cl$) to the p_z orbital ($I^-{\cdot}CH_3I$) across the series. (Reproduced with permission from *The Journal of Chemical Physics*, Van Duzor *et al.*, Nov. 2010, Vol. 133, 144303-144312. ©2010 *American Institute of Physics*.)

The presence of the CH_3X molecule clearly alters the energy of the I^- anion ground state. However it is significant (in cases of sufficient photon energy) that each of the cluster anions studied still displays two major photodetachment channels, split by approximately 0.94 eV. At the resolution achievable at this eKE, these values are identical to the separation of the two low lying spin-orbit states of atomic iodine. Although slight deviations (∼1-3 meV) from this splitting can be expected to arise due to the perturbation of the open shell iodine by the polar solvent molecule (as discussed in chapter 6 and reference[176]), this observation may reasonably be used to justify a view of the detachment process as that of an atomic anion taking place in the vicinity of a relatively unperturbed neutral molecule. As discussed in chapter 4, such

atomic-like detachment is a widely noted feature of $I^-\cdot X$ clusters.[3–5, 46, 104, 108–111, 116, 121, 177, 178] For convenience, the two detachment channels are again labeled after the ground and first excited states of the neutral I atom, $^2P_{3/2}$ and $^2P_{1/2}$ respectively. This notation presents a useful device with which to discuss and interpret the photodetachment dynamics of the $I^-\cdot CH_3X$ cluster anions.

Table 5.1: *Ab initio* bond lengths and angles for $I^-\cdot CH_3X$ (X=Cl,Br,I) and CH_3X (see text for details). Experimentally determined values for CH_3X are given in parentheses (References [183] and [184]). (Reproduced with permission from *The Journal of Chemical Physics*, Van Duzor *et al.*, Nov. 2010, Vol. 133, 144303-144312. ©2010 *American Institute of Physics*.)

	$I^-\cdot CH_3X$			CH_3X		
	X=			X=		
	Cl	Br	I	Cl	Br	I
$r_{C\text{-}X}$/Å	1.826	1.975	2.182	1.795	1.944	2.149
				(1.780)	(1.936)	(2.139)
$r_{C\text{-}H}$/Å	1.092	1.092	1.092	1.095	1.095	1.095
				(1.097)	(1.090)	(1.092)
∠HCX	110.6	111.0	111.3	110.7	111.0	111.1
				(111.5)	(111.7)	(112.12)
∠HCH	108.3	107.9	107.7	108.3	107.9	107.7
				(107.4)	(107.1)	(106.7)

The close proximity of the I^- anion, in particular the excess charge, does have some influence on the geometry of the CH_3X molecule within the cluster. *Ab initio* MP2 calculations, performed via QCHEM [179] using the aug-cc-pVDZ (H, C, Cl and Br)[180, 181] and aug-cc-pVDZ-p plus supplementary diffuse functions (I)[182] basis sets, reveal a slight distortion of the methyl halide bonds. Most notably the

C-X bond lengths are calculated to be longer in the cluster anion than for a neutral iodine-methyl halide pair. The distortions are shown in table 5.1, along with experimentally determined values for the free molecules.[183, 184] The values for $I^-{\cdot}CH_3I$ are consistent with those reported in chapter 4, as well as previously published calculations.[107] The C-X bond in $I^-{\cdot}CH_3I$ is elongated by 1.5%, while the corresponding bonds in the $I^-{\cdot}CH_3Br$ and $I^-{\cdot}CH_3Cl$ are elongated by 1.6 and 1.7%, respectively. Crucially however, as shown in Figure 5.2, the highest occupied orbitals are once again essentially iodine atomic p orbitals.

The calculations predict a VDE (vertical detachment energy, chapter 2) trend similar to that observed in the experiments across the series X = Cl, Br, I. The iodine 5p orbitals are now distinguished by their orientation relative to the molecular moiety. The relative energies of the p_z and $p_{x,y}$ orbitals differ due to the orientation of the dipole moment of the methyl halide, which lies along the cluster anion C_3 axis. Although the effect is not distinguishable in the photoelectron spectra, it is interesting to note that the highest occupied molecular orbital switches from $p_{x,y}$ in $I^-{\cdot}CH_3Cl$ to p_z orbital in $I^-{\cdot}CH_3I$ as the dipole moment varies across the methyl halide series.

5.3.2 Cluster Anion Vibrational Structure

Although there are strong similarities between the cluster anion and atomic I^- detachment, the presence of the molecular moiety is evident in the photoelectron spectra. The shift in binding energy has already been mentioned. Figures 5.3 and 5.4 present images and spectra recorded in the vicinity of the $^2P_{3/2}$ channel thresholds of the three cluster anions. Vibrational structure is apparent in the concentric rings visible in the images. These are particularly obvious at 350 nm (Figure 5.3) but

can also be distinguished in the 340 nm images and spectra presented in Figure 5.4. These features correspond predominantly to excitation of the C-X stretching modes (equivalent to the ν_3 mode in the free methyl halides).

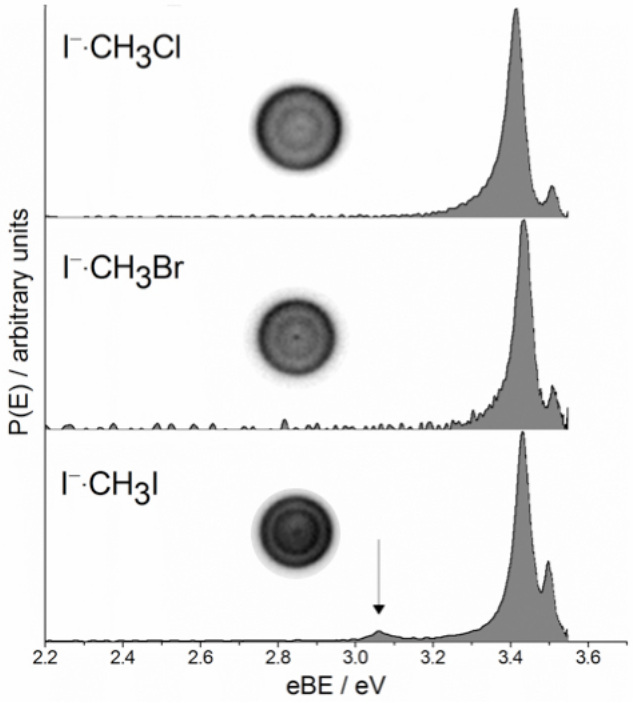

Figure 5.3: 350 nm detachment images and spectra (as a function of eBE) of the $I^- \cdot CH_3X$ cluster anions. The downward arrow indicates the presence of an I^- product fragment. (Reproduced with permission from *The Journal of Chemical Physics*, Van Duzor *et al.*, Nov. 2010, Vol. 133, 144303-144312. ©2010 *American Institute of Physics*.)

Within the Condon approximation a certain amount of vibrational excitation is expected in these species due to the minor distortions of the methyl halide moiety. Such distortion shifts the Franck-Condon envelope of the vertical transition, as the daughter neutral species is prepared at the equilibrium geometry of the parent anion. Vibrational transition intensities can be predicted as the square of the overlap integral (the Franck-Condon Factor, FCF) of the anion and neutral wave functions. Assessment of the vibrational excitation caused by photodetachment of the cluster anions has been performed via normal mode analysis using *ab initio* calculations.

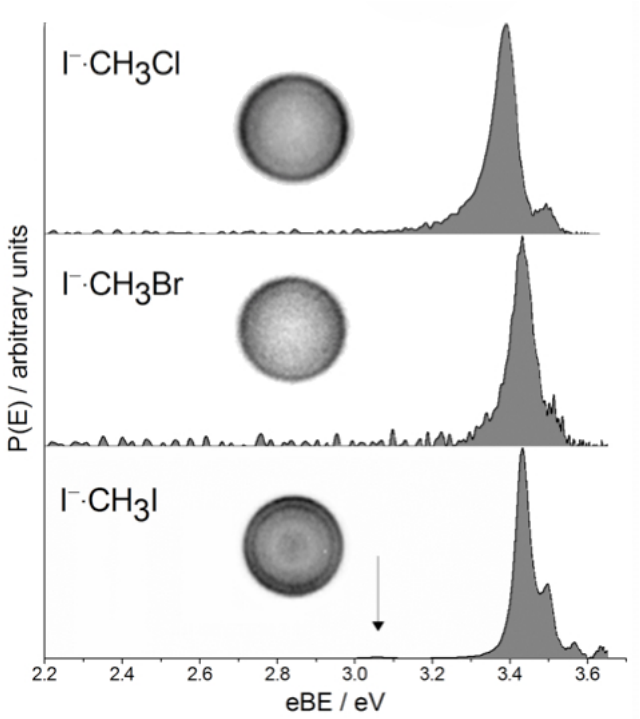

Figure 5.4: 340 nm detachment images and spectra (as a function of eBE) of the $I^-{\cdot}CH_3X$ cluster anions. The downward arrow indicates the presence of an I^- product fragment. (Reproduced with permission from *The Journal of Chemical Physics*, Van Duzor *et al.*, Nov. 2010, Vol. 133, 144303-144312. ©2010 *American Institute of Physics*.)

Treating the vibrational modes as harmonic oscillators, we follow the approach of Sharp and Rosenstock[185, 186] accounting for the Duchinsky effect in the manner described by Chen.[187, 188] A problem for cluster anion detachment is the subsequent fragmentation of the cluster framework (into I + CH_3X) as the excess electron is removed. However, the van der Waals mode frequencies are smaller by at least an order of magnitude than the normal modes of the molecular moiety. We therefore assume that the normal modes of the molecular moiety can be treated separately from the van der Waals modes. Normal mode analysis supports this approach, showing that relative motion of the non-covalently bound I atom is negligible in all but the

van der Waals modes. This prompts us to ignore the presence of the non-covalently bound I atom in the Franck-Condon treatment.

Relative to the 0_0^0 transition, the FCFs are highest for excitation of 1 quantum in the ν_3 mode, $\sim$0.1 for detachment from all three cluster anions. This is at least an order of magnitude higher than the FCFs for single quantum excitation of any of the other modes, and of these, only the a_1 symmetry modes[183, 184] have FCFs $> 1\times10^{-3}$ relative to 0_0^0. This reinforces the expectation that C-X stretching motion is likely to be most prominently excited. More importantly, the FCFs associated with detachment from all three cluster anions are very similar. Given the eBE of each cluster anion, the FC prediction is that the intensities of equivalent transitions (relative to 0_0^0) in the photoelectron spectra should be similar for all three cluster anions.

In the spectra of Figures 5.3 and 5.4, the average spacing between transitions (60 ± 10 meV, 80 ± 10 meV and 100 ± 10 meV for CH_3X, X = I, Br, Cl respectively) is consistent with the vibrational frequency of the ν_3 mode of the appropriate methyl halide (66 meV, 76 meV and 91 meV for X = I, Br and Cl, respectively).[4, 116, 184] However, the extent of vibrational excitation present in the $I^-\cdot CH_3I$ spectrum is much higher than in the other cluster anions. As seen in Figure 5.4, evidence of up to 3 quanta of excitation in the C-I stretch is visible in the 340 nm spectrum. It is quantitatively difficult to assess the extent of non-FC character in these spectra for reasons of signal to noise ratio, instrument resolution and threshold effects which cause the detachment cross section to vary as a function of eKE. Nevertheless, comparison of the spectra from the three different cluster anions clearly indicate significant non-FC behavior in the $I^-\cdot CH_3I$ detachment process.

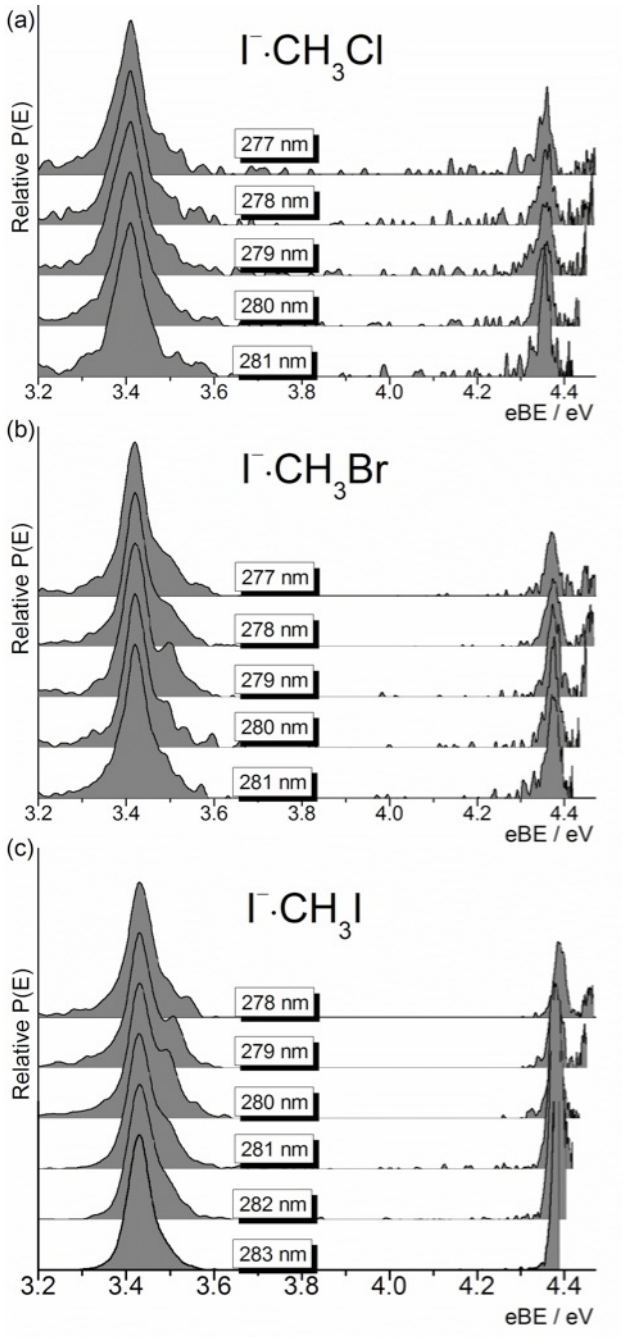

H

Figure 5.5: $I^{-}{\cdot}CH_3X$ photodetachment spectra (as a function of eBE) for photon energies near the $^2P_{1/2}$ threshold (a) X=Cl, (b) X=Br and (c) X=I. (Reproduced with permission from *The Journal of Chemical Physics*, Van Duzor *et al.*, Nov. 2010, Vol. 133, 144303-144312. ©2010 *American Institute of Physics.*)

As the photon wavelength is decreased further from the $^2P_{3/2}$ threshold, (down to 285 nm) the vibrational structure becomes less evident in the spectra of all three cluster anions. For X = Cl, Br, this is presumably due to the decrease in resolution associated with the imaging arrangement as the electron kinetic energy increases, as outlined in section 2.3.4. In the case of $I^-{\cdot}CH_3I$ photodetachment this is also due to a decrease in the level of vibrational excitation, the reason for which will be discussed later. As previously noted, the data do not allow a true quantitative assessment of the vibrational population of neutral CH_3X. However, changes in the level of vibrational excitation can be identified in a qualitative manner by careful examination of experimental images or spectra.

A very interesting example of this is found as the photon energy is tuned through the region immediately above the $^2P_{1/2}$ threshold in the cluster anions. Figure 5.5 shows the evolution of vibrational features in both the $^2P_{3/2}$ and $^2P_{1/2}$ channels as the photon energy is varied within an approximate range of 150 meV above the $^2P_{1/2}$ VDE. For example, Figure 5.5(c) shows the emergence of a shoulder in the $I^-{\cdot}CH_3I$ $^2P_{3/2}$ feature in the photoelectron spectrum. This partially resolves at 280 and 279 nm before the level of vibrational excitation associated with the $^2P_{3/2}$ channel decreases upon further increase of photon energy. It should also be noted that the decrease in vibrational intensity in the $^2P_{3/2}$ channel occurs as the first vibrational feature emerges in the $^2P_{1/2}$ channel.

The photoelectron images for the $I^-{\cdot}CH_3I$ detachment can be used to give a clear visual indication of this behavior. Figure 5.6 displays the upper right quadrant of images recorded at detachment wavelengths 280 and 278 nm. Two distinct vibrational transitions are seen in the outer ($^2P_{3/2}$) feature of the image at 280 nm. However, at 278 nm, a second transition begins to emerge at the center of the image (the lower

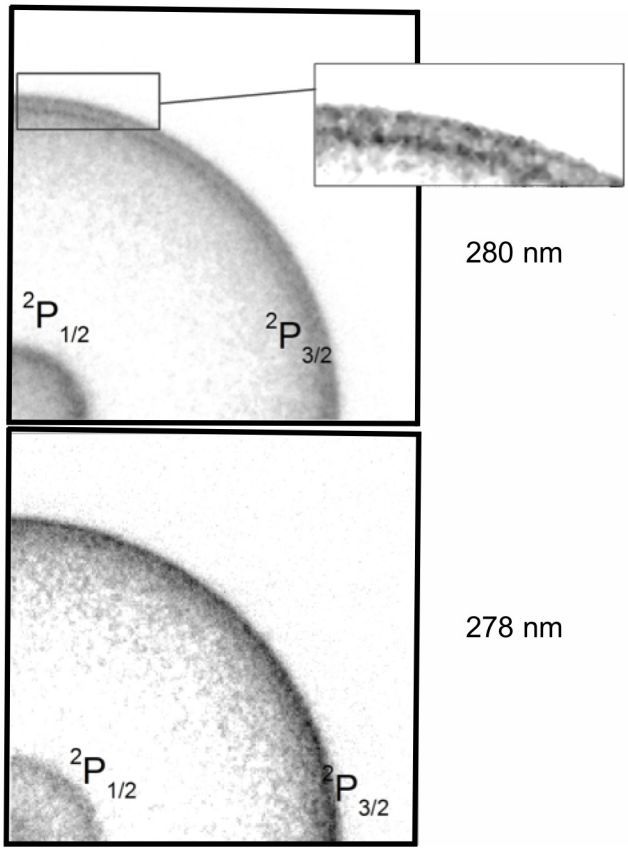

Figure 5.6: Upper right quadrant of the 280 nm and 278 nm photodetachment images of $I^-{\cdot}CH_3I$. The vibrational structure in the photoelectron spectrum of the $^2P_{3/2}$ feature is clear in the 280 nm image. (Reproduced with permission from *The Journal of Chemical Physics*, Van Duzor *et al.*, Nov. 2010, Vol. 133, 144303-144312. ©2010 *American Institute of Physics*.)

left corner of the quadrant shown), while the $^2P_{3/2}$ region does not show two easily distinguishable features. The spectra in Figure 5.5(b) show similar behavior in the $^2P_{3/2}$ channel for $I^-{\cdot}CH_3Br$. The emergence and disappearance of partially resolved vibrational structure is again evident, albeit at slightly different photon energies, due to the different solvent shifts and vibrational frequencies. This behavior is less prominent in the $I^-{\cdot}CH_3Cl$ spectra of Figure 5.5(a). However, it should be stressed that the image quality is poorer for the $I^-{\cdot}CH_3Cl$ cluster anion due to lower ion yield.

5.3.3 Cluster Fragmentation Channels

In the region of both channel thresholds in $I^-{\cdot}CH_3I$ detachment, an extra, higher eKE feature is observed in the photoelectron spectrum. This feature (which disappears at photon energies between the threshold regions) corresponds to an electron binding energy of 3.06 eV, the electron affinity of an iodine atom. This spectral feature, which was noted in chapter 4, is indicated by the downward arrow in Figures 5.1, 5.3, and 5.4. The corresponding feature is difficult to discern in the images presented in Figures 5.3, 5.4 and 5.6 due to the contrast ratio of the figures, but is clear in the spectra. As discussed in chapter 4, detection of I^- occurs as the result of a sequential two photon process.[109, 121] The first photon creates the methyl iodide anion which subsequently dissociates within the temporal width of the ns laser pulse, the second photon effecting detachment from the atomic iodide product. The fragmentation channel feature displays the expected quadratic dependence on the photon intensity and furthermore, this interpretation is consistent with previous observations made for this cluster anion.[3–5, 104] The absence of a transition corresponding to detachment via the $^2P_{1/2}$ state of the I^- product at (for example) 280 nm is likely to be due to the lower intensity of this transition, which presumably places it below the detection limit for this two photon process.

Features corresponding to X^- (X=Br, Cl) in the near threshold regions of the other cluster anions are conspicuously absent. This should not be taken to completely rule out dissociation to produce the X^- anion. In the case of the $I^-{\cdot}CH_3Cl$ $^2P_{3/2}$ threshold the photon energy (3.41 eV) is smaller than the electron affinity of Cl (3.62 eV)[189]. However, at either threshold for $I^-{\cdot}CH_3Br$ and at the $^2P_{1/2}$ threshold of $I^-{\cdot}CH_3Cl$ (4.35 eV) there would be sufficient photon energy to detach from the halide atomic anion. Again, caution must be exercised since the absence of a fragment

$^2P_{1/2}$ feature for $I^-\cdot CH_3I$ excitation highlights the sensitivity limitation to this two photon process. However, it is at least clear that the fragmentation cross section is significantly curtailed (to below the two photon detection limit) in the $I^-\cdot CH_3Br$, and $I^-\cdot CH_3Cl$ cluster anions.

5.3.4 Cluster Anion Photoelectron Angular Distributions

Anisotrpy parameter (β) values for each of the over 80 measurements made were extracted through application of the equation $I(\theta) = \sigma/4\pi\,[1 + \beta P_2(\cos\theta)]$ as, detailed in section 2.2 (Equation 2.21). Figure 5.7 displays β for electrons from the $^2P_{3/2}$ channel taken from the images for each cluster anion and bare I^-, as a function of eKE. Each β value presented represents a measurement at a specific detachment wavelength and results from averaging over the energy range corresponding to the FWHM of the $^2P_{3/2}$ transition as described in chapter 3. In the case of photodetachment from an atomic anion, β depends upon the parent orbital angular momentum ℓ and the kinetic energy of the departing electron (see chapter 2). Due to the observed similarity of the spectral features to those of atomic I^- photodetachment, as well as the calculated localization of the excess electron upon the I atomic moiety within the cluster, this definition of the parent orbital is assumed also to be valid for the cluster anions.

The initial decrease to a minimum (maximum negative value) and subsequent increase in the I^- β value of Figure 5.7(a) (filled circles) is the behavior expected for photodetachment from an atomic p orbital.[119, 120] It should be noted that several more data points have been included in this study of I^- photodetachment than in

the previous chapter. This was done in order to have a point of reference across the region in which the $^2P_{1/2}$ photodetachment channel opens.

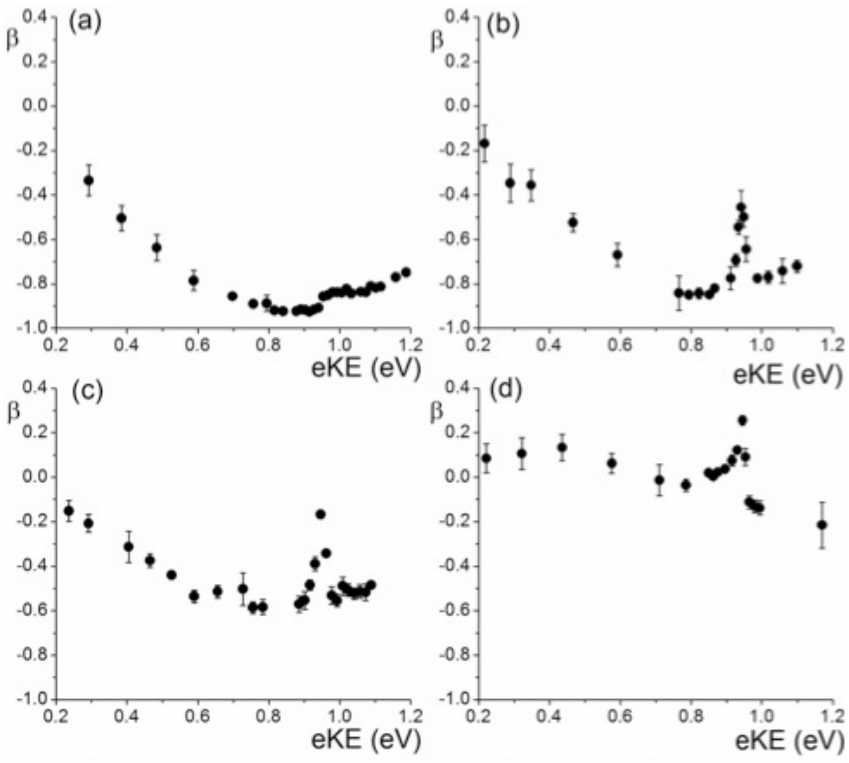

Figure 5.7: β parameters extracted from the $^2P_{3/2}$ (v = 0) transition in the photoelectron spectrum for (a) I^-, (b) $I^-{\cdot}CH_3Cl$, (c) $I^-{\cdot}CH_3Br$, and (d) $I^-{\cdot}CH_3I$. Each data point represents a different detachment wavelength. (Reproduced with permission from *The Journal of Chemical Physics*, Van Duzor *et al.*, Nov. 2010, Vol. 133, 144303-144312. ©2010 *American Institute of Physics.*)

The PADs from the $I^-{\cdot}CH_3X$ cluster anions present several distinct and interesting features. In the low eKE regime ($0 - 0.90$ eV) the $I^-{\cdot}CH_3Cl$ and $I^-{\cdot}CH_3Br$ data exhibit similar general behavior to I^- as the eKE increases. Quantitatively, the anisotropy parameters extracted from the $I^-{\cdot}CH_3Cl$ images are very similar to I^-, while $I^-{\cdot}CH_3Br$ values display a shallower gradient. The β values extracted from the $I^-{\cdot}CH_3I$ images display very different behavior over this interval. The initial trend is

toward more positive β at lower energies, showing a slight preference for polarization parallel to the laser electric vector.

While the low energy cluster anion PADs display different behavior in the low eKE regime, they all undergo a dramatic change just above 0.9 eV. This interesting detail falls between the data points presented for $I^-{\cdot}CH_3I$ presented in chapter 4. Photodetachment from each of the cluster anions produces a pronounced peak in the β vs. eKE progression at 0.94 eV. This is the same as the spin-orbit splitting between the two low lying states of the I atom. Consequently, the peak in the $^2P_{3/2}$ β evolution with eKE corresponds to photon energies in the $^2P_{1/2}$ channel threshold region.

5.4 Discussion

The photodetachment properties observed in the $I^-{\cdot}CH_3X$ cluster anions bear similarities to previously reported methyl halide-electron scattering measurements. In turn, these are heavily influenced by the relative location of the ground state potential surface of the neutral molecule and a low lying, dissociative anionic state. The neutral and anion states are most conveniently illustrated schematically, using the generic, pseudo-diatomic potentials of Figure 5.8. The CH_3X^- state lies within a few eV of the neutral ground state at the equilibrium geometry (R^e_{CX}) and the proximity (quantified by the vertical attachment energy, VAE) increases across the series X = Cl, Br, I.[6, 10, 172] The separation also decreases as R_{CX} increases until, at a critical distance R^c_{CX}, the anion and neutral diabats cross.

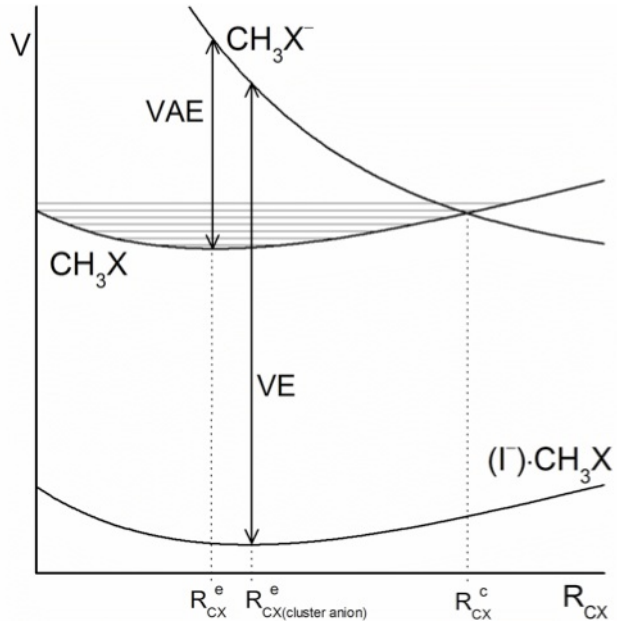

Figure 5.8: Generic, pseudo-diatomic diabatic potentials for CH_3X and CH_3X^-. R^e_{CX} represents the free CH_3X equilibrium C-X bond length, $R^e_{CX(cluster\ anion)}$ is the equivalent length in the cluster and R^c_{CX} is the crossing point of the CH_3X and CH_3X^- diabats. (Reproduced with permission from *The Journal of Chemical Physics*, Van Duzor *et al.*, Nov. 2010, Vol. 133, 144303-144312. ©2010 *American Institute of Physics*.)

5.4.1 Summary of Electron-Methyl Halide Interactions

Very low energy scattering or laser photoelectron attachment experiments, and supporting theoretical work has shown that in the region of R^c_{CX}, vibrational Feshbach resonances mediate vibrationally inelastic scattering and DEA in each CH_3X.[6, 10, 32, 106, 147–149, 151–162, 164, 167, 168, 170, 172] However, the cross sections for these processes are temperature dependent. The crossing point lies in the vicinity of a vibrationally excited level and thus capture into the resonance is enhanced by initial vibrational excitation.[148–150, 152, 154, 155, 159, 162] Furthermore, the ν_3 quantum number associated with the resonance becomes progressively higher as the substituent halide changes from I to Cl.[6, 9, 32, 153, 172] Complication arises in the

presence of a low lying shape resonance in all three CH_3X molecules, [7, 8, 102, 103, 127, 135, 136, 143–147, 165, 166, 168, 169] also associated with capture of the electron into the σ^* orbital. This is the result of the presence of the CH_3X^- state embedded in the detachment continuum. Vibrationally inelastic scattering has been observed in electron energy loss spectra of all three species at incident electron energies lying within the widths of the shape resonance.[165, 166, 169]

The shape resonance may also be responsible for DEA. The extent is dependent on the temporary anion survival time, subsequent to electron capture into the σ^* orbital. If the anion survives long enough, R_{CX} may exceed R^c_{CX}.[143, 147, 169, 190] The survival probability decreases with increasing (VAE),[143, 147] which is 1.4 eV, for CH_3I,[145] 2.4 eV for CH_3Br,[145] and 3.45 eV for CH_3Cl.[168]

5.4.2 Cluster Anion Vibrational Excitation and Fragmentation

Some vibrational structure is expected in the cluster anion spectra on Franck-Condon grounds.[107] However, the vibrational structure in the $I^-{\cdot}CH_3I$ photoelectron spectra of Figures 5.3 and 5.4 is enhanced compared to that of the other cluster anions near the $^2P_{3/2}$ threshold. Furthermore, there is evidence for I^- production at these wavelengths. The reasons for this behavior have been covered in detail by Johnson and co-workers.[104] In brief, the vibrational Feshbach resonance dominates the photoexcitation near threshold. The distortion of the CH_3I moiety actually enhances vertical excitation (VE) to the resonance region of the potential surface. At very low eKE the molecular dipole moment is sufficient to create a virtual dipole bound state

which mediates capture of the electron into the σ^* orbital. The C-I bond lengthens and the anion undergoes vibrational autodetachment or even dissociative attachment.

The absence of fragmentation and enhanced vibrational excitation in the X = Br and Cl cluster anion spectra is also relatively easy to understand in terms of the free molecule results discussed above. The cluster induced distortion is not sufficient to access the regions of the CH_3X potential associated with the higher vibrational levels necessary for vertical excitation in these species. Cluster anions containing vibrationally excited CH_3X molecules do not survive to reach the detection region of the instrument and so the cluster approach is effectively specific to the lowest vibrational levels.

The presence of the shape resonance may also be felt in the cluster anion experiments. For the $I^-{\cdot}CH_3I$ cluster anion, the VAE and width of the resonance certainly make it accessible at the photon energies used in these experiments. Unfortunately, the relative contributions of the shape and vibrational Feshbach resonances to the vibrational structure and fragmentation are difficult to separate for $I^-{\cdot}CH_3I$. For the other cluster anions, the VAE for X = Cl (3.45 eV)[168] and Br (2.4 eV)[145] would correspond to VE (Figure 5.8) with $E_{h\nu} > 6$ and 5 eV respectively.

The photon energies used in the current work lie outside the width of the resonance for X = Cl (3.05 eV),[168] while for X = Br excitation will merely access the wings, reducing its effect. Although unobserved in the present measurements, tandem mass spectrometry has detected Br^- subsequent to $I^-{\cdot}CH_3Br$ photoexcitation in the $^2P_{3/2}$ threshold region.[3] The yield is at least an order of magnitude smaller than in $I^-{\cdot}CH_3I$ and is likely to be the result of excitation into the edge of the σ^* resonance. In the current work the reduced yield, combined with the necessity of Br^-

photoexcitation places Br^- below the detection limit. The $^2P_{1/2}$ region of the cluster anion spectra also shows evidence of vibrational excitation and a reappearance of the I^- fragment for $I^-{\cdot}CH_3I$. Energy conservation suggests the $^2P_{1/2}$ features should lag those of the $^2P_{3/2}$ channel by 0.94 eV, meaning that similar features are not unexpected in the two channels at comparable eKE. This is a reasonable zero order picture although the presence of the excited I atom gives rise to additional, cluster specific effects, which are discussed later.

5.4.3 Cluster Anion Angular Distributions

Over the eKE range 0-0.9 eV, the β parameter associated with the $^2P_{3/2}$ channel for $I^-{\cdot}CH_3Cl$ is very similar to that of free I^- detachment. Conversely, that of the $I^-{\cdot}CH_3I$ $^2P_{3/2}$ channel is clearly very different. The $I^-{\cdot}CH_3Br$ cluster anion represents something of an intermediate case. These effects are not attributable to the dipole of the molecular residue. Electron-dipole moment interaction has previously been shown to exert a relatively minor effect on the PAD,[46, 191] even for molecules possessing dipole moments significantly greater than those of the methyl halides studied here (CH_3I= 1.647±0.014 D, CH_3Br= 1.797±0.015 D, CH_3Cl= 1.869±0.010 D).[46, 109–111, 192]

The eKE evolution of the $I^-{\cdot}CH_3I$ is the result of excitation of the σ^* resonance described earlier.[46, 109, 121] β(eKE) provides a particularly sensitive indicator for the resonance. Although quantitative treatment of the effect on β is complex, rationalization is relatively straightforward. The observed angular distribution reflects competition between direct detachment [$I^-{\cdot}CH_3I \rightarrow I(^2P_{3/2}) + CH_3I + e^-$] and temporary capture by the resonance [$I^-{\cdot}CH_3I \rightarrow I(^2P_{3/2}){\cdot}CH_3I^- \rightarrow I(^2P_{3/2}) + CH_3I +$

e^-]. The VAE and width of the resonance are critical. For $I^-{\cdot}CH_3Cl$, strong similarity of β(eKE) to that of I^- is consistent with the inaccessibility of the CH_3Cl σ^* resonance at photon energies below the $^2P_{1/2}$ threshold. $I^-{\cdot}CH_3Br$ detachment shows a small, but significant deviation from the I^- β(eKE) trend. The resonance becomes more prominent as $E_{h\nu}$ increases. The PAD associated with the $I^-{\cdot}CH_3I$ cluster anion, for which the VAE is much smaller, shows a pronounced effect.

5.4.4 Cluster Specific Effects: Excitation near the $^2P_{1/2}$ channel threshold

In the preceding, analogy with electron scattering from neutral CH_3X has been invoked to guide interpretation of the cluster anion photoexcitation results. However, the presence of the residual I atom also leads to effects associated solely with the cluster environment. For excitation energies < 0.9 eV above the $^2P_{3/2}$ threshold the iodine essentially behaves as a spectator atom. However, in a narrow energy window about the $^2P_{1/2}$ threshold, changes in the vibrational structure and PAD of the $^2P_{3/2}$ band are observed.

Excitation at the $^2P_{1/2}$ threshold initially produces a complex of $I(^2P_{1/2}){\cdot}CH_3X$ and a near-zero energy electron. The complex is stabilized by the cluster framework dipole moment which is close to the critical limit to support a dipole bound state. The complex can be viewed as a virtual dipole bound state[9, 10, 76, 104, 175] lying close to the $I(^2P_{1/2}){\cdot}CH_3X(v{=}0) + e^-$ direct detachment threshold. The presence of an excited I atom gives rise to the possibility of relaxation to $I(^2P_{3/2}){\cdot}CH_3X$, with the excess energy transferred to the departing electron. It may be inferred that this becomes more likely the longer the photoelectron amplitude is localized in the

vicinity of the excited I atom. Electrons produced via this mechanism are energetically indistinguishable from those produced via direct detachment into the $^2P_{3/2}$ channel at the same $E_{h\nu}$. The sensitivity of the PAD to competition between detachment channels has already been remarked upon. At photon energies consistent with the $^2P_{1/2}$ threshold region, competition between direct and autodetachment into the $^2P_{3/2}$ channel is the cause of the sharp deviation of β(eKE) in the narrow window around $E_{h\nu}$ = 0.94 eV for all the cluster anions in this study. Analogous behavior in the $I^-\cdot CH_3CN$ and $I^-\cdot H_2O$ cluster anions have also been reported.[111] The fact that all three methyl halide cluster anions show a similar effect strongly suggests that such localization-relaxation effects are common to dipolar cluster anions.

The rise and fall of a higher eBE shoulder in the $^2P_{3/2}$ feature between the $^2P_{1/2}$ v = 0 and v = 1 thresholds (Figure 5.5) reflects an enhancement of vibrational excitation in the neutral CH_3X molecules. This also is attributable to an electronic autodetachment mechanism if each vibronic threshold has an associated virtual dipole bound state. Similar states have been demonstrated just below the $^2P_{3/2}$ threshold of $I^-\cdot CH_3I$[104] and in detachment from $I^-\cdot H_2O$[193] as an enhancement of the detachment cross section. Enhancements of the overall detachment cross section have also been reported in the immediate pre-threshold region of the $^2P_{3/2}$ channel of $I^-\cdot$acetone[177] and $I^-\cdot$nitromethane[194] as well as the $^2P_{3/2}$ and $^2P_{1/2}$ channels of $I^-\cdot CH_3CN$[111, 177] photodetachment, systems which support true dipole bound states.

5.5 Summary

The shape and vibrational Feshbach resonances associated with electron-CH_3X interactions manifest themselves in the cluster anion photodetachment spectra and angular distributions. These interactions give rise to vibrational excitation of the neutral residue, cause DEA at low incident electron energies and strongly influence the photoelectron angular distribution.

Although many of the $I^-{\cdot}CH_3X$ photoexcitation results can be discussed using CH_3X-electron scattering analogies, the cluster experiment effectively selects vibrationally cold CH_3X molecules. Also observed are processes unique to the cluster environment. Excitation to the $^2P_{1/2}$ threshold reveals effects associated with vibronic coupling, facilitated by the creation of a virtual dipole bound state in proximity to the electronically excited iodine atom. Furthermore, changes in the cluster anion PAD (compared to the reference distribution of the anionic moiety) are a sensitive indicator of electronic autodetachment and other energetically indistinguishable processes. The chapter to follow further explores the effects of vibronic coupling and spin orbit relaxation in the halide core by substituting a chloride anion for the iodide anion moiety studied thus far.

Chapter 6

$Cl^-\cdot CH_3I$: The Effect of the Halide Anion Moiety on Intracluster and Electron-Molecule Interactions

6.1 Introduction

The photoelectron imaging investigations of $I^-\cdot CH_3I$, $I^-\cdot CH_3Br$, and $I^-\cdot CH_3Cl$ presented in the preceding chapters demonstrate that the photoelectron spectra and angular distributions are affected, to varying extent, by interaction of the departing electron with the methyl halide moieties. Results from the $I^-\cdot CH_3I$ cluster anion, in particular, shows effects mediated by the interplay of the neutral ground state of CH_3I and a low lying, dissociative anionic state associated with excess electron capture into a σ^* antibonding orbital.[46, 109, 121, 195] To a reasonable approximation, the photoelectron spectra can be explained by viewing photodetachment from

Portions of this chapter have been reproduced with permission from *The Journal of Chemical Physics*, Van Duzor *et al.*, May 2011, Vol. 134, 184315-184322.

such clusters as a multistep process: the excess electron is first removed from an atomic iodide anion, followed by interaction of the electron with the nearby neutral molecule.[4, 5, 46, 109, 121, 195] This chapter presents results for the closely related $Cl^{-}{\cdot}CH_3I$ cluster anion which highlight more of the intricacies of this detachment process.

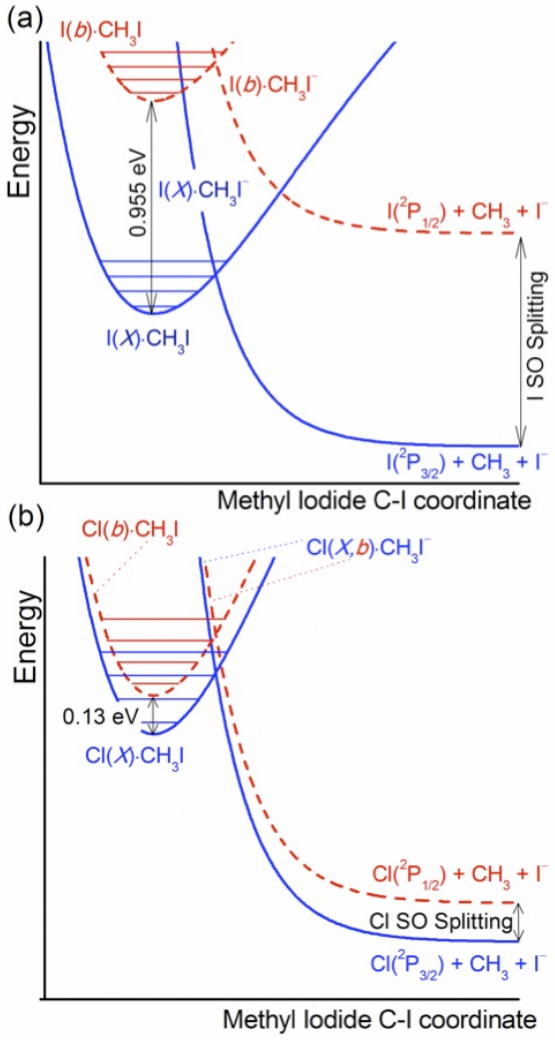

Figure 6.1: Potential curves along the methyl halide C-I coordinate associated with detachment via the b state (dashed lines) and X state (solid lines) (a) $I^{-}{\cdot}CH_3I$, (b) $Cl^{-}{\cdot}CH_3I$. (Reproduced with permission from *The Journal of Chemical Physics*, Van Duzor *et al.*, May 2011, Vol. 134, 184315-184322. ©2011 *American Institute of Physics.*)

The solid blue curves of Figure 6.1(a) are taken from the diabatic potentials associated with the interaction of a CH_3I molecule and a free electron along the along the methyl iodide C-I stretching coordinate.[6, 10, 32, 106] Just as in the $I^-{\cdot}CH_3I$ cluster anion, photoexcitation of $Cl^-{\cdot}CH_3I$ can be interpreted in terms of excitation into a the region where the CH_3I^- state lies above the neutral potential. The dynamics are therefore influenced by a temporary anion state (CH_3I^-) or resonance of the CH_3I + e^- system, resulting in elastic and inelastic scattering effects.[6, 10, 32, 102, 106] These effects are likewise expected to be revealed in the photoelectron angular distribution (PAD) and spectra.[46, 109, 121, 195] The departing electron is delayed relative to direct detachment by an amount proportional to the lifetime of the resonance. Sufficiently long lifetimes may allow for evolution of the nuclear wave function, resulting in electron loss from geometries outside the Franck-Condon envelope. Such inelastic scattering is observed as enhancement of vibrational features in the photoelectron spectrum.[3–5, 46, 104, 109, 116, 121, 195] If this evolution proceeds to the crossing point of the neutral and negative ion diabats, cleavage of the bond will occur, resulting in stable anionic fragments. Electron scattering studies of CH_3I molecules and neutral clusters have revealed a number of threshold peaks[6, 9, 10, 32, 102, 105] at low energy, most notably the vibrational Feshbach resonance (VFR) associated with the ν_3, v=1 state of CH_3I. Vertical excitation of the $I^-{\cdot}CH_3I$ cluster anion near the detachment threshold accesses the VFR region, resulting in non-Franck Condon enchancement of the ν_3, v=1 feature in the photoelectron spectrum as well as fragmentation.[3–5, 104, 109, 116, 121, 195]

The presence of vibronic transitions notwithstanding, the $I^-{\cdot}CH_3I$ detachment spectrum bears a strong similarity to that of the atomic iodide anion. With sufficient excitation energy, two bands are observed, which correlate to asymptotic $I(^2P_{3/2}$

or $^2P_{1/2}$) + CH_3I + e^- states. High resolution anion ZEKE (zero electron kinetic energy spectroscopy) measurements show the band origins to be separated by 0.955 ± 0.020 eV.[116] Within experimental error this is equivalent to the separation of the lowest electronic states of the iodine atom ($^2P_{3/2}$ and $^2P_{1/2}$). The potential energy diagram can be extended to illustrate the presence of the excited I atom using a second pair of CH_3I/CH_3I^- potentials, offset by the energy separation of the iodine atom states. These are the red dashed lines in Figure 6.1(a) which are labeled $I(b)\cdot CH_3I$ and $I(b)\cdot CH_3I^-$. In previous chapters, the states displayed in Figure 6.1 would be designated by the asymptotic electronic state of the neutral halogen core, an approximation that serves quite well for iodide centered clusters. As discussed in greater detail in section 6.4.3, the $Cl\cdot CH_3I$ neutral electronic states are not properly described in this limit. The change in labeling scheme between this and previous chapters is made in order to facilitate comparison between $I^-\cdot CH_3I$ and $Cl^-\cdot CH_3I$.

The marked effect of the interaction of the molecular states sketched in Figure 6.1(a) has already been remarked upon. Additionally, excitation into the region of the threshold of the $I(b)/^2P_{1/2}$ channel leads to an autodetachment process with energy transfer to the photoelectron as a result of relaxation of the $^2P_{1/2}$ state of the iodine atom.[109, 111, 195] Broadly speaking however, the large energy separation of the I atom states allows the $^2P_{1/2}$ and $^2P_{3/2}$ channels to be discussed as essentially separate.

The work comprising this chapter represents the first photodetachment imaging results for the $Cl^-\cdot CH_3I$ cluster anion. Substitution of a chlorine atom for the non-covalently bound iodine atom drastically reduces the separation of the two asymptotic product states from approximately 0.94 to 0.11 eV (Figure 6.1(b)), which is on the order of the vibrational energy level spacings in the CH_3I molecule,[196] and therefore brings the molecular diabats of each channel into closer proximity. Comparison of

$Cl^-{\cdot}CH_3I$ cluster anion detachment results with those of $I^-{\cdot}CH_3I$ will highlight the importance of interactions between the constituents of the neutral cluster (the cluster framework subsequent to photodetachment). Furthermore, the results presented here suggest that this may be a fruitful system for higher resolution detachment studies that are becoming available through the new generation of photoelectron imaging spectrometers.[54, 55]

6.2 Experimental Details

Photoelectron images of $Cl^-{\cdot}CH_3I$ were collected at 5-10 nm intervals over a range from 295-270 nm. $Cl^-{\cdot}CH_3I$ cluster anions were prepared by passing a gaseous mixture of $\sim 10\%$ CH_3I in Ar over liquid CCl_4 and expanding through the aperture of a general valve series 9 pulsed nozzle (10 Hz repetition rate) into the ion source chamber maintained at $4{\times}10^{-5}$ Torr. The supersonic expansion intersects a 1 kV electron beam, resulting in cluster anion formation through the electron impact ionization method (section 3.2.2).

The detachment laser is gently focused with a spherical lens (focal length 1 m), resulting in average intensities (of the 4-14 mJ pulses) always being $< 1{\times}10^8$ W cm^{-2}. The momentum space distribution of photoelectrons is reconstructed from the image using the BASEX program of Dribinski et al [92] allowing extraction of the photoelectron spectrum and angular distributions.

6.3 Results and Analysis

Photodetachment spectra of $Cl^- \cdot CH_3I$ recorded in the vicinity of the direct detachment threshold at 270, 280, 285, 290, and 295 nm are shown in Figure 6.2. Several transitions are observed at electron binding energies (eBE) > 4.0 eV. These features persist as the photon wavelength decreases, although a concurrent decrease in instrument resolution makes them harder to distinguish in the 270 nm spectrum.

6.3.1 Evidence of Fragmentation

There are some weaker spectral features in the region between 3.0 and 4.0 eV in many of the spectra. The intensity (and presence) of these features is dependent on the photon wavelength employed, and close to the S/N limit. However, inspection of the corresponding photoelectron images gives a very good qualitative indication of their veracity. Figure 6.3 illustrates this for 285 nm photodetachment. The more intense spectral transitions (eBE > 4.0 eV) are seen as a series of concentric rings near the center of the detector in Figure 6.3(b). Upon rescaling the image (Figure 6.3(a)) to emphasize the lower intensity region the presence of the weaker spectral features become clear.

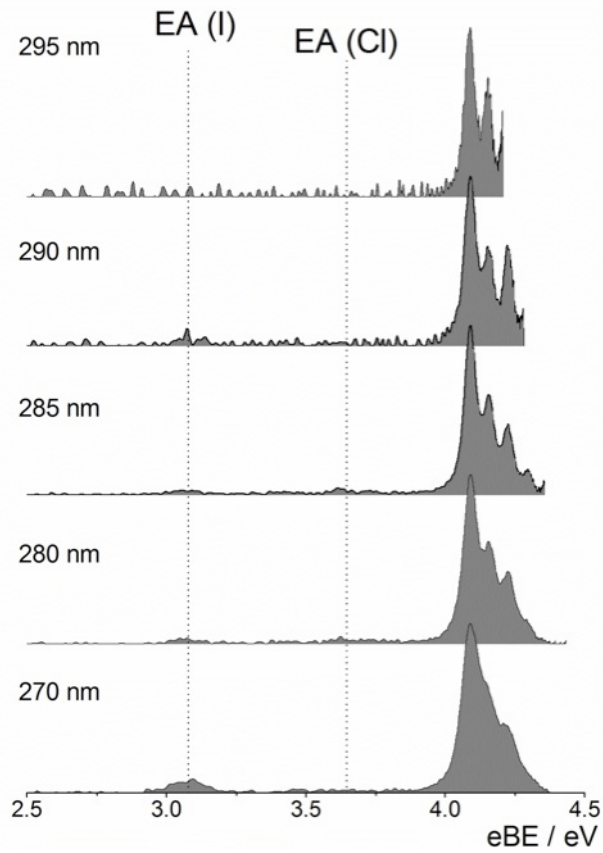

Figure 6.2: Electron binding energy domain photoelectron spectra of $Cl^- \cdot CH_3I$ taken at 295, 290, 285, 280, and 270 nm. (Reproduced with permission from *The Journal of Chemical Physics*, Van Duzor *et al.*, May 2011, Vol. 134, 184315-184322. ©2011 *American Institute of Physics.*)

The 280 and 285 nm images and binding energy domain spectra show two, photon energy dependent features at 3.62 and 3.73 eV. The 290-270 nm spectra show another transition at 3.06 eV. The closely spaced pair corresponds to the energy required to effect detachment from free Cl^- via the first two electronic states of the Cl atom, whilst 3.06 eV corresponds to the electron affinity (EA) of the iodine atom.[197] I^- and Cl^- fragments are produced as a result of initial photoexcitation. The photoelectrons seen in the eBE $<$ 4.0 eV region are then detached from the atomic anions via a second photon within the ns laser pulse. In the current experiments, the

already low intensity of these features rules out verification of this two photon mechanism by variation of incident laser power. However, a similar two-photon dependent I^- photoelectron signal was demonstrated in $I^-{\cdot}CH_3I$ detachment in chapters 4 and 5.

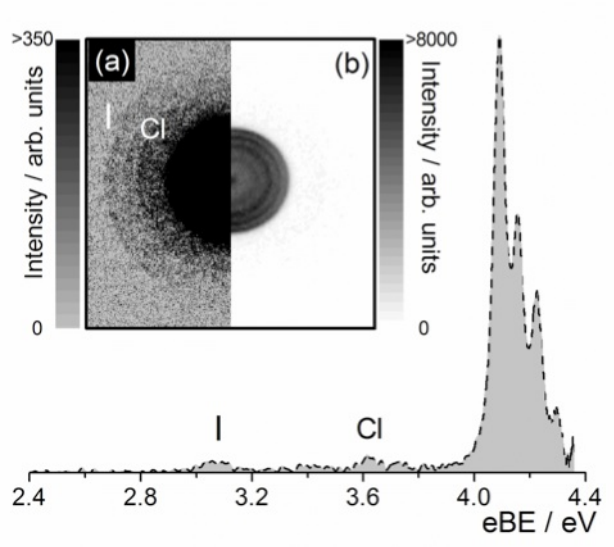

Figure 6.3: 285 nm image and binding energy domain spectrum of $Cl^-{\cdot}CH_3I$. (a) scales the intensity of image (b) to highlight the lower binding energy features. (Reproduced with permission from *The Journal of Chemical Physics*, Van Duzor *et al.*, May 2011, Vol. 134, 184315-184322. ©2011 *American Institute of Physics.*)

6.3.2 Spectral Features

Returning attention to the eBE > 4.0 eV region of the spectra, the transition energies and relative intensities can be estimated by fitting the spectrum with a series of Lorentzian functions. The peak of the strongest spectral transition is 4.08 ± 0.01 eV, shifted 0.47 eV relative to the electron affinity of Cl. The mean separation between consecutive higher binding energy peaks is 70 ± 5 meV. The uncertainty represents one standard deviation from the mean across all detachment wavelengths. Within the uncertainty limits, this spacing is in excellent agreement with previously reported

measurements of the (predominantly) C-I stretching frequency for CH_3I (ν_3) and the analogous mode in the $I^-{\cdot}CH_3I$ cluster anion.[4, 116, 121, 184] Relative transition intensities are estimated from areas of the fitting functions and shown in Table 6.1, where the uncertainties are gleaned from the non-linear least squares, Levenberg-Marquardt fitting procedure.

Table 6.1: Relative intensities of vibronic transitions in the $Cl^-{\cdot}CH_3I$ photodetachment spectra [see text for details]. (Reproduced with permission from *The Journal of Chemical Physics*, Van Duzor *et al.*, May 2011, Vol. 134, 184315-184322. ©2011 *American Institute of Physics.*)

	Transition Peak eBE/eV			
λ, nm	4.08 eV	4.15 eV	4.22 eV	4.29 eV
295	1.00±0.009	0.52±0.02	-	-
290	1.00±0.01	0.35±0.03	0.46±0.02	-
285	1.00±0.006	0.46±0.02	0.33±0.02	0.06±0.04
280	1.00±0.008	0.54±0.02	0.38±0.02	0.05±0.05
270	1.00±0.01	0.56±0.06	0.35±0.03	0.09±0.05

6.3.3 Photoelectron Angular Distributions

Examination of Figure 6.3(b) shows that the eBE > 4.0 eV transitions generally correspond to a preference for photoelectron ejection in the direction of the electric field vector of the polarized laser beam. A similar preference for ejection along the electric field vector, corresponding to positive anisotropy parameters (β) is observed for these transitions at all wavelengths in this study. Anisotropy parameters collected from $Cl^-{\cdot}CH_3I$ and Cl^- photodetachment experiments can be found in Figure 6.4.

This is in contrast to the polarization in the angular distribution of the free atomic anion. For example, Cl^- detachment at 310 nm (eKE = 0.36 eV) yields $\beta = -0.39 \pm 0.06$. In contrast, the β parameter of the 4.08 eV binding energy transition in the 280 nm $Cl^- \cdot CH_3I$ detachment spectrum (eKE = 0.34 eV) is $+0.34 \pm 0.02$. The reversal of polarization between the cluster and parent anion angular distribution is unusual. In the majority of cases reported to date, angular distributions for free atomic anions and their associated cluster anions are very similar in the low eKE range (e.g. $I^- \cdot CH_3Cl$, $I^- \cdot CH_3CN$, $I^- \cdot H_2O$ at eKE < 0.9 eV, as well as chapter 5.)[46, 111, 195] However, a similar reversal of the polarization of the angular distribution was observed in $I^- \cdot CH_3I$ cluster anion detachment, as has been detailed in chapters 4 and 5.[46, 109, 121, 195]

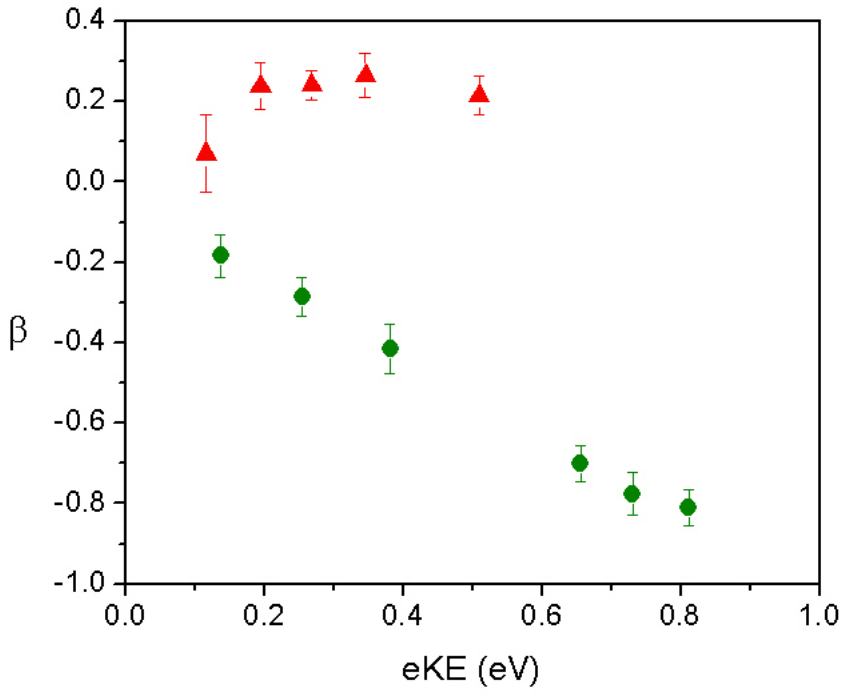

Figure 6.4: Anisotropy parameters (β) extracted from the $Cl(X) \cdot CH_3I$ detachment channel at wavelengths of 295, 290, 285, 280 and 270 nm (red triangles) and from $Cl(^2P_{3/2})$ at 330, 320, 310, 290, 280 and 270 nm.

6.4 Discussion

To summarize; photoexcitation of the $Cl^-{\cdot}CH_3I$ cluster anion at photon energies between 4.2 and 4.6 eV leads to competition between fragmentation to atomic anion products and single photon detachment yielding PADs which significantly differ from those of Cl^- detachment. Furthermore, the single photon detachment produces a series of transitions with a spacing similar to the CH_3I (ν_3) stretching frequency. Comparison with $I^-{\cdot}CH_3I$ cluster anion detachment[3–5, 46, 104, 109, 116, 121, 195] is particularly interesting and similarities and differences between the two cluster anions will be discussed below.

6.4.1 Photoelectron Angular Distributions

In both cases the cluster anion photoelectron angular distributions show marked deviation from those of the free atomic halide. The CH_3I moiety is responsible through the anionic state embedded in the detachment continuum (Figures 4.1, 6.1). As discussed in previous chapters, this creates the conditions for excitation of a temporary anion state such as a shape resonance,[140] or a zero energy resonance supported by the dipole moment of the cluster framework.[32, 41, 104] The resultant phase shift between the s- and d-wave components of the free electron wave function leads to the strong change in the β values between A^- and $A^-{\cdot}CH_3I$, (A= Cl, I) detachment.

6.4.2 Fragmentation Channels

Photoexcitation of $I^-{\cdot}CH_3I$ close to the detachment threshold produces I^-. Several publications have discussed this in terms of the effect of the negative ion resonances associated with the CH_3I potential energy curves shown in Figure 6.1.[109],[3–5, 116, 121, 195] The results presented here show evidence of fragmentation in the 290, 285, 280 and 270 nm $Cl^-{\cdot}CH_3I$ photoelectron spectra. I^- and Cl^- fragment signatures are discernible, with the latter being observed in only the 285 and 280 nm spectra.

The most plausible explanation for the presence of the I^- and Cl^- features in the spectrum is that they are the result of a two photon process. Photoexcitation effects an electron transfer to the CH_3I moiety, which is followed by either fragmentation of the resulting transient molecular anion (along the C-I bond) or electron scavenging by the Cl atom.[41] Fragmentation of either the cluster anion or of the CH_3I moiety within the cluster will occur on a timescale that is short compared to the ns width of the laser pulse. A second photon within the pulse detaches the excess electron from the product fragment. An alternative source of Cl^- ions would be fragmentation of vibrationally excited cluster anions within the anion TOF. In the current experiments, signal to noise issues make it impossible to verify the photon intensity dependence of the lower binding energy features in the $Cl^-{\cdot}CH_3I$ spectra. However, the absence of the Cl^- transitions at most excitation wavelengths argues strongly in favor of a two photon process and the initial formation of an excited anionic intermediate state. The appearance of the I^- spectral signature subsequent to $Cl^-{\cdot}CH_3I$ photoexcitation clearly demonstrates the presence of the CH_3I^- fragmentation channel.[3–5]

6.4.3 Single Photon Detachment Spectra

The biggest difference between the $I^-{\cdot}CH_3I$ and $Cl^-{\cdot}CH_3I$ photoexcitation results is found in the single photon detachment spectra. In previous chapters, the spectral features for such cluster anions was conveniently expressed in terms of the corresponding free atomic halide anion spectra. At sufficient photon energy, these contain two transitions $A^- \rightarrow (A\ (^2P_{3/2}) + e^-$, and $A^- \rightarrow A\ (^2P_{1/2}) + e^-\ )$ separated by the relative energy of the (lower) $^2P_{3/2}$ and (upper) $^2P_{1/2}$ spin-orbit states.[118]

$I^-{\cdot}CH_3I$ has two low lying vibronic bands, separated (within experimental error) by the splitting of the I atom spin-orbit states.[3–5, 104, 109, 116, 121, 195] High resolution ZEKE measurements show the binding energies of the band origins differ by 0.955 ± 0.020 eV.[116] Hence the bands clearly correlate to production of different iodine atom states ($^2P_{3/2}$ and $^2P_{1/2}$). Within these bands the vibrational features are mainly associated with the CH_3I ν_3 (predominantly C-I stretching) mode.

Figure 6.5 compares the 280 nm $Cl^-{\cdot}CH_3I$ spectrum with Cl^- and $I^-{\cdot}CH_3I$ detachment. The 280 nm $Cl^-{\cdot}CH_3I$ (open circles) and 320 nm Cl^- (solid red line) spectra are shown in Figure 6.6(a). The Cl^- spectrum has been shifted by 0.47 eV, matching the cluster anion origin, to facilitate comparison between the free and clustered atomic anion spectra. This gives an instant visual indication that the atomic $Cl^- \rightarrow Cl(^2P_{1/2})$ transition falls between two maxima in the cluster anion spectrum. In fact, the single photon transition spacings (70 ± 5 meV) in Figures 6.2 and 6.5 are consistent with a vibrational progression associated with excitation of the CH_3I ν_3 mode (533 cm^{-1}).[184] Comparison with the lowest binding energy band of $I^-{\cdot}CH_3I$ [shown for 340 nm excitation in Figure 6.5(b)] reinforces this impression.[5] Although

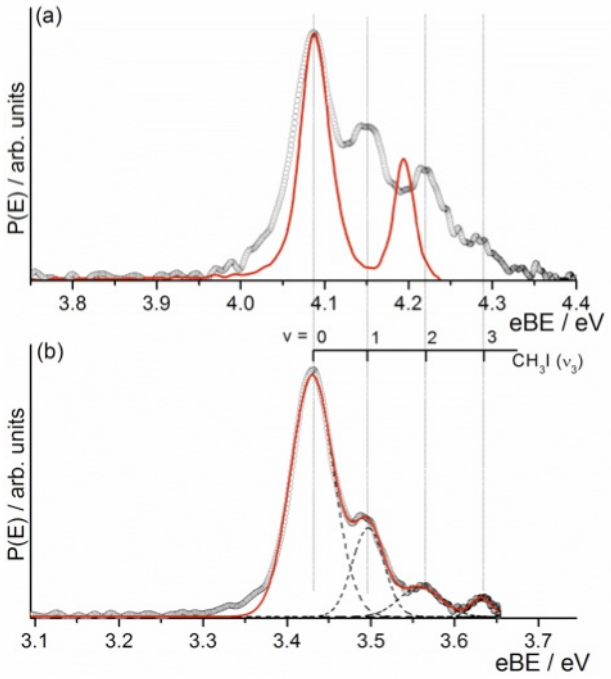

Figure 6.5: (a) Comparison of 280 nm $Cl^-{\cdot}CH_3I$ detachment (open circles) with 320 nm Cl^- detachment (solid line). The Cl^- spectrum is offset by 0.47 eV. (b) 280 nm detachment spectrum of $I^-{\cdot}CH_3I$ detachment (open circles) along with Lorentzian fits (dashed lines) to each transition and an overall fit (solid line) of these Lorentzian functions to the spectrum. (Reproduced with permission from *The Journal of Chemical Physics*, Van Duzor *et al.*, May 2011, Vol. 134, 184315-184322. ©2011 *American Institute of Physics.*)

the intensities are somewhat different, the transition spacings are identical to those in the $Cl^-{\cdot}CH_3I$ spectra. The immediate impression is one of suppression of the $^2P_{1/2}$ channel for $Cl^-{\cdot}CH_3I$ detachment.

In chapter 5, Franck-Condon factors, obtained through ab initio MP2 calculations (using basis sets aug-cc-pVDZ for H, C, Cl and aug-cc-pVDZ-pp ecp for I), showed that the vibrational excitation displayed in $I^-{\cdot}CH_3I$ detachment is greater than expected on the grounds of the CH_3I geometric distortion imparted by the cluster anion environment.[185, 186, 195] Using the same approach, the minor geometrical

Table 6.2: *Ab initio* MP2 geometries of neutral CH_3I and the $Cl^-\cdot CH_3I$ and $I^-\cdot CH_3I$ cluster anions. (Reproduced with permission from *The Journal of Chemical Physics*, Van Duzor *et al.*, May 2011, Vol. 134, 184315-184322. ©2011 *American Institute of Physics.*)

	$r_{C\text{-}I}$/Å	$r_{C\text{-}H}$/Å	∠HCI/degrees
$Cl^-\cdot CH_3I$	2.189	1.091	107.375
$I^-\cdot CH_3I$	2.180	1.091	107.888
CH_3I	2.149	1.095	107.742

distortions of the molecule (Table 6.2) in $Cl^-\cdot CH_3I$ cluster anion give rise to Franck-Condon factors which are very similar to those previously determined for $I^-\cdot CH_3I$ detachment. In the case of $Cl^-\cdot CH_3I$, the prediction is that the 4.15 eV transition intensity should be 15% of the 4.08 eV peak, and the 4.22 eV feature should be an order of magnitude smaller again. This is significantly different from the observations listed in table 6.1. The comparison of $Cl^-\cdot CH_3I$ and $I^-\cdot CH_3I$ detachment in Figure 6.5 also shows greater intensities in the $Cl^-\cdot CH_3I$ spectrum.

Suppression of the $^2P_{1/2}$ detachment channel has been reported in time resolved photoelectron studies of solution phase I^-.[198] However, the "absence" of spectral features correlating to the asymptotic $^2P_{1/2}$ state of the chlorine atom in the monosolvated species must be treated carefully. The transition energies in the spectrum are not governed by the asymptotic separation of the halogen atom states, as has been tacitly implied in the discussion to this point. The proximity of the non-covalently bound halogen atom to the molecular moiety lifts the degeneracy of the halogen atom orbitals.[199–201] For a C_{3v} arrangement, this leads to A_1 and E symmetry zero-order states, which are mixed by spin-orbit interaction. The resulting electronic

states (which will be labeled X, a, and b) eventually correlate to one or other of the asymptotic neutral states (X, a to $^2P_{3/2}$ and b to $^2P_{1/2}$).

Ab initio single point energy calculations provide the zero order state energies for the neutral cluster framework along the van der Waals stretching coordinate. The geometry of the CH_3I moiety is frozen and the zero order ground and excited state energies are calculated in Gaussian 03 [202] (MP2 using the aug-cc-pVDZ basis set for H, C, Cl and LANL2DZ ecp for I). The orbitals of the neutral cluster ground state form an initial guess for the excited state.[124] The effect of spin orbit coupling is then incorporated in the manner of References [199],[197, 203–205] to determine the A·CH_3I X-a and X-b state separations. For A = Cl, X-a = 0.032 eV and X-b = 0.131 eV, while for A = I, X-a = 0.051 eV and X-b = 0.968 eV, with the latter being in excellent accord with the I^-·CH_3I ZEKE measurements.[116] The calculated splitting of the upper and lower states in the Cl·CH_3I cluster differs from that of free Cl by nearly 19%, while the difference for I^-·CH_3I and I is only 3%. This, along with fact that the predicted I(a)·CH_3I state has never been observed spectroscopically (see discussion below) validates our prior use of the I state designations for the cluster anion photodetachment bands. In the case of Cl^-·CH_3I, it is clear that this useful approximation does not hold. The variation in the energy of the calculated states along the van der Waals stretching coordinate (relative to the X state in each case) is shown in Figure 6.6.

In principle, vertical excitation of the Cl^-·CH_3I cluster could access the Cl·CH_3I X, a, and b states. Simulation of the photoelectron spectrum using the Cl·CH_3I state energies is shown in Figure 6.7(a). A vibrational progression is incorporated for each electronic transition, using the Franck-Condon intensities calculated previously. Statistical weights based on the total electronic angular momentum of each state are

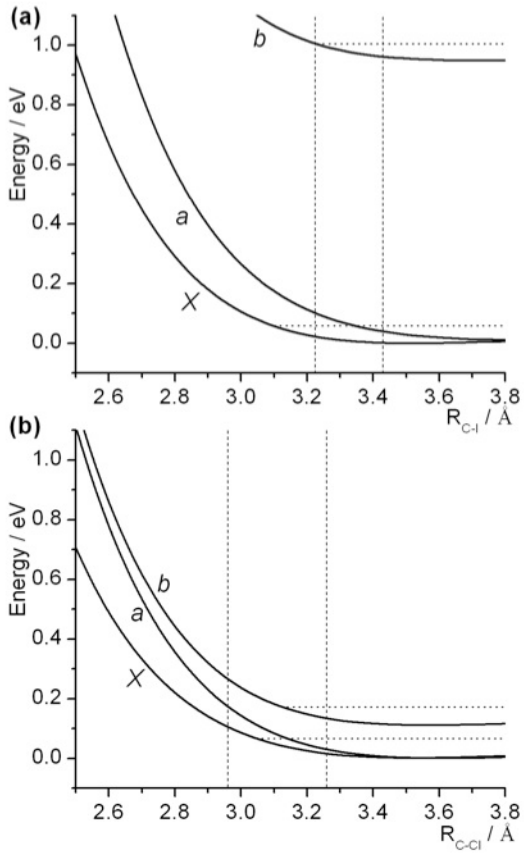

Figure 6.6: Variation of the potential energy of the cluster anion states along the van der Waals stretching coordinate, (a) $I^-{\cdot}CH_3I$, (b) $Cl^-{\cdot}CH_3I$ [see text for details]. (Reproduced with permission from *The Journal of Chemical Physics*, Van Duzor *et al.*, May 2011, Vol. 134, 184315-184322. ©2011 *American Institute of Physics.*)

also incorporated following arguments similar to Reference [199] and the instrument response function (and other broadening factors) is approximated by convolution with a Lorentzian of width 60 meV. The band origins are indicated in Figure 6.7(a) by the vertical dashed lines and that of $Cl^-{\cdot}CH_3I \rightarrow [Cl(b){\cdot}CH_3I(v)] + e^-$ is coincident with the experimental transition at 4.22 eV. However, the shoulder on the first transition in the simulation of Figure 6.7(a) (which corresponds to the $Cl^-{\cdot}CH_3I \rightarrow [Cl(a){\cdot}CH_3I(v)] + e^-$ origin is clearly different from the experimental spectrum displayed.

Many experiments have shown that the a band is absent in $I^-{\cdot}CH_3I$ detachment spectra.[3–5, 46, 109, 116, 121, 195] This has been attributed to excitation to the repulsive wall of the van der Waals stretching coordinate associated with the a state.[116] In this scenario, lifetime broadening spreads the oscillator strength over a wide range of eKEs. The potentials shown in Figure 6.6(a) illustrate the vertical excitation region for $I^-{\cdot}CH_3I$. For the purposes of discussion, this is defined in the following manner. The cluster anion potential along the van der Waals coordinate is calculated at the MP2 level and fit with a Morse function. The vertical lines in Figure 6.6(a) represent the full width half maximum (FWHM) of the ground vibrational wave function associated with this Morse potential. The horizontal lines in Figure 6.6(a) represent the van der Waals dissociation energy of neutral $I{\cdot}CH_3I$ in each state. For $I^-{\cdot}CH_3I$, most of the FC envelope corresponds to bound regions of the X and b state potentials but the a state continuum, in accordance with the contention of [116].

The detachment spectrum of the $Cl^-{\cdot}CH_3I$ cluster anion is simulated in Figure 6.7(b), assuming a similar situation and neglecting contributions from the a band. Further, the relative vibrational intensities of the experimental $I^-{\cdot}CH_3I$ spectrum of Figure 6.5(b) are incorporated rather than the $Cl^-{\cdot}CH_3I$ detachment Franck-Condon factors. These are estimated using the areas of a series of Lorentzian functions to the spectra of Figure 6.5(b) (dashed lines). Although the simulated transition positions of Figure 6.7(b) are consistent with the experimental spectrum, the intensities are not in good agreement. At low eKE (binding energies close to the photon energy), overestimation of the transition intensity might be rationalized using Wigner threshold law type arguments. However, the experimental 4.15 eV transition ($Cl^-{\cdot}CH_3I \rightarrow Cl(X){\cdot}CH_3I(\nu_3,\ v{=}1) + e^-$) intensity cannot be explained in this manner. Instead

there is considerable enhancement of this transition suggesting much greater vibrational excitation of the CH_3I moiety occurs in $Cl^-\cdot CH_3I$ detachment than in $I^-\cdot CH_3I$ detachment.

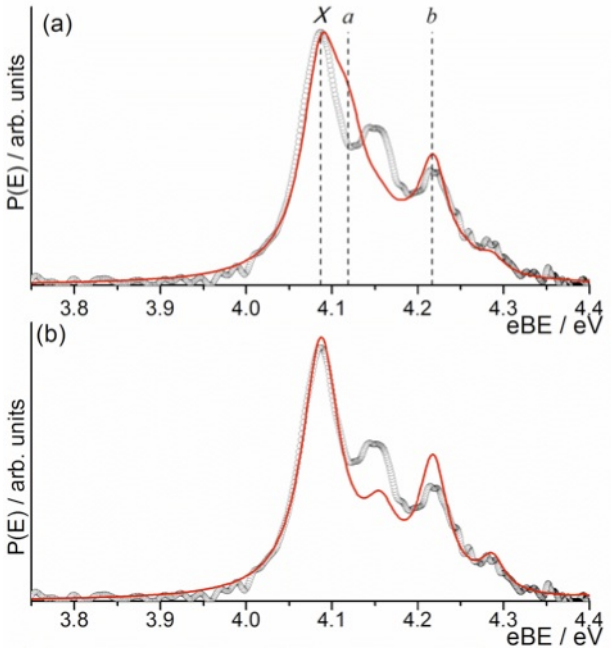

Figure 6.7: Electron binding energy domain spectra for 280 nm detachment from $Cl^-\cdot CH_3I$ (open circles). Simulations (solid lines) assuming detachment via (a) each of the X, a, and b states of $Cl\cdot CH_3I$, (b) neglecting the contribution from the a state. [See text for further details]. (Reproduced with permission from *The Journal of Chemical Physics*, Van Duzor *et al.*, May 2011, Vol. 134, 184315-184322. ©2011 *American Institute of Physics.*)

The above offers an explanation for the transition positions in the $Cl^-\cdot CH_3I$ spectra. However, the enhanced intensity of the 4.15 eV transition is not clear. Another phenomenon observed in $I^-\cdot CH_3I$ photoexcitation, autodetachment, may offer a rationalization. $I^-\cdot CH_3I$ excitation near the b band onset yields a transient $[I(b)\cdot CH_3I\cdot e^-]$ complex. Evidence for autodetachment from this complex (resulting from relaxation to the ground state of the I atom) is seen in enhancement of the X band vibrational structure and a drastic alteration of the X band PAD at excitation wavelengths near the b band onset.[5, 104, 109, 121, 195] Similar effects have been

reported for $I^-{\cdot}CH_3CN$ and $I^-{\cdot}H_2O$, as well as $I^-{\cdot}CH_3Cl$ and $I^-{\cdot}CH_3Br$, as seen in chapter 5.[111, 195]

Cluster photoexcitation to the X or b halogen atom states is illustrated in Figure 6.1 using pairs of CH_3I/CH_3I^- curves, offset by the X-b energy difference. From a Fermi Golden Rule viewpoint the relaxation (auto-detachment) probability is,

$$\propto \frac{4\pi^2}{h} \sum_f \mid \langle \psi_f \mid V \mid \psi_i \rangle \mid^2 \rho_f \tag{6.1}$$

ψ_i is the quasi-bound, $[A(b){\cdot}CH_3I{\cdot}e^-]$ complex and ψ_f represents $[A(X){\cdot}CH_3I]$ + free electron (A = I or Cl). ψ_f represents the density of available final states (essentially the continuum free electron states). Considering the $[A(b){\cdot}CH_3I{\cdot}e^-]$ complex to be analogous to a Rydberg state[23, 206], the coupling operator can be represented as the interaction of the excess and core electrons and the integral factored into electronic and vibrational components. The vibrational component will depend on the overlap between the initial and final vibrational wave functions.

The process associated with $I^-{\cdot}CH_3I$ excitation near the threshold of the b state results in electronic relaxation to the X state coupled with autodetachment (see section 5.4.4). Given the relatively large difference in energy between the X and b states in $I{\cdot}CH_3I$, the vibrational coupling term can be expected to be contribute minimally. Therefore, electronic relaxation to the ground level of the X state is favored. However, the electronic states associated with $Cl^-{\cdot}CH_3I$ excitation [Figure 6.1(b)] are much closer in energy. In fact, the calculated Cl X-b separation (in the neutral cluster at the cluster anion geometry) of 0.131 eV is similar to that of several CH_3I vibrational modes ($\nu_6 = 0.11$ eV, $\nu_2 = 0.16$ eV, $\nu_5 = 0.18$ eV) and more pertinently with double excitation of the ν_3 mode ($\nu_3 = 0.065$ eV). As a result, the overlap between

the upper and lower electronic state vibrational wave functions is much greater. Inclusion of the vibrational manifold associated with Cl(a)·CH_3I (excluded from Figure 6.1(b) for sake of clarity) should only enhance this possibility, as the X-a separation is calculated to be 0.032 eV. Given the propensity rules,[207] vibrational autodetachment may now make a significant contribution to the relaxation process, consequently enhancing the vibrational transition intensity in the photoelectron spectrum.

6.5 Summary

It is clear that the photodetachment spectra of Cl^-·CH_3I are strongly influenced by the proximity of the neutral and anionic states of CH_3I. The presence of states analogous to electron-molecule scattering resonances leads to altered photoelectron angular distributions (compared to free Cl^- detachment), fragmentation and non-Franck Condon vibrational intensities. Similar observations have been made for I^-·CH_3I detachment. However, I^-·CH_3I detachment spectra display two distinct vibronic bands, which are not easily distinguished in the Cl^-·CH_3I spectra. The extent of vibrational excitation is also much lower in the I^-·CH_3I detachment experiments.

Several possible explanations for the single photon features in the Cl^-·CH_3I photoelectron spectra have been considered. The 4.22 eV eBE transition in the photoelectron spectra is energetically consistent with the origin transition of the Cl^-·CH_3I $\rightarrow$ Cl(b)·CH_3I + e^- band. However, significant enhancement of the first vibrational transition in the Cl^-·CH_3I $\rightarrow$ Cl(X)·CH_3I + e^- band suggests the possibility that electronic relaxation of excited [Cl(b)·CH_3I·e^-] complexes via vibrational autodetachment might also be significant. This mechanism is consistent with the transitions

observed in the spectrum and the close proximity of the X and b states, but different to the electronic autodetachment observed subsequent to $I^-{\cdot}CH_3I$ excitation.

The similarity of the predicted $[Cl^-{\cdot}CH_3I \rightarrow Cl(b){\cdot}CH_3I + e^-]$ band origin and the $[Cl^-{\cdot}CH_3I \rightarrow Cl(X){\cdot}CH_3I(\nu_3,\ v{=}2) + e^-]$ transition frequency make it impossible to determine the extent of competition between these detachment pathways at the experimental resolution of these measurements. However, the possibility of different detachment mechanisms in otherwise similar cluster anions suggests potential for using these and related clusters as an experimental probe of the competition between electronic and vibrational autodetachment, and in particular coupling between the electronic and vibrational modes of freedom. Better instrumental resolution is required to determine the extent (if any) of channel suppression and whether vibrational modes other than ν_3 contribute to the photoelectron spectrum. Further measurements at the resolution recently achieved in References [19, 54] or by the SEVI technique [55] would give a better indication. High resolution evaluation of the electron kinetic energy evolution of the photoelectron angular distributions should also provide valuable complementary information on the origins of the features in the $Cl^-{\cdot}CH_3I$ photoelectron spectrum.

Chapter 7

$I^-\cdot(CH_3I)_2$ Photodetachment: The Influence of Dipole Bound States on Detachment and Cluster Fragmentation

7.1 Introduction

Cluster anions present appealing, microscopic models of anion and electron solvation interactions and dynamics.[1, 2, 208] The ease with which these charged species can be separated by mass spectrometric techniques allows for careful study of tailored solvent environments. Cluster anion photodetachment can provide a deeper understanding of a variety of phenomena, including electron localization within clusters, solvent perturbations of the anion as well as the neutral residue, solvent structure,

Portions of this chapter have been Reproduced with permission from *The Journal of Chemical Physics*, Van Duzor *et al.*, June 2011, Vol. 134, 214301-214308. ©2011 *American Institute of Physics.*

long range electron-molecule interactions and electron-molecule scattering. Particularly powerful in this regard are photoelectron imaging studies using a tunable photon source and photoelectron imaging detection scheme.[11] An especially attractive aspect of the imaging method is the ease with which photoelectron spectra and angular distributions may be recorded in a single experiment with essentially unitary electron collection efficiency.[99]

This chapter presents the results of photoelectron imaging experiments performed on the disolvated $I^-\cdot(CH_3I)_2$ cluster anion, paying particular attention to electron scattering related phenomena. Owing to a relatively large molecular dipole moment (1.62 D), strong polarizability and low-lying, dissociative excited state, the CH_3I molecule is a particularly efficient scatterer of low energy electrons, as evinced in previous chapters. Experimental and theoretical studies of the low-energy electron collisions with CH_3I have produced extensive evidence of negative ion resonances. Schramm and co-workers presented evidence of a vibrational Feshbach resonance (VFR) near the ν_3=1 vibrational level,[10] and a number of researchers have observed other features, including vibrational excitation and threshold cusps.[9, 10, 32, 102] The kinetics and energetics of dissociative electron attachment (DEA) to CH_3I have also been studied in detail.[6, 8, 106, 140, 154, 155, 157, 161, 162, 209]

Much attention has been paid, in this work and elsewhere, to monosolvated $X^-\cdot CH_3I$ (X=I, Br and Cl) clusters. Most notably, Johnson and co-workers have amassed a considerable body of work on the $I^-\cdot CH_3I$ cluster anion[3–5, 104, 116] as a probe of the S_N2 reaction coordinate, non-adiabatic electron-solvent interactions, and processes akin to dissociative electron attachment (DEA). Subsequent studies, including those discussed in the previous three chapters, have examined the effect

of electron-solvent interactions upon the photodetachment properties, in particular including variations in the PADs.[109, 121, 195]

Significantly less attention, however, has been extended to cluster anions containing multiple CH_3I molecules. This is surprising since the concerted influence of the long-range potentials of additional CH_3I molecules might be reasonably expected to produce interesting electron-solvent effects. The similarities and differences with respect to the $I^-{\cdot}CH_3I$ cluster anion should offer considerable insight into DEA processes, electron binding motifs and cluster geometry, as well as possible relevance to studies of SN2 reaction intermediates. Dessent et al.[194] have shown that the photoneutral action spectrum, following $I^-{\cdot}(CH_3I)_2$ photoexcitation, displays a below threshold absorption enhancement reminiscent of excitation to a dipole bound (DB) state of the cluster. The results presented here highlight the important role that the electron-dipole interaction plays in the dynamics of both fragmentation and electron ejection subsequent to photoexcitation. Furthermore, by tuning the photodetachment energy from below threshold to 4.8 eV, it is possible to follow the evolution of the photoejection dynamics and their relation to the arrangement of solvent molecules in the cluster anion.

7.2 Experimental Details

$I^-{\cdot}(CH_3I)_2$ cluster anions were produced by both of the ion generation techniques described in chapter two, electron impact ionization and pulsed discharge ionization. The gas sample used in this work was prepared according to the methods employed in generating the monomer cluster in chapters 4 and 5. Several photoelectron images were taken at each wavelength included in this study, a range extending

from 355 to 260 nm. The beam was gently focused by a 1 m lens, producing power densities ranging from 1.4-4.6$\times 10^7$ W cm^{-2}. Background noise and spurious electron impact events are accounted for through the recording and subtraction of an off-time signal for each experimental cycle as described in previous chapters. The data put forth in this chapter were extracted using the BASEX software of Dribinski et al.[92]

7.3 Data and Analysis

The $I^-\cdot(CH_3I)_2$ cluster anion was probed at photon energies from 3.49 eV (355 nm) to 4.77 eV (260 nm), at intervals ranging from 1 to 10 nm, as neccessary to elucidate spectroscopic features of interest. The resulting photoelectron images reveal the presence of multiple detachment channels, extensive cluster fragmentation, and interesting variations in the PADs with detachment laser energy. We subdivide the data presented here by photodetachment energy regime, beginning with features observed below the direct detachment threshold ($h\nu < 3.75$ eV), followed by the direct detachment regime ($h\nu > 3.75$ eV), including a close examination of the threshold region for production of excited I atoms.

7.3.1 Photoexcitation at $h\nu < 3.75$ eV

Excitation of the $I^-\cdot(CH_3I)_2$ cluster at photon energies between 3.49 and 3.75 eV produces 2 to 3 bands in the photoelectron spectrum. The evolution of these bands (I, II and X) with photon energy can be seen in Figure 7.1.

Table 7.1: Photoelectron peak positions (eKE_{max}) and accompanying angular asymmetry values (β) extracted from fragment signals I and II. (Reproduced with permission from *The Journal of Chemical Physics*, Van Duzor *et al.*, June 2011, Vol. 134, 214301-214308. ©2011 *American Institute of Physics.*)

	eKE_{max}/eV		β	
λ/nm	I	II	I	II
355	0.43	0.11	–	–
350	0.48	0.15	-0.76±0.03	-0.10±0.08
345	0.53	0.19	-0.84±0.08	0.01±0.06
340	0.59	0.23	-0.88±0.03	0.06±0.06
335	0.64	0.28	-0.86±0.08	0.05±0.04
330	0.70	0.34	-0.95±0.06	0.06±0.05

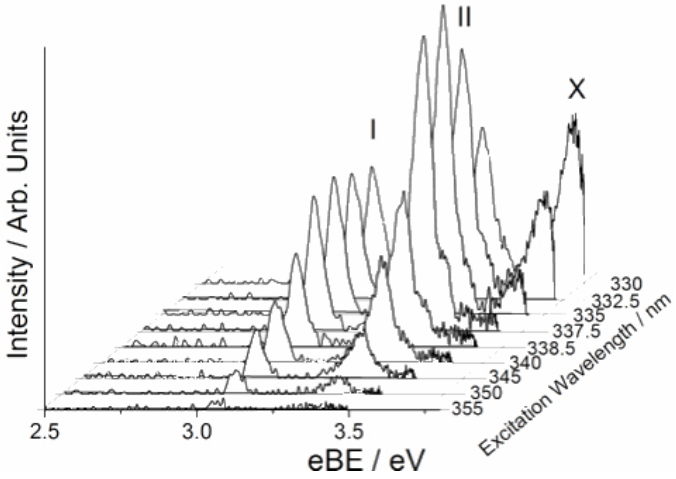

Figure 7.1: $I^-\cdot(CH_3I)_2$ photoelectron spectra (eBE domain) at a range of photodetachment wavelengths. Peaks labeled I and II correspond to product anion fragments, X is direct detachment from ($I^-\cdot(CH_3I)_2$). (Reproduced with permission from *The Journal of Chemical Physics*, Van Duzor *et al.*, June 2011, Vol. 134, 214301-214308. ©2011 *American Institute of Physics.*)

For direct comparison the spectra are displayed as a function of electron binding energy (eBE). Bands I (peak eBE = 3.06±0.01 eV) and II (peak eBE = 3.41±0.01) are assigned to photodetachment from I^- and $I^-\cdot CH_3I$ anions, produced via photoinduced

fragmentation, a process which will be discussed later. Peak electron kinetic energies (eKE_{max}), and photoelectron anisotropy parameters (β) for bands I and II are listed in Table 7.1.

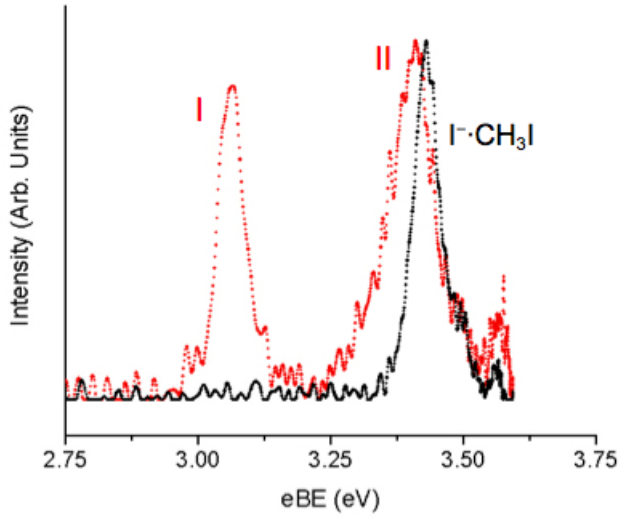

Figure 7.2: Comparison of an $I^-\cdot CH_3I$ (black) spectrum at 345 nm with a spectrum displaying bands I and II, produced by 345 nm excitation of $I^-\cdot(CH_3I)_2$. Both spectra are displayed in terms of eBE (see text for details).

We independently produce all three species, I^-, $I^-\cdot CH_3I$ and $I^-\cdot(CH_3I)_2$, in our ion source. Time-of-flight mass selection allows separate probing of I^-, and $I^-\cdot CH_3I$ for the purpose of comparison with the $I^-\cdot(CH_3I)_2$ photoexcitation results. The eBEs associated with bands I and II are essentially consistent with known values for photodetachment from I^-[118] (3.06 eV) and $I^-\cdot CH_3I$ (VDE = 3.42 eV)[116] respectively, although there is a slight redshift (approximately 20 meV) and broadening of band II, as illustrated in Figure 7.2

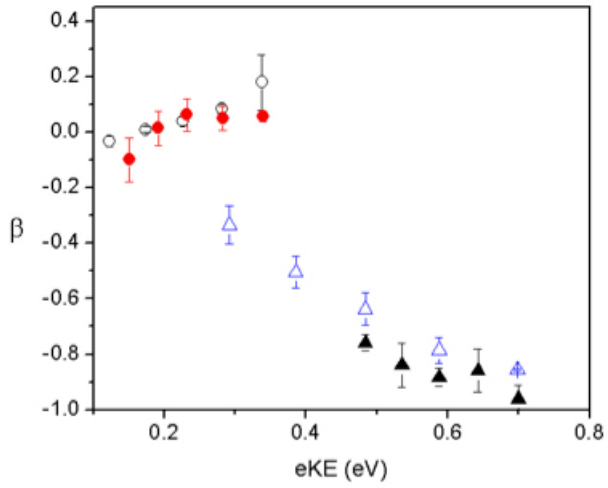

Figure 7.3: Photoelectron anisotropy parameter values (β) for I^- (filled triangles), $I^-{\cdot}CH_3I$ (filled circles), band I (open triangles) and band II (open circles).

Figure 7.3 presents β values for bands I and II (open symbols) and those of I^- and $I^-{\cdot}CH_3I$ (closed symbols).[195] Triangles correspond to I^- and band I, while circles correspond to $I^-{\cdot}CH_3I$ and band II. Each point in Figure 7.3 corresponds to a different detachment wavelength. The similarities strongly argue in favor of extensive fragmentation of the cluster anion upon excitation in this region, yielding I^- and $I^-{\cdot}CH_3I$ product anions.

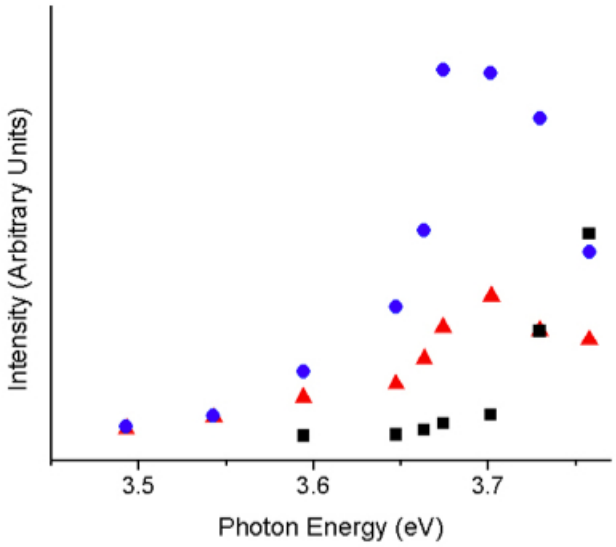

Figure 7.4: Integrated photoelectron intensity as a function of photon energy, band I (triangles), band II (circles) and X band (squares).

Figure 7.4 displays the integrated intensities of the bands corresponding to features I, II, and X as a function of photon energy. Data were obtained at fixed ion intensity and laser fluence. Differences in the photodetachment cross sections of the parent species have not been explicitly accounted for, so Figure 7.4 does not represent a measure of absolute fragmentation yield. However, a very good idea of the relative excitation energies required for fragmentation and direct detachment can be obtained. This approach also highlights that fragmentation occurs within a narrow excitation energy window. I^- and $I^- \cdot CH_3I$ fragment production appears to peak around 3.68 eV, in good agreement with the peak photoneutral absorption value observed by Dessent et al.[194]

7.3.2 Photoexcitation at $h\nu > 3.75$ eV

Throughout most of this work, as well as much of the general body of work on atomic halide centered cluster anions, discussion typically proceeds from the assumption of excess electron localization upon the atomic moiety. Direct photodetachment typically occurs through states which asymptotically correlate to low lying states of the free neutral, open shell halogen atom.

In chapters 4 and 5, atomic iodide centered cluster anions were considered in terms of the two iodine states, $^2P_{3/2}$ and $^2P_{1/2}$. The spectral positions of these two peaks will be shifted for cluster anion detachment as the I^- moiety is stabilized by ion-molecule interactions. Additionally, as demonstrated in chapter 6, the features correlating to the $^2P_{3/2}$ limit may be broadened, or even split as a result of the lifting of the degeneracy of the iodine atom $^2P_{3/2}$ state.[176] The splitting of the direct photodetachment bands observed in $I^-\cdot(CH_3I)_2$, much as in $I^-\cdot CH_3I$, are relatively unperturbed by comparison to free I^-. However, given the additional presence of $I^-\cdot CH_3I$ and I^- anion fragment bands, discussion is simplified by labeling these features I (I^- fragment), II ($I^-\cdot CH_3I$ fragment), X [direct detachment to $I(^2P_{3/2})\cdot(CH_3I)_2$] and A [direct detachment to $I(^2P_{1/2})\cdot(CH_3I)_2$].

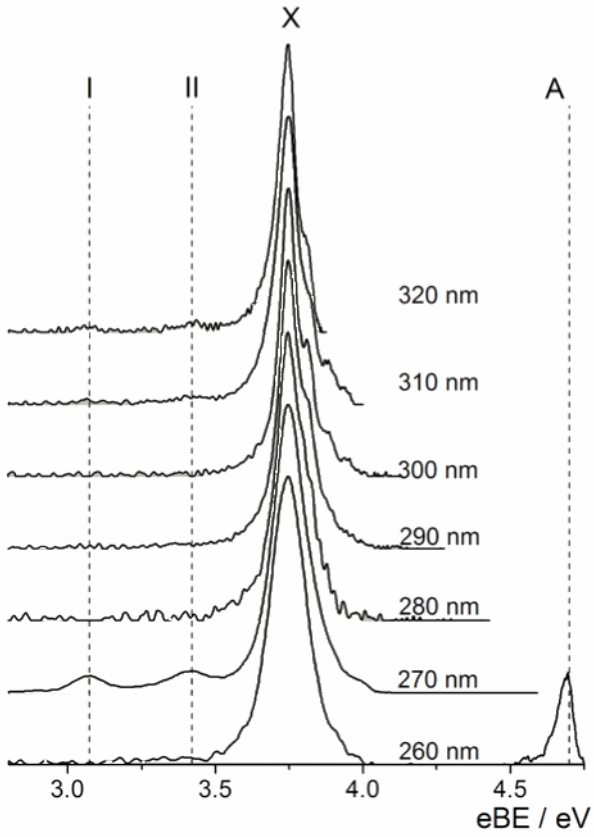

Figure 7.5: 320-260 nm $I^- \cdot (CH_3I)_2$ photoelectron spectra. Bands I and II are evident near threshold (320 nm spectrum) but absent from 310-280 nm, before reappearing in the 270 nm spectrum (see text for details). (Reproduced with permission from *The Journal of Chemical Physics*, Van Duzor *et al.*, June 2011, Vol. 134, 214301-214308. ©2011 *American Institute of Physics.*)

Vibrational structure is evident in several spectra, as seen to the higher binding energy side of the X band in Figure 7.5. This may arise due to some combination of differences in molecular geometry and non-adiabatic effects associated with temporary excited cluster anion states, as discussed in previous chapters.[104, 121, 176, 195] The spacing of the vibrational features is consistent with excitation of the CH_3I ν_3 mode.

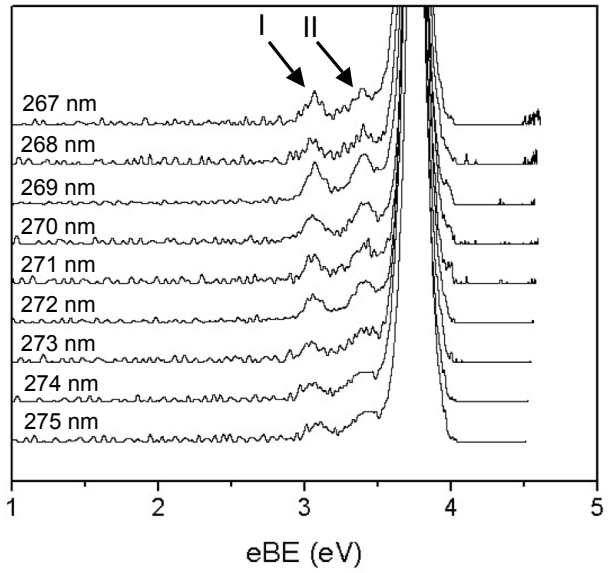

Figure 7.6: Detail of photoelectron spectra from 275-267 nm, displaying evidence of bands I and II. The major feature in the spectra (3.75 eV, eBE) is the X band.

As the photon energy is increased beyond 3.75 eV, bands I and II disappear. As shown in Figure 7.5, the X band dominates the photoelectron spectrum over this interval. Photodetachment from the $I^-\cdot(CH_3I)_2$ cluster anion at photon energies exceeding 4.71 eV produces two discrete bands, separated by 0.96 eV. An example (at 260 nm) is shown in Figure 7.5. The two bands (X and A), correlate asymptotically to the production of 2 CH_3I molecules and $I(^2P_{3/2})$ or $I(^2P_{1/2})$ atoms respectively as the neutral cluster framework dissociates upon electron loss. However, over a narrow wavelength range (275 - 265 nm) about the onset of the A band there is a reappearance of the two fragmentation features (I and II). This can be clearly seen in Figure 7.6. Figure 7.6 may be compared to the 270 nm spectrum in Figure 7.5 in order to gain a sense of the scale of the I and II band features in this photodetachment region. The reappearance of these features at 0.25 eV (photon energy) below the A band onset indicates dynamics similar to those in play below the X band threshold.

Table 7.2: Photoelectron peak positions (eKE) and accompanying angular asymmetry values (β) extracted from X band photodetachment. (Reproduced with permission from *The Journal of Chemical Physics*, Van Duzor *et al.*, June 2011, Vol. 134, 214301-214308. ©2011 *American Institute of Physics.*)

Band X			
eKE_{max}/eV	β	eKE_{max}/eV	β
0.01	-0.06±0.07	0.82	-0.03±0.08
0.13	0.15±0.05	0.85	-0.08±0.06
0.25	0.36±0.07	0.86	-0.09±0.07
0.39	0.43±0.07	0.88	-0.14±0.07
0.53	0.44±0.08	0.90	-0.11±0.07
0.68	0.36±0.06	0.92	-0.02±0.01
0.72	0.17±0.03	0.93	0.00±0.08
0.76	0.13±0.07	0.95	0.18±0.3
0.78	0.10±0.07	0.97	0.20±0.03
0.80	0.06±0.08	0.99	0.2±0.1
0.81	0.02±0.09	1.02	0.07±0.05

Table 7.2 records the anisotropy parameters (β) associated with the $I^-\cdot(CH_3I)_2$ X band eKE_{max}, which vary considerably over the photon energy range 3.75-4.77 eV. The evolution of the β parameter (filled triangles) shown in Figure 7.7 is different from both that of I^- (filled circles) and I^-CH_3I (open squares). At low eKE, the X channel photoelectron angular distribution is preferentially polarized parallel to the electric vector of the detachment laser. β initially becomes more positive, before rapidly decreasing after the maximum at eKE = 0.53 eV to a minimum near 4.63 eV. The onset of this decrease is coincident with the recurrence of fragment anion generation.

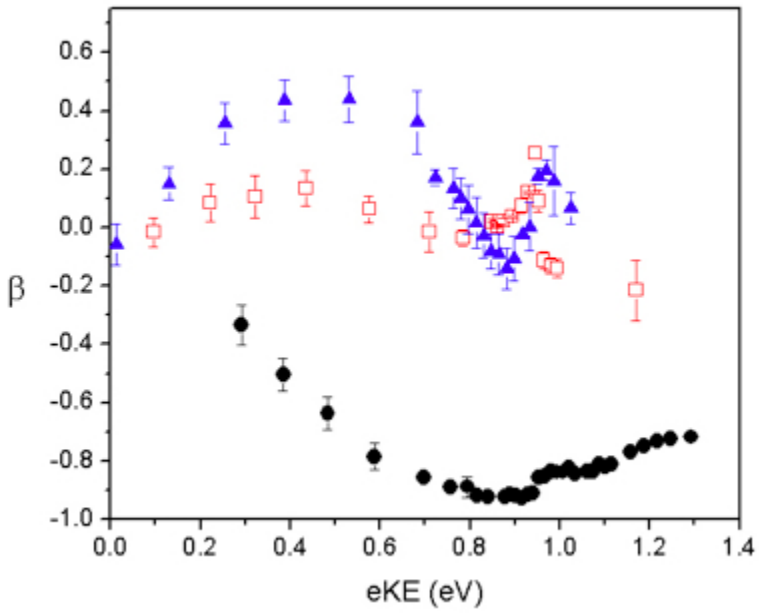

Figure 7.7: Photoelectron asymmetry parameter values (β) for $I^-\cdot(CH_3I)_2$ X band detachment (filled triangles), $I^-\cdot CH_3I$ (open squares) and I^- detachment (filled circles). (Reproduced with permission from *The Journal of Chemical Physics*, Van Duzor *et al.*, June 2011, Vol. 134, 214301-214308. ©2011 *American Institute of Physics.*)

As the photon wavelength decreases further, β begins to increase once more, peaking at a photon energy of 4.71 eV, roughly equivalent to the energy onset of the A band. The coincidence of this behavior with the opening of an excited state channel is strongly reminiscent of the observations of the series of mono-solvated atomic halide anions, including $I^-\cdot CH_3X$ (X=Cl, Br, I) presented in chapter 5.[109, 111, 121, 195] Most pertinently, the monosolvated $I^-\cdot CH_3I$ anisotropy parameters (Figure 7.7) show a similar peak.

7.4 Discussion

A number of studies have reported I^- production from $I^-{\cdot}CH_3I$ for a narrow range of photoexcitation energies beginning just below the direct detachment threshold.[3–5, 104, 109, 121, 195] Electron transfer into the CH_3I σ^* orbital produces a temporary, dissociative molecular anion state. Analogous behavior, driven by the exothermic nature of halide fragment anion production, is exhibited by most alkyl halide molecules in low energy electron scattering experiments.[10, 160] $I^-{\cdot}CH_3Br$ and $I^-{\cdot}CH_2Br_2$ provide further evidence for the photoinduced electron transfer mechanism yielding Br^-.[3] Additionally, as demonstrated in the previous chapter, $Cl^-{\cdot}CH_3I$ photoexcitation shows I^- production as the predominant fragmentation channel.[176]

7.4.1 Discussion: Photoexcitation at $h\nu < 3.75$ eV

The results presented here display two anionic fragmentation products from $I^-{\cdot}(CH_3I)_2$. Fragmentation appears to be most active 50-60 meV below the photodetachment threshold, significantly further than in the case of the monosolvated anions discussed in previous chapters. The subsequent disappearance of bands I and II (in Figures 7.1 and 7.4) as the photon energy exceeds the detachment threshold argues in favor of photoinduced fragmentation. The alternative, thermally induced fragmentation, should yield bands I and II at all excitation wavelengths. This is not observed. It should also be noted that the photofragment features in the spectra are far more intense than those observed for monosolvated anion photoexcitation.

Our assignment of bands I and II to I^- and $I^-{\cdot}CH_3I$ products is based on analyses of eBEs and photoelectron angular distributions. The redshift of band II

(Figure 7.2) must reflect the dynamics of the fragmentation process. By analogy to $I^- \cdot CH_3I$ photofragmentation the following mechanism is envisioned:

$$I^- \cdot C^{(a)}H_3I \cdots C^{(b)}H_3I \rightarrow I + H_3C^{(a)} \cdots I^- \cdots C^{(b)}H_3I \rightarrow I + C^{(a)}H_3 + I^- \cdot C^{(b)}H_3I$$

In this asymmetric, in-line arrangement, dissociative attachment via electron transfer to the first ($C^{(a)}H_3I$) molecule will produce an I^- ion whose impulsive recoil propels it toward the remaining ($C^{(b)}H_3I$) molecule. The nascent $I^- \cdot C^{(b)}H_3I$ will be vibrationally excited, at least in the van der Waals stretching mode. The II band red shift is the result of vibrational hotbands associated with the I^--C(b) coordinate. The asymmetric (head to tail) cluster geometry was posited by Dessent et al.[194] and the presence of a signal corresponding to production of a monosolvated anion ($I^- \cdot CH_3I$) is strongly supportive of this arrangement.

7.4.2 Role of the Dipole Bound State

Calculations were performed using Gaussian 03[202] at the MP2 level of theory. For H and C atoms, the aug-cc-pvdZ basis set was used and the aug-cc-pVDZ-pp[ECP][210] was used for I. These calculations predict a 4.63 D dipole moment for the $I \cdot CH_3I \cdot CH_3I$ cluster framework. This is well in excess of the $\sim$2 D required to support a DB state,[211–215] in which the electron occupies a spatially diffuse orbital largely external to the cluster framework.

There has been much discussion in the literature regarding the role of molecular and cluster dipole moments in mediating electron capture or photoinduced cluster

anion dissociation. A DB orbital will generally have largely s character, thus mixing with the low lying σ^* antibonding orbitals of the CH_3I molecules is symmetry allowed. In this manner, the DB state may act as a "doorway",[10, 216, 217] mediating dissociative attachment by coupling to the energetically similar valence anion potential. Examples of such behavior have been reported in both electron-molecule scattering[216–224] and cluster anion photoexcitation experiments.[41]

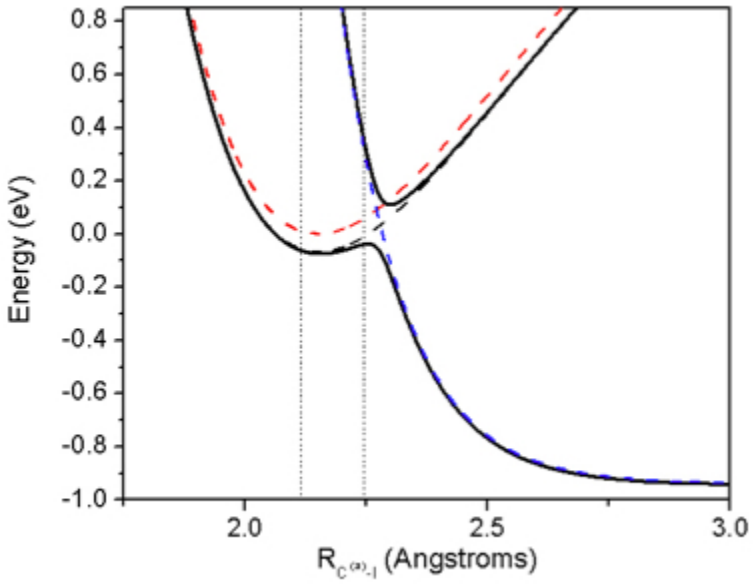

Figure 7.8: Calculated 1-D potential curves associated with the $C^{(a)}$-I stretching coordinate are displayed.6,9,12 $I{\cdot}C^{(a)}H_3I{\cdot}C^{(b)}H_3I$ framework. Dashed lines represent diabats for $I{\cdot}C^{(a)}H_3I{\cdot}C^{(b)}H_3I$ (red); $I{\cdot}C^{(a)}H_3I^{-}{\cdot}C^{(b)}H_3I$ (blue) and a dipole bound state (black). Solid black lines are the an adiabatic representation of the mixing of the DB and valence anion states. The dashed vertical lines represent the vertical excitation envelope (Reproduced with permission from *The Journal of Chemical Physics*, Van Duzor *et al.*, June 2011, Vol. 134, 214301-214308. ©2011 *American Institute of Physics.*).

Figure 7.8 schematically illustrates how the DB state influences the photofragmentation process for $I^{-}{\cdot}(CH_3I)_2$. Diabatic representations of potentials associated with the neutral framework and excess electron are shown as dashed lines.[6, 10, 32] The neutral ground state (which would be produced upon electron loss) is the red

curve. The diabatic representation for the molecular anion state produced upon electron transfer from the initial I^- ion is the dissociative, blue curve. The DB state diabat (black dashed curve) is represented by offsetting the neutral ground state by the dipole binding energy. Viewed from the perspective of a simple, 1-D avoided crossing model[221, 223] adiabatic potentials represented by the solid lines in Figure 7.8 can be drawn. Photoexcitation from the parent cluster anion into this region will therefore access predissociative states as a result of the coupling of the valence and DB anion states. In support of the role of the DB state mediated fragmentation, we note that our most intense fragment photoelectron peaks are found at $h\nu \approx 3.68$ eV. This is consistent with the local maximum (assigned to a DB state) in the absorption spectrum observed by Dessent et al.[194] Furthermore, the dipole moment associated with the head to tail structure is much greater than that of the monosolvated $I{\cdot}CH_3I$ framework, which is consistent with the enhanced fragmentation yield we observe.

Consideration of the origin of the I^- fragment is more complicated. Several scenarios can be envisioned.

1. Different cluster anion isomers ($IH_3C{\cdot}I^-{\cdot}CH_3I$ and $I^-{\cdot}CH_3I{\cdot}CH_3I$).

2. Scavenging of the excess electron by the neutral iodine atom.

3. Subsequent fragmentation of the monosolvated product,
   $I^-C^{(a)}H_3I{\cdot}C^{(b)}H_3I + h\nu \rightarrow I + C^{(a)}H_3 + I^-{\cdot}C^{(b)}H_3I^-$ $I + C^{(a)}H_3 + I^- + C^{(b)}H_3I$

4. Dissociative electron attachment to the terminal ($C^{(b)}H_3I$) molecule. $I^-C^{(a)}H_3I{\cdot}C^{(b)}H_3I$ $+ h\nu \rightarrow I + C^{(a)}H_3$ $I + C^{(b)}H_3 + I^-$

The first of these possibilities is effectively ruled out by *ab initio* calculation, which predicts a difference in vertical detachment energy for these isomers of 0.263 eV.

Only a single direct detachment band (at low excitation energies) is observed in our spectra. We assign this to the $I^-{\cdot}CH_3I{\cdot}CH_3I$ isomer for the reasons outlined above, and suggest that this is the only isomer produced under our ion source conditions. A third "non-linear" isomer was posited by Timerghazin et al.[225] for the similar $I^-{\cdot}(CH_3CN)_2$ cluster.[177] However, such a cluster geometry seems unlikely in this case, as production of the $I^-{\cdot}CH_3I$ anion fragment would be far less likely. The other scenarios are harder to evaluate, although comparison with the monosolvated anions studied in the previous three chapters suggest that (2) is at best a minor contributor.

Regarding (3) and (4), DB state mediated fragmentation arguments are in principle relevant to dissociation of either CH_3I moiety within the cluster anion. However, the strength of the coupling between the DB state and relevant dissociative anion states is important. The amplitude of the DB orbital is presumably smaller in the vicinity of the $C^{(b)}H_3I$ σ^* orbital and hence we might expect the mixing to be reduced in this case. This argument favors fragmentation of $C^{(a)}H_3I$ as the source of both monosolvated and (following subsequent atomic anion loss) unsolvated anionic products. However, neither these qualitative arguments, nor the experimental data are sufficient to make a definitive statement in this regard, particularly given the diffuse nature of the DB state wavefunction.

In the context of DB state mediated dissociation, product anion production at energies 200 meV below the first direct detachment band is interesting. Potential energy curves along the van der Waals $I{\cdots}C^{(a)}$ coordinate are shown in Figure 7.9 (Gaussian 03, same basis sets and level of theory as above).[202] The lower solid curve represents the variation of the cluster anion ground state along the van der Waals $I{\cdots}C^{(a)}$ coordinate, freezing all other degrees of freedom, while the dashed curve represents the variation in the potential associated with the neutral cluster framework.

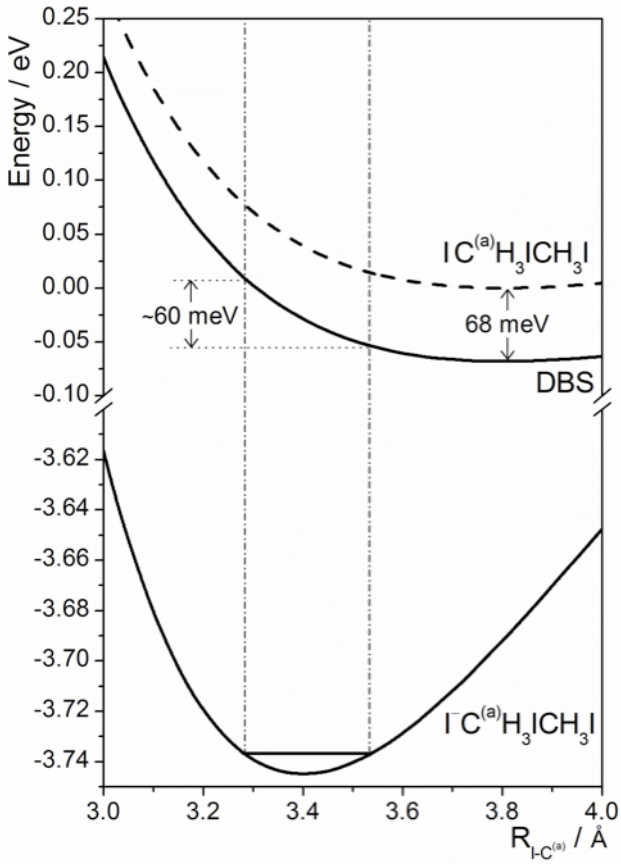

Figure 7.9: Calculated 1-D potential curves along the van der Waals I···$C^{(a)}$ coordinate. Lower solid line $I^{-}\cdot C^{(a)}H_3I\cdot CH_3I$, upper dashed line $I\cdot C^{(a)}H_3I\cdot CH_3I$, upper solid line $[I\cdot C^{(a)}H_3I\cdot CH_3I]^{-}$ DB state. Dash-dotted lines estimate the extent of the vertical excitation envelope. (Reproduced with permission from *The Journal of Chemical Physics*, Van Duzor *et al.*, June 2011, Vol. 134, 214301-214308. ©2011 *American Institute of Physics.*)

The DB state (upper solid curve) is represented by offsetting the neutral potential to match the location of the cluster anion absorption maximum. The vertical excitation region (dash-dotted lines), estimates a 60 meV excitation window, in the limit that the DB state is long lived. However, within the DB state mediated dissociation mechanism, lifetime broadening of the excited state is important. Although an accurate estimate of the lifetime cannot be obtained from our measurements, the photon energy range for which fragmentation is observed suggests strong coupling of the DB state and the valence orbital and a fairly short lifetime for the DB anion.

7.4.3 Discussion: Photoexcitation at $h\nu > 3.75$ eV

The reappearance of fragmentation products at excitation energies 250 meV below the A transition threshold is also consistent with the same DB state mediated mechanism. Here the relevant dipole moment is associated with a cluster framework incorporating an excited I atom, $[I(^2P_{1/2})\cdot CH_3I\cdot CH_3I]$. However, the dynamics associated with this temporary excited state are more complex than for excitation below the X channel threshold. An additional decay pathway arises, $[I(^2P_{1/2})\cdot CH_3I\cdot CH_3I]^- \rightarrow [I(^2P_{3/2})\cdot CH_3I\cdot CH_3I] + e^-$ which will compete with fragmentation. This electronic autodetachment process might be expected to further reduce the lifetime of the DB state, which is consistent with the wider range of photon energies producing fragmentation products below the A channel threshold. It has been demonstrated in chapter 5 and elsewhere that such autodetachment processes are common in mono-solvated I^- cluster anions.[109, 111, 121, 195] They have a profound effect on the PAD, which is clearly seen in Figure 7.7. The anisotropy parameters associated with the $I^-\cdot CH_3I\cdot CH_3I$ X transition (filled triangles) and the analogous transition from $I^-\cdot CH_3I$ (open squares) both show a sharp peak in the anisotropy parameter values at eKEs close to the neutral I atom spin orbit splitting. This is caused by interference between auto- and directly detached (but energetically equivalent) electrons, and gives a graphic illustration of the presence of an electronic autodetachment channel.

Interestingly, at all photon energies below the A channel threshold, there is a stronger parallel polarization of the PAD (more positive β) for the disolvated anion. Furthermore, both cluster anion PADs deviate markedly from that of the free I^- anion. In the case of $I^-\cdot CH_3I$ detachment this has been discussed in terms of the influence of the temporary anion (CH_3I^-) state produced upon charge transfer to the molecular moiety.[121, 195] It would seem safe to assume a similar role for the

$I\cdot[C^{(a)}H_3I^-]\cdot C^{(b)}H_3I$ state in the excited disolvated anions. At this stage, we are not in a position to offer a quantitative explanation of difference between the mono- and disolvated anion PADs. One simplistic viewpoint might be that the presence of two methyl iodide molecules enhances the scattering cross section. Another possibility may be that the anion state associated with production of the $I^-\cdot CH_3I$ is shifted lower in energy by 390 meV relative to the I^- fragment channel. This solvation shift may effectively lower the energy of the σ^* orbital associated with $C^{(a)}H_3I$. The increase in the dipole moment may also be significant in enhancing the charge transfer cross section.

7.5 Summary

Long range electron-solvent interactions, such as the dipole-binding of the electron, have a dramatic effect upon the photoexcitation dynamics of the $I^-\cdot(CH_3I)_2$ cluster anion. Excitation below the direct detachment threshold produces extensive fragmentation of the cluster, peaking at a photon energy of 3.68 eV, consistent with the excitation of a DB state. These dynamics can be explained invoking a DB state "doorway" model, wherein coupling of the DB state to nearby valence anion states brings about cleavage of a covalent C-I bond. The strongly repulsive nature of the valence anion states causes fragmentation, with the range of excitation energies producing product ions reflecting predissociative lifetime broadening of the DB state.

The production of stable $I^-\cdot CH_3I$ cluster anions subsequent to exciation strongly supports the prior assertion of Dessent et al.[194] that the $I^-\cdot(CH_3I)_2$ cluster anion geometry corresponds to a head to tail arrangement of CH_3I groups with a linear I·C-I···C-I backbone. Fragmentation producing similar products is also observed in

the vicinity of the A band threshold. This is consistent with a DB state mediated mechanism, supported by a neutral framework which incorporates an excited I atom. However, excitation into the region is accompanied by abrupt changes in the PAD of the X band. This is attributable to a competing electronic autodetachment pathway due to relaxation of the spin-orbit excited I atom via electronic energy transfer to the excess electron.

Chapter 8

Conclusion

The central goal of this dissertation has been to examine the effectiveness of cluster anion photodetachment as a probe of electron-molecule interactions. The results presented herein comprise the most expansive study of the influence of electron-solvent interactions upon the PAD that has been performed to date. Over the course of the preceding chapters, the results of photodetachment studies of a series of methyl halide containing cluster anions have been presented. The cluster anions themselves display many physical similarities. Among them is the electron binding motif; in all cases presented here the excess electron is localized upon the atomic halide moiety. The cluster solvation energies were also found to be quite consistent throughout, ranging from 35-46 meV per monomer added, and geometric distortions of the neutral molecules in the clusters are all comparably modest ($\sim$ 1.5%). These observations are particularly true of the iodide centered clusters.

Despite the above stated similarities of the clusters, their photoelectron angular distributions show a range of behaviors at low energy. Clusters containing CH_3I molecules displayed marked deviation from PADs produced in unsolvated I^- photodetachment. The spectra of these clusters also display enhanced vibrational structure

relative to Franck-Condon predictions and similar clusters [$I^-\cdot CH_3X$ (X=Cl, Br)]. Clusters not containing CH_3I displayed photodetachment behavior relatively consistent with that of bare I^- at low detachment energies. The $I^-\cdot CH_3Cl$ cluster displayed very little deviation from anisotropy values expected for bare I^- at comparable eKEs, despite possessing the largest dipole moment of any of the monomer clusters studied here. These observations support the assertion that the effects of electron-CH_3I scattering resonances are felt in photodetachment from CH_3I containing cluster anions. The results clearly show that the low lying σ^* orbital of the CH_3I molecule has an important role in mediating the dynamics of the electron-CH_3I interaction.

Effects mediated by the physical electron-dipole interaction were observed as well. Energies around eKE = 0.9 eV fall near the opening of the excited photodetachment channel in the iodide centered clusters. In the four clusters of this type studied here, a sharp peak in the evolution of the anisotropy parameter β with eKE was observed in this region. By analogy to spin orbit autodetachment from atomic Rydberg states, relaxation of the core to the $^2P_{3/2}$ ground state is allowed facilitated by coupling to the electronic continuum, resulting in autodetachment at an eKE equivalent to that of direct detachment *via* the electronic ground state. Similar behavior was also observed upon photoexcitation within the vibrational manifold of the electronically excited state. The role of vibronic coupling in the $Cl^-\cdot CH_3I$ cluster anion, wherein the vibrational spacing is on the order of the electronic state splitting, remains a point of experimental interest. These results highlight the "tunability" of the cluster anion photodetachment method; a tunable laser provides photoelectrons of well defined eKE (photon energy), while flexible ion generation and mass selection techniques allow for production and isolated study of clusters of varying size, composition and electronic structure.

A further example of this strength is demonstrated in the study of $I^-\cdot(CH_3I)_2$ photodetachment. The asymmetric arrangement of the CH_3I molecules within the cluster gives rise to a substantial dipole moment, capable of physically binding an electron outside the cluster framework. This dipole bound state couples to the nearby σ^* orbital of the CH_3I molecule, producing intense $I^-\cdot CH_3I$ and I^- fragment signals. This result presents a dramatic example of the influence that cluster geometry and the resulting long range electron-neutral interactions can have upon the chemistry of a particular system.

Cluster anion photodetachment spectroscopy, coupled with velocity-map imaging, allows for observation of chemical interactions at a fundamental level. Information regarding electronic structure, intracluster "solvent-solute" interactions, and electron-molecule scattering interactions are readily obtainable. Broadly applicable as well as sensitive, photoelectron imaging of cluster anions offers a robust probe of the interactions underlying simple chemical systems.

8.1 Future Directions

The work described in this dissertation, having demonstrated the efficacy of cluster anion photodetachment as a probe of electron-molecule interactions, provides a point of departure for further studies. Of particular interest will be examination of electron correlation interactions in atomic and cluster anions.

In the Cooper-Zare model of photoelectron angular distributions, the anisotropy parameter β is defined by the cross sections and phase shifts of the partial wave components of the free electron wave function (section 2.2.1). For photodetachment

into a central potential, this model reproduces experimental observations quite well. In the presence of resonances, however, electron-correlation and other anisotropic interactions allow for transfer of angular momentum between the departing electron and the residual core.[44, 226, 227]

An interesting example of such phenomena is photoionization or photodetachment from an atomic s-orbital. In the Cooper-Zare description, the resulting PAD should be that of a pure p-wave, displaying $\beta = 2$ at all eKE. However, in the presence of strong electron correlation effects, as observed in the vicinity of autodetachment resonances, deviations from this behavior may be observable.[228] This has been experimentally demonstrated in the subshell ionization of Xe and Kr in the vicinity of spin-orbit channel openings.[229] Negative ions are excellent candidates for the study of such effects, as electron-correlation effects are more dominant due to the weaker interaction with the residual core subsequent to photodetachment.[14]

8.1.1 Photodetachment from Cu^- and $Cu^-\cdot X$

The recent addition of the pulsed discharge ion source to our instrument has greatly facilitated production of a wide variety of anions in robust, quantities. This source has also opened the possibility of using solid and metal samples for ion production, expanding the array of possible clusters for study. The Cu^- anion can be produced in our pulsed discharge ion source using a copper cathode in place of a stainless steel needle.[48, 49] The ground state of the Cu^- anion is $^1S_0$, with the extra electron occupying the 4s orbital. Single photon photodetachment from this anion, in the electric dipole approximation, should produce a p-wave electron.[230] Evidence of any spin-orbit channel-coupling in the vicinity of the $^2D_{5/2}$ and $^2D_{3/2}$

channel openings should appear as deviations from $\beta = 2$, as observed in Xe and Kr above. Measurements of the PAD of this anion have not previously displayed deviation from expected behavior, although PAD measurements very near the $^2S_{1/2}$ threshold, where such effects are most likely to occur, have not been performed.[101]

The results presented in chapter 5, in particular, suggest that the presence of a physical dipole enhances such autodetachment features. Clustering of the Cu^- anion with a strongly dipolar solvent molecule could provide a further insight into phenomena such as those PAD peaks encountered upon excitation near threshold in chapters 5 and 7. Once again, only anisotropic interactions, such as spin-orbit autodetachment or resonances, should be expected to manifest in the PAD. Comparison of this data with the measured cross sections could provide valuable information with respect to the energy scaling (and thus lifetimes) of these autodetachment features in β, and alteration of the cluster environment could offer insight into the role of anisotropic electron-cluster interactions in the process. Additionally, the presence of only a single outgoing electron wave should greatly simplify comparison of the data to theoretical treatments of the problem.

In the case of a molecule, such as CH_3I, in which low energy resonances are present, these could be investigated as well. Photodetachment imaging of the $Cu^-{\cdot}CH_3I$ cluster may provide a clearer picture of the low energy scattering observed in the PADs of CH_3I-containing clusters in presented in chapters 4-7. The $Cu^-{\cdot}CH_3I$ PADs would be expected to manifest no evidence of "background" (non-resonance) scattering, highlighting only the presence of resonance scattering in the PAD. Furthermore, the low energy resonance scattering and electron attachment mechanisms proposed to be active in $X^-{\cdot}CH_3I$ photodetachment can be expected to display sensitivity to the angular momentum of the incident electron. Zero-energy and vibrational Feshbach

resonances favor low-to-zero angular momentum electrons, as the lack of a centrifugal barrier allows for a close approach of the electron to the molecular framework. Shape resonances, on the other hand, require the centrifugal interaction to be present in order to capture the electron. Additionally, symmetry considerations are important. For instance, the π^* shape resonance accessible upon $Cu^- \cdot CH_3CN$ photodetachment (VAE=2.9 eV) may be more likely to produce scattering than the σ^* resonance in CH_3I.[231] In producing electrons of a single angular momentum, the Cu^- anion presents another selective probe of the scattering dynamics in cluster anion systems.

8.1.2 Time-Resolved Photoelectron Imaging

Another means of better understanding the dynamics of electron-cluster interactions is to observe them directly in the time domain. Time resolved photoelectron spectroscopy of dissociative electron attachment could offer great insight into a very fundamental chemical process. However, probing such a system requires an initiation event shorter than the timescale of molecular motion. Coulombic repulsion makes the generation of low-energy, ultra-short electron pulses very challenging. Femtosecond photo-initiation of this chemistry within the cluster environment, however, may be feasible.

Photon-initiated dissociative electron attachment within clusters has been demonstrated in this work and elsewhere.[3–5, 41, 104] Dissociative electron-transfer bands within cluster anions observed here are usually narrow ($\sim$100 meV). It is therefore useful to employ the tuneable, ns laser in characterizing these features. In addition to tuning the wavelength of the laser, the makeup of the cluster must also be "tuned"

such that the energetics of photoexcitation and electron capture by the solvent correspond to photon energies available to the fs laser. In this sense, the time-resolved experiments build directly upon the present work.

Time-resolved photoelectron imaging of the $I^-\cdot(CH_3I)_2$ cluster anion at pump laser energies near 270 nm is an intriguing possibility. Displayed in Figure 7.6, two cluster fragmentation channels were observable, corresponding to production of I^- (band I) and $I^-\cdot CH_3I$ (band II). Pump-probe photodetachment spectroscopy of these fragments could produce valuable information regarding the evolution in time (and energy) of fragments along the dissociative diabats, the time scale upon which the respective fragments are formed and the lifetime of the dipole bound state with respect to coupling into the fragment channels. Such information would directly address a number of presently unresolved details of the $I^-\cdot(CH_3I)_2$ system.

Appendix A

The Inverse Abel Transformation

Being of central importance to the photoelectron imaging method, the inverse Abel transformation and it's role in the extraction of data will be discussed here briefly. As stated above, the raw photoelectron image represents a two-dimensional projection of the three-dimensional photoelectron Newton-sphere. The three-dimensional sphere can be described in terms of y,z and an angle θ, producing the function $f(y, z, \theta) = f(r, \theta)$. Due to the cylindrical symmetry of the photoelectron distribution about the laser polarization ($z-$axis), however, the distribution is independent of θ. The projection of this function on a given line L of distance R can then be described by the line integral

$$f_{\mathrm{L}}(\mathrm{R}, \theta) = \int_{-\infty}^{\infty} f(y, z)\delta(y\cos\theta + \sin\theta - \mathrm{R})\mathrm{d}y\mathrm{d}z \tag{A.1}$$

As the angle θ may be defined arbitrarily, it is set to $\theta = 0$. With R= y, the Equation A.1 further simplifies,

$$f_{\mathrm{L}}(y) = \int_{-\infty}^{\infty} f(r)\delta(y - \mathrm{R})\mathrm{d}y\mathrm{d}z = 2\int_{r=y}^{\infty} f(r)\mathrm{d}z \tag{A.2}$$

Equation A.2 may be altrernatively expressed in the form of Equation A.3 below, which is the Abel integral or Able transform of $f(r)$:

$$f_{\mathrm{L}}(y) = \int_{r}^{\infty} \frac{f(r) r \mathrm{d}r}{\sqrt{r^2 - y^2}} \tag{A.3}$$

Equation A.3 expresses the function $f_{\mathrm{L}}(y)$, the experimentally observed projection in terms of $f(r)$, the three-dimensional photoelectron distribution. The inverse Abel transform, equation A.4, therefore expresses $f(r)$ in terms of $f_{\mathrm{L}}(y)$.

$$f(r) = -\frac{1}{\pi} \frac{\partial}{\partial r} \int_{r}^{\infty} \frac{f_{\mathrm{L}}(y) r \mathrm{d}y}{y\sqrt{y^2 - r^2}} \tag{A.4}$$

There are many implementations of this method, the most common of which is to take the inverse Hankel transform of the Fourier transform of each individual line of the image, the so-called Fourier-Hankel method [232]. This method, while computationally facile, does have drawbacks. The most notable of these is the amplification of noise within the image proportional to $1/r$ from the symmetry axis.

Methods employed in this laboratory include the recursive method of Hansen and Law[112] and the basis set expansion (BASEX) method of Dribinski et al.[92] The BASEX method avoids some of the noise-related problems associated with the Fourier-Hankel method. In particular, noise in the image can present discontinuities. The inverse Hankel transform requires a continuous, "smooth" function. The BASEX method generates a smooth representation of the momentum space distribution through the Abel transformation of a gaussian-like basis set representation of the

image space. In this manner, BASEX avoids problems associated with sharp features on the order of single pixels.[233]

References

[1] A. Sanov and W. Carl Lineberger, Physical Chemistry Chemical Physics **6**, 2018 (2004).

[2] A. W. Castleman and K. H. Bowen, The Journal of Physical Chemistry **100**, 12911 (1996).

[3] D. M. Cyr, G. A. Bishea, M. G. Scarton, and M. A. Johnson, The Journal of Chemical Physics **97**, 5911 (1992).

[4] D. M. Cyr, M. G. Scarton, and M. A. Johnson, The Journal of Chemical Physics **99**, 4869 (1993).

[5] D. M. Cyr, C. G. Bailey, D. Serxner, M. G. Scarton, and M. A. Johnson, The Journal of Chemical Physics **101**, 10507 (1994).

[6] R. S. Wilde, G. A. Gallup, and I. I. Fabrikant, Journal of Physics B: Atomic, Molecular and Optical Physics **33**, 5479 (2000).

[7] C. Kryzysztofowicz, A M Szmytkowski, Journal of Physics B: Atomic, Molecular and Optical Physics **28**, 1593 (1995).

[8] N. Jones, D. Field, and J.-P. Ziesel, International Journal of Mass Spectrometry **277**, 91 (2008).

[9] F. I. I. Gallup, Gordon A., Physical Review A **75**, 32719 (2007).

[10] A. Schramm et al., Journal of Physics B: Atomic, Molecular and Optical Physics **32**, 2153 (1999).

[11] A. T. J. B. Eppink and D. H. Parker, Review of Scientific Instruments **68**, 3477 (1997).

[12] D. H. Parker and A. T. J. B. Eppink, The Journal of Chemical Physics **107**, 2357 (1997).

[13] R. D. Mead, U. Hefter, P. A. Schulz, and W. C. Lineberger, The Journal of Chemical Physics **82**, 1723 (1985).

[14] V. K. Ivanov, Journal of Physics B: Atomic, Molecular and Optical Physics **32**, R67 (1999).

[15] P. F. Bernath, *Spectra of Atoms and Molecules*, Oxford University Press, 2nd edition, 2005.

[16] W. Demtroder, *Laser Spectroscopy: Basic Concepts and Instrumentation*, Springer, 3 edition, 2003.

[17] K. J. Reed, A. H. Zimmerman, H. C. Andersen, and J. I. Brauman, The Journal of Chemical Physics **64**, 1368 (1976).

[18] F. A. Akin, L. K. Schirra, and A. Sanov, The Journal of Physical Chemistry A **110**, 8031 (2006).

[19] M. Van Duzor, Matthew Duzor et al., The Journal of Chemical Physics **133**, 174311 (2010).

[20] R. Mabbs et al., Physical Review A **82**, 011401 (2010).

[21] L. Velarde, T. Habteyes, E. R. Grumbling, K. Pichugin, and A. Sanov, The Journal of Chemical Physics **127**, 084302 (2007).

[22] P. K. Ghosh, *Introduction to Photoelectron Spectroscopy*, volume 67 of *Chemical Analysis*, Wiley-Interscience, 1st edition, 1983.

[23] J. Berkowitz, *Photoabsorption, Photoionization, and Photoelectron Spectroscopy*, Academic Press, 1st edition, 1979.

[24] H. Bethe, *Handbuch der Physik*, volume 24, page 483, Springer, 1933.

[25] J. Cooper and R. N. Zare, *Atomic Collision Processes*, volume XI-C, page 317, Gordon and Breach, 1968.

[26] G. Breit and H. A. Bethe, Physical Review **93**, 888 (1954).

[27] W. R. Johnson, *Atomic Structure Theory: Lectures on Atomic Physics*, Springer, 1st edition, 2007.

[28] J. L. Hall and M. W. Siegel, The Journal of Chemical Physics **48**, 943 (1968).

[29] D. Hanstorp, C. Bengtsson, and D. J. Larson, Physical Review A **40**, 670 (1989).

[30] G. J. Schulz, Reviews of Modern Physics **45**, 378 (1973).

[31] G. J. Schulz, Reviews of Modern Physics **45**, 423 (1973).

[32] H. Hotop, M.-W. Rul, and I. I. Fabrikant, Physica Scripta **T110**, 22 (2004).

[33] J. P. Gauyacq and A. Herzenberg, Physical Review A **25**, 2959 (1982).

[34] G. Knoth, M. Gote, M. Rädle, K. Jung, and H. Ehrhardt, Physical Review Letters **62**, 1735 (1989).

[35] U. Fano, Physical Review **124**, 1866 (1961).

[36] J. Hasted and D. Mathur, *Electron Molecule Interactions and Their Applications*, volume 1, chapter 5, pages 424–477, Academic Press, 1st edition, 1984.

[37] J. R. Taylor, *Scattering Theory: The Quantum Theory of Nonrelativistic Collisions*, Wiley, 1st edition, 1972.

[38] U. Fano and J. W. Cooper, Reviews of Modern Physics **40**, 441 (1968).

[39] S. Tauro and K. Liu, Journal of Physics B: Atomic, Molecular and Optical Physics **41**, 225001 (2008).

[40] R. L. Jackson, A. H. Zimmerman, and J. I. Brauman, The Journal of Chemical Physics **71**, 2088 (1979).

[41] C. Dessent, J. Kim, and M. Johnson, Faraday Discussions **115**, 395 (2000).

[42] C. G. Bailey, D. J. Lavrich, D. Serxner, and M. A. Johnson, The Journal of Chemical Physics **105**, 1807 (1996).

[43] J. Schiedt and R. Weinkauf, The Journal of Chemical Physics **110**, 304 (1999).

[44] U. Fano and D. Dill, Physical Review A **6**, 185 (1972).

[45] A. N. Grum-Grzhimailo, S. Fritzsche, P. O'Keeffe, and M. Meyer, Journal of Physics B: Atomic, Molecular and Optical Physics **38**, 2545 (2005).

[46] R. Mabbs, E. Surber, and A. Sanov, The Journal of Chemical Physics **122**, 054308 (2005).

[47] P. Kruit and F. H. Read, Journal of Physics E: Scientific Instruments **16**, 313 (1983).

[48] C.-Y. Cha, G. Gantefor, and W. Eberhardt, Review of Scientific Instruments **63**, 5661 (1992).

[49] H. Handschuh, G. Gantefor, and W. Eberhardt, Review of Scientific Instruments **66**, 3838 (1995).

[50] R. Giniger, T. Hippler, S. Ronen, and O. Cheshnovsky, Review of Scientific Instruments **72**, 2543 (2001).

[51] C. Domesle et al., Physical Review A **82**, 033402 (2010).

[52] D. W. Chandler, J. W. T. Jr., M. H. Janssen, and D. H. Parker, Chemical Physics Letters **156**, 151 (1989).

[53] D. H. Parker, *Photoionization and Photodetachment*, volume I, chapter 1, pages 3–46, World Scientific Publishing Co., 1st edition, 2000.

[54] S. J. Cavanagh et al., Physical Review A **76**, 052708 (2007).

[55] D. M. Neumark, The Journal of Physical Chemistry A **112**, 13287 (2008).

[56] W. C. Wiley and I. H. McLaren, Review of Scientific Instruments **26**, 1150 (1955).

[57] J. Simons, *Photoionization and Photodetachment*, chapter 17, pages 958–1010, World Scientific Publishing Co., 1st edition, 2000.

[58] E. Illenberger, *Photoionization and Photodetachment*, chapter 19, pages 1063–1160, World Scientific Publishing Co., 1st edition, 2000.

[59] J. Simons, The Journal of Physical Chemistry A **112**, 6401 (2008).

[60] F. Bloch and N. E. Bradbury, Physical Review **48**, 689 (1935).

[61] D. Spence and G. J. Schulz, Physical Review A **5**, 724 (1972).

[62] C. E. Klots and R. N. Compton, The Journal of Chemical Physics **67**, 1779 (1977).

[63] C. E. Klots and R. N. Compton, The Journal of Chemical Physics **69**, 1636 (1978).

[64] A. Stamatovic, K. Leiter, W. Ritter, K. Stephan, and T. D. Mark, The Journal of Chemical Physics **83**, 2942 (1985).

[65] H. Shimamori and R. W. Fessenden, The Journal of Chemical Physics **74**, 453 (1981).

[66] A. Kantrowitz and J. Grey, Review of Scientific Instruments **22**, 328 (1951).

[67] G. Kistiakowsky and W. P. Slichter, Review of Scientific Instruments **22**, 333 (1951).

[68] R. E. Smalley, L. Wharton, and D. H. Levy, Accounts of Chemical Research **10**, 139 (1977).

[69] J. Arno and J. Bevan, *Jet Spectroscopy and Molecular Dynamics*, chapter 2, pages 29–73, Blackie Academic Professional, 1 edition, 1995.

[70] T. A. Milne, E. Vandegrift, and F. T. Greene, The Journal of Chemical Physics **52**, 1552 (1970).

[71] R. Gordon, Y. Lee, and D. R. Herschbach, The Journal of Chemical Physics **54**, 2393 (1971).

[72] O. Hagena and W. Obert, The Journal of Chemical Physics **56**, 1793 (1972).

[73] D. Golomb, R. Good, and R. Brown, The Journal of Chemical Physics **52**, 1545 (1970).

[74] H. Godfried and I. F. Silvera, Physical Review A **27**, 3019 (1983).

[75] O. H. Crawford and B. J. D. Koch, The Journal of Chemical Physics **60**, 4512 (1974).

[76] J. P. Gauyacq and A. Herzenberg, Journal of Physics B: Atomic and Molecular Physics **17**, 1155 (1984).

[77] K. H. Bowen, G. W. Liesegang, B. S. Sanders, and D. R. Herschbach, The Journal of Physical Chemistry **87**, 557 (1983).

[78] A. Schramm et al., Physical Review Letters **81**, 778 (1998).

[79] H. Haberland, C. Ludewigt, H.-G. Schindler, and D. R. Worsnop, The Journal of Chemical Physics **81**, 3742 (1984).

[80] J. V. Coe, J. T. Snodgrass, C. B. Freidhoff, K. M. McHugh, and K. H. Bowen, The Journal of Chemical Physics **83**, 3169 (1985).

[81] T. A. Miller, B. R. Zegarski, T. J. Sears, and V. E. Bondybey, The Journal of Physical Chemistry **84**, 3154 (1980).

[82] M. A. Johnson, J. Rostas, and R. N. Zare, Chemical Physics Letters **92**, 225 (1982).

[83] M. A. Johnson, M. L. Alexander, and W. C. Lineberger, Chemical Physics Letters **112**, 285 (1984).

[84] W. C. Lineberger and M. A. Johnson, *Techniques for the Study of Ion Molecule Reactions*, volume 20, chapter 11, pages 591–631, Wiley, New York, 1982.

[85] G. Ganteför, H. Siekmann, and K. Meiwes-Broer, Chemical Physics Letters **165**, 293 (1990).

[86] D. L. Osborn, D. J. Leahy, D. R. Cyr, and D. M. Neumark, The Journal of Chemical Physics **104**, 5026 (1996).

[87] L. A. Posey, M. J. Deluca, and M. A. Johnson, Chemical Physics Letters **131**, 170 (1986).

[88] P. A. Tipler and R. A. Llewellyn, *Modern Physics*, Freeman, 3rd edition, 1999.

[89] C. R. Gebhardt, T. P. Rakitzis, P. C. Samartzis, V. Ladopoulos, and T. N. Kitsopoulos, Review of Scientific Instruments **72**, 3848 (2001).

[90] D. Townsend, M. P. Minitti, and A. G. Suits, Review of Scientific Instruments **74**, 2530 (2003).

[91] D. A. Chestakov et al., The Journal of Physical Chemistry A **108**, 8100 (2004).

[92] V. Dribinski, A. Ossadtchi, V. A. Mandelshtam, and H. Reisler, Review of Scientific Instruments **73**, 2634 (2002).

[93] S. Manzhos and H.-P. Loock, Computer Physics Communications **154**, 76 (2003).

[94] M. J. J. Vrakking, Review of Scientific Instruments **72**, 4084 (2001).

[95] K. M. Ervin, I. Anusiewicz, P. Skurski, J. Simons, and W. C. Lineberger, The Journal of Physical Chemistry A **107**, 8521 (2003).

[96] K. L. Reid, Annual Review of Physical Chemistry **54**, 397 (2003).

[97] R. N. Zare, Molecular Photochemistry **4**, 1 (1972).

[98] R. Mabbs, E. R. Grumbling, K. Pichugin, and A. Sanov, Chem. Soc. Rev. **38**, 2169 (2009).

[99] A. Sanov and R. Mabbs, International Reviews in Physical Chemistry **27**, 53 (2008).

[100] C. L. Adams, H. Schneider, K. M. Ervin, and J. M. Weber, The Journal of Chemical Physics **130**, 074307 (2009).

[101] G. Aravind, N. Bhargava Ram, A. K. Gupta, and E. Krishnakumar, Physical Review A **79**, 043411 (2009).

[102] M. Allan and I. I. Fabrikant, Journal of Physics B: Atomic, Molecular and Optical Physics **35**, 1025 (2002).

[103] C. Szmytkowski and A. M. Krzysztofowicz, Chemical Physics Letters **209**, 474 (1993).

[104] C. E. H. Dessent, C. G. Bailey, and M. A. Johnson, The Journal of Chemical Physics **105**, 10416 (1996).

[105] I. I. Fabrikant and H. Hotop, Physical Review A **63**, 022706 (2001).

[106] J. M. Weber, I. I. Fabrikant, E. Leber, R. M-W., and H. Hotop, The European Physical Journal D **11**, 247 (2000).

[107] W. P. Hu and D. G. Truhlar, The Journal of Physical Chemistry **98**, 1049 (1994).

[108] M. S. Bowen, M. Becucci, and R. E. Continetti, The Journal of Physical Chemistry A **109**, 11781 (2005).

[109] R. Mabbs, M. Van Duzor, F. Mbaiwa, and J. Wei, Journal of Physics: Conference Series **194**, 012051 (2009).

[110] F. Mbaiwa, M. Van Duzor, J. Wei, and R. Mabbs, The Journal of Physical Chemistry A **114**, 1539 (2010).

[111] F. Mbaiwa, J. Wei, M. Van Duzor, and R. Mabbs, The Journal of Chemical Physics **132**, 134304 (2010).

[112] E. W. Hansen and P.-L. Law, J. Opt. Soc. Am. A **2**, 510 (1985).

[113] C. Moore, Journal of the Optical Society of America **50**, 407 (1960).

[114] A. Mandl and H. A. Hyman, Physical Review Letters **31**, 417 (1973).

[115] E. J. Robinson and S. Geltman, Physical Review **153**, 4 (1967).

[116] C. C. Arnold, D. M. Neumark, D. M. Cyr, and M. A. Johnson, The Journal of Physical Chemistry **99**, 1633 (1995).

[117] A. D. Dickson, I. M. Mills, and J. Bryce Crawford, The Journal of Chemical Physics **27**, 445 (1957).

[118] H. Hotop and W. C. Lineberger, Journal of Physical and Chemical Reference Data **14**, 731 (1985).

[119] J. Cooper and R. N. Zare, The Journal of Chemical Physics **48**, 942 (1968).

[120] J. Cooper and R. N. Zare, The Journal of Chemical Physics **49**, 4252 (1968).

[121] M. Van Duzor, J. Wei, F. Mbaiwa, and R. Mabbs, The Journal of Chemical Physics **131**, 204306 (2009).

[122] R. Wester, A. E. Bragg, A. V. Davis, and D. M. Neumark, The Journal of Chemical Physics **119**, 10032 (2003).

[123] M. K. Gilles, K. M. Ervin, J. Ho, and W. C. Lineberger, The Journal of Physical Chemistry **96**, 1130 (1992).

[124] H.-Y. Chen and W.-S. Sheu, Journal of the American Chemical Society **122**, 7534 (2000).

[125] R. Mabbs, E. Surber, and A. Sanov, Chemical Physics Letters **381**, 479 (2003).

[126] J. Kim et al., Journal of the American Society for Mass Spectrometry **10**, 810 (1999).

[127] M. Kimura, O. Sueoka, C. Makochekanwa, H. Kawate, and M. Kawada, The Journal of Chemical Physics **115**, 7442 (2001).

[128] E. P. Wigner, Physical Review **73**, 1002 (1948).

[129] P. Gill, W. Murray, and M. Wright, *Practical Optimization*, Elsevier, 1981.

[130] N. Stone, Atomic Data and Nuclear Data Tables **90**, 75 (2005).

[131] P. Burke and C. Joachain, *Theory of Electron-Atom Collisions Part I: Potential Scattering*, Plenum, 1994.

[132] T. F. O'Malley, L. Spruch, and L. Rosenberg, Journal of Mathematical Physics **2**, 491 (1961).

[133] B. R. Levy and J. B. Keller, Journal of Mathematical Physics **4**, 54 (1963).

[134] M. Atoji, The Journal of Chemical Physics **25**, 174 (1956).

[135] M. Guerra, D. Jones, G. Distefano, F. Scagnolari, and A. Modelli, The Journal of Chemical Physics **94**, 484 (1991).

[136] A. Benitez, J. H. Moore, and J. A. Tossell, The Journal of Chemical Physics **88**, 6691 (1988).

[137] A. Herzenberg and B. C. Saha, Journal of Physics B: Atomic and Molecular Physics **16**, 591 (1983).

[138] W. Domcke, Journal of Physics B: Atomic and Molecular Physics **14**, 4889 (1981).

[139] W. Domcke and L. S. Cederbaum, Journal of Physics B: Atomic and Molecular Physics **14**, 149 (1981).

[140] H. Kato et al., Journal of Physics B: Atomic, Molecular and Optical Physics **43**, 065205 (2010).

[141] A. M. Krzysztofowicz and C. Szmytkowski, Journal of Physics B: Atomic, Molecular and Optical Physics **28**, 1593 (1995).

[142] P. D. Burrow, A. Modelli, N. S. Chiu, and K. D. Jordan, The Journal of Chemical Physics **77**, 2699 (1982).

[143] K. Aflatooni and P. D. Burrow, The Journal of Chemical Physics **113**, 1455 (2000).

[144] A. M. Krzysztofowicz and C. Szmytkowski, Chemical Physics Letters **219**, 86 (1994).

[145] A. Modelli, F. Scagnolari, G. Distefano, D. Jones, and M. Guerra, The Journal of Chemical Physics **96**, 2061 (1992).

[146] A. A. Christodoulides, R. Schumacher, and R. N. Schindler, The Journal of Physical Chemistry **79**, 1904 (1975).

[147] K. Aflatooni and P. Burrow, International Journal of Mass Spectrometry **205**, 149 (2001).

[148] W. E. Wentworth, R. George, and H. Keith, The Journal of Chemical Physics **51**, 1791 (1969).

[149] P. Datskos, L. Christophorou, and J. Carter, Chemical Physics Letters **168**, 324 (1990).

[150] P. G. Datskos, L. G. Christophorou, and J. G. Carter, The Journal of Chemical Physics **97**, 9031 (1992).

[151] S. Chu and P. Burrow, Chemical Physics Letters **172**, 17 (1990).

[152] D. M. Pearl, P. D. Burrow, I. I. Fabrikant, and G. A. Gallup, The Journal of Chemical Physics **102**, 2737 (1995).

[153] M. Braun, I. I. Fabrikant, M.-W. Ruf, and H. Hotop, Journal of Physics B: Atomic, Molecular and Optical Physics **40**, 659 (2007).

[154] E. Alge, N. G. Adams, and D. Smith, Journal of Physics B: Atomic and Molecular Physics **17**, 3827 (1984).

[155] D. Spence and G. J. Schulz, The Journal of Chemical Physics **58**, 1800 (1973).

[156] G. F. Hildebrandt, F. G. Kellert, F. B. Dunning, K. A. Smith, and R. F. Stebbings, The Journal of Chemical Physics **68**, 1349 (1978).

[157] C. W. Walter, B. G. Lindsay, K. A. Smith, and F. B. Dunning, Chemical Physics Letters **154**, 409 (1989).

[158] M.-W. Ruf, M. Braun, S. Marienfeld, I. I. Fabrikant, and H. Hotop, Journal of Physics: Conference Series **88**, 012013 (2007).

[159] D. Pearl and P. Burrow, Chemical Physics Letters **206**, 483 (1993).

[160] S. H. Alajajian, M. T. Bernius, and A. Chutjian, Journal of Physics B: Atomic, Molecular and Optical Physics **21**, 4021 (1988).

[161] H. Shimamori and Y. Nakatani, Chemical Physics Letters **150**, 109 (1988).

[162] H. Shimamori, Y. Tatsumi, Y. Ogawa, and T. Sunagawa, Chemical Physics Letters **194**, 223 (1992).

[163] X. Ling, K. A. Smith, and F. B. Dunning, Physical Review A **47**, R1 (1993).

[164] K. D. Jordan and P. D. Burrow, Chemical Reviews **87**, 557 (1987).

[165] X. Shi, V. K. Chan, G. A. Gallup, and P. D. Burrow, The Journal of Chemical Physics **104**, 1855 (1996).

[166] X. Shi, T. M. Stephen, and P. D. Burrow, The Journal of Chemical Physics **96**, 4037 (1992).

[167] G. A. Gallup, K. Aflatooni, and P. D. Burrow, The Journal of Chemical Physics **118**, 2562 (2003).

[168] K. Aflatooni, G. A. Gallup, and P. D. Burrow, The Journal of Physical Chemistry A **104**, 7359 (2000).

[169] G. A. Gallup, Journal of Physics B: Atomic, Molecular and Optical Physics **26**, 759 (1993).

[170] J. Bertran, I. Gallardo, M. Moreno, and J. M. Saveant, Journal of the American Chemical Society **114**, 9576 (1992).

[171] P. Mach, J. Urban, and V. Staemmler, Chemical Physics **356**, 164 (2009), Moving Frontiers in Quantum Chemistry: - Electron Correlation, Molecular Properties and Relativity.

[172] I. I. Fabrikant, Journal of Physics B: Atomic, Molecular and Optical Physics **24**, 2213 (1991).

[173] T. N. Rescigno, A. E. Orel, and C. W. McCurdy, Physical Review A **56**, 2855 (1997).

[174] M. F. Falcetta and K. D. Jordan, The Journal of Physical Chemistry **94**, 5666 (1990).

[175] I. I. Fabrikant and R. S. Wilde, Journal of Physics B: Atomic, Molecular and Optical Physics **32**, 235 (1999).

[176] M. V. Duzor et al., The Journal of Chemical Physics **134**, 184315 (2011).

[177] C. E. H. Dessent, C. G. Bailey, and M. A. Johnson, The Journal of Chemical Physics **103**, 2006 (1995).

[178] R. Mabbs, E. Surber, and A. Sanov, Analyst **128**, 765 (2003).

[179] Y. Shao et al., Physical Chemistry Chemical Physics **8**, 3172 (2006).

[180] J. Thom H. Dunning, The Journal of Chemical Physics **90**, 1007 (1989).

[181] D. E. Woon and J. Thom H. Dunning, The Journal of Chemical Physics **98**, 1358 (1993).

[182] K. A. Peterson, D. Figgen, E. Goll, H. Stoll, and M. Dolg, The Journal of Chemical Physics **119**, 11113 (2003).

[183] T.-S. Chang and D. M. Dennison, The Journal of Chemical Physics **21**, 1293 (1953).

[184] W. T. King, I. M. Mills, and J. Bryce Crawford, The Journal of Chemical Physics **27**, 455 (1957).

[185] T. E. Sharp and H. M. Rosenstock, The Journal of Chemical Physics **41**, 3453 (1964).

[186] J. Weber and G. Hohlneicher, Molecular Physics: An International Journal at the Interface Between Chemistry and Physics **101**, 2125 (2003).

[187] D. W. Kohn, E. S. J. Robles, C. F. Logan, and P. Chen, The Journal of Physical Chemistry **97**, 4936 (1993).

[188] N. Nibbering, S. Ingemann, and J. de Koning, *The Structure, Energetics, and Dynamics of Organic Ions*, chapter 7, Wiley, 1st edition, 1996.

[189] T. Andersen, H. K. Haugen, and H. Hotop, Journal of Physical and Chemical Reference Data **28**, 1511 (1999).

[190] T. F. O'Malley, Physical Review **150**, 14 (1966).

[191] T. F. O'Malley, Physical Review **137**, A1668 (1965).

[192] R. G. Shulman, B. P. Dailey, and C. H. Townes, Physical Review **78**, 145 (1950).

[193] D. Serxner, C. E. H. Dessent, and M. A. Johnson, The Journal of Chemical Physics **105**, 7231 (1996).

[194] C. E. H. Dessent, J. Kim, and M. A. Johnson, Accounts of Chemical Research **31**, 527 (1998).

[195] M. Van Duzor, J. Wei, F. Mbaiwa, and R. Mabbs, The Journal of Chemical Physics **133**, 144303 (2010).

[196] E. W. Jones and H. W. Thompson, Proceedings of the Royal Society of London. Series A. Mathematical and Physical Sciences **288**, 50 (1965).

[197] J. Thom. H. Dunning and P. J. Hay, Applied Physics Letters **28**, 649 (1976).

[198] A. C. Moskun, S. E. Bradforth, J. Thøgersen, and S. Keiding, The Journal of Physical Chemistry A **110**, 10947 (2006).

[199] A. Sanov, J. Faeder, R. Parson, and W. C. Lineberger, Chemical Physics Letters **313**, 812 (1999).

[200] Y. Zhao, C. C. Arnold, and D. M. Neumark, J. Chem. Soc., Faraday Trans. **89**, 1449 (1993).

[201] Y. Zhao, I. Yourshaw, G. Reiser, C. C. Arnold, and D. M. Neumark, The Journal of Chemical Physics **101**, 6538 (1994).

[202] M. J. Frisch et al., Gaussian 03, revision c.02, Gaussian, Inc., Wallingford, CT, 2004.

[203] P. J. Hay and J. Thom. H. Dunning, The Journal of Chemical Physics **66**, 1306 (1977).

[204] J. Thom H. Dunning and P. J. Hay, The Journal of Chemical Physics **69**, 134 (1978).

[205] P. J. Hay and J. Thom. H. Dunning, The Journal of Chemical Physics **69**, 2209 (1978).

[206] K. Radler and J. Berkowitz, The Journal of Chemical Physics **70**, 216 (1979).

[207] J. Simons, Journal of the American Chemical Society **103**, 3971 (1981).

[208] A. Sanov and W. Carl Lineberger, PhysChemComm **5**, 165 (2002).

[209] J. A. Stockdale, F. J. Davis, R. N. Compton, and C. E. Klots, The Journal of Chemical Physics **60**, 4279 (1974).

[210] K. A. Peterson, B. C. Shepler, D. Figgen, and H. Stoll, The Journal of Physical Chemistry A **110**, 13877 (2006).

[211] O. H. Crawford and W. R. Garrett, The Journal of Chemical Physics **66**, 4968 (1977).

[212] W. R. Garrett, The Journal of Chemical Physics **71**, 651 (1979).

[213] W. R. Garrett, The Journal of Chemical Physics **73**, 5721 (1980).

[214] W. R. Garrett, The Journal of Chemical Physics **69**, 2621 (1978).

[215] K. D. Jordan, Accounts of Chemical Research **12**, 36 (1979).

[216] T. Sommerfeld, Physical Chemistry Chemical Physics **4**, 2511 (2002).

[217] M. Stepanovic, Y. Pariat, and M. Allan, The Journal of Chemical Physics **110**, 11376 (1999).

[218] T. Sommerfeld, The Journal of Chemical Physics **126**, 124301 (2007).

[219] P. D. Burrow et al., The Journal of Chemical Physics **124**, 124310 (2006).

[220] A. M. Scheer, K. Aflatooni, G. A. Gallup, and P. D. Burrow, Physical Review Letters **92**, 068102 (2004).

[221] T. Sommerfeld, Journal of Physics: Conference Series **4**, 245 (2005).

[222] F. Lecomte, S. Carles, C. Desfrancois, and M. A. Johnson, The Journal of Chemical Physics **113**, 10973 (2000).

[223] T. Sommerfeld, The Journal of Physical Chemistry A **108**, 9150 (2004).

[224] A. Scheer et al., Chemical Physics Letters **411**, 46 (2005).

[225] Q. K. Timerghazin, T.-N. Nguyen, and G. H. Peslherbe, The Journal of Chemical Physics **116**, 6867 (2002).

[226] D. Dill, Physical Review A **7**, 1976 (1973).

[227] J. L. Dehmer and D. Dill, Physical Review Letters **35**, 213 (1975).

[228] S. T. Manson and A. F. Starace, Reviews of Modern Physics **54**, 389 (1982).

[229] S. B. Whitfield et al., Journal of Physics B: Atomic, Molecular and Optical Physics **39**, L335 (2006).

[230] R. C. Bilodeau, M. Scheer, and H. K. Haugen, Journal of Physics B: Atomic, Molecular and Optical Physics **31**, 3885 (1998).

[231] C. G. Bailey, C. E. H. Dessent, M. A. Johnson, and J. Kit H. Bowen, The Journal of Chemical Physics **104**, 6976 (1996).

[232] A. J. R. Heck and D. W. Chandler, Annual Review of Physical Chemistry **46**, 335 (1995).

[233] A. T. J. B. Eppink, S.-M. Wu, and B. Whitaker, *Imaging in Molecular Dynamics: Technology and Applications*, chapter 3, Cambridge, 1st edition, 2003.